



VCU

Virginia Commonwealth University
VCU Scholars Compass

Theses and Dissertations


Graduate School

2018

Evaluation and Adaptation of Live-Cell Interferometry for Applications in Basic, Translational, and Clinical Research

Kevin A. Leslie
Virginia Commonwealth University

Follow this and additional works at: <https://scholarscompass.vcu.edu/etd>

 Part of the Allergy and Immunology Commons, Biological and Chemical Physics Commons, Cancer Biology Commons, Cell Biology Commons, Hematology Commons, Integrative Biology Commons, Medical Biophysics Commons, Oncology Commons, and the Other Analytical, Diagnostic and Therapeutic Techniques and Equipment Commons

© The Author

Downloaded from

<https://scholarscompass.vcu.edu/etd/5562>

This Dissertation is brought to you for free and open access by the Graduate School at VCU Scholars Compass. It has been accepted for inclusion in Theses and Dissertations by an authorized administrator of VCU Scholars Compass. For more information, please contact libcompass@vcu.edu.

© Kevin Alexander Leslie 2018

All Rights Reserved

Evaluation and Adaptation of Live-Cell Interferometry for Applications in Basic, Translational, and
Clinical Research

A dissertation submitted in partial fulfillment of the requirements for the degree of Doctor of
Philosophy at Virginia Commonwealth University.

by

Kevin Alexander Leslie

M.S. College of William & Mary, 2012

B.S. College of William & Mary, 2009

Director: Dr. Jason C. Reed

Associate Professor, Department of Physics

Virginia Commonwealth University

Richmond, Virginia

August 2018

Acknowledgement

No one succeeds alone.

The end of this journey finds me indebted to a great number of people for opportunities, advice, inspiration, support, friendship, and love.

Words are insufficient compensation for gifts like these. The following thanks are a small start.

To Dr. Verrelli and Dr. Tombes, for building a program in which I could take part. Under your stewardship, the Integrative Life Sciences program has provided me both the financial means and the educational flexibility to conduct research that does not fit in the box of a single discipline. You have been tireless champions of every ILS student, and I am grateful for your support and confidence throughout my time at VCU.

To my committee, for your support, time, and collaboration. To Dr. Manjili, my thanks for your time as a professor and as an advisor on grant and research strategies. To Dr. Reiner, my thanks for your willingness to collaborate, our discussions on optics, and the extra -80 freezer space. To Dr. Ryan, my gratitude for many years of mast cell discussions, strategic guidance, scientific integrity, and parenting advice. To Dr. Toor, a more enthusiastic physician-researcher, there is none. My thanks for always having an open door and time for scientific discussions and teaching, despite a perpetually prohibitive schedule.

To Brian Barnstein, for providing an endless supply of mast cells, usually on short notice.

To Dr. Catherine Roberts, for making our T cell work possible and for always asking about Henry.

To Evelyn, for making sure everyone got what they needed when they needed it.

To the Reed lab, for your comradery, collaboration, and comic relief.

To Sean, for 14 years of friendship and scientific commiseration.

To Mark, for giving me a chance, an education, and a friendship. I am forever grateful.

To Dr. Reed, for your time and energy as a mentor and principal investigator. You have made it possible for me to take part in incredible research endeavors. My gratitude for your unwavering support of my personal goals is something I cannot adequately convey. Thank you for countless hours of teaching and advice, your flexibility, and the provision of key scientific and professional opportunities.

To The Andersons, for providing emotional support, child care, great food, great company, and a willingness to tolerate a contrarian who talks too much about science.

To Caroline, Katie, and Paige, for keeping me humble, making me laugh, and being incredible sisters and women. The world is lucky to have you.

To my parents, for your unending love, support, and the sacrifice of time and resources to make sure my world is full of kindness and open doors. You will always have my love and gratitude.

To my son, for reminding me of what is important in life. Years from now, when you stumble upon this work and decide to read it, know that you are a perpetual source of pride and joy.

To my wife, for happiness. None of this would have been possible without you. Through my successes and failures, you have celebrated and suffered with me. You have kept our family afloat. I could not ask for a better partner in life. I love you!

Table of Contents

| | |
|--|-----------|
| List of Figures..... | vii |
| List of Tables..... | ix |
| List of Abbreviations..... | x |
| Abstract..... | xii |
| Chapter 1 – Cell Mass: A Versatile Biomarker..... | 1 |
| 1.0 – Chapter Overview..... | 2 |
| 1.1 – Introduction..... | 2 |
| 1.2 – Rationale..... | 3 |
| 1.3 – Techniques for Measuring Cell Mass..... | 4 |
| 1.3.1 – Non-Optical Modalities..... | 4 |
| 1.3.2 – Optical Modalities..... | 6 |
| 1.4 – Live-Cell Interferometry..... | 8 |
| Chapter 2 – Technical Overview of Live-Cell Interferometry Systems..... | 10 |
| 2.0 – Chapter Overview..... | 11 |
| 2.1 – Original State of the VCU LCI System..... | 11 |
| 2.2 – Current State of the VCU LCI System..... | 14 |
| 2.3 – Image Analysis..... | 16 |
| 2.4 – HSLCI Platform Performance Metrics..... | 19 |
| Chapter 3 – Quantifying Melanoma Drug Resistance and Heterogeneity..... | 22 |
| 3.0 – Chapter Overview..... | 23 |
| 3.1 – Introduction..... | 23 |
| 3.2 – Methods..... | 29 |
| 3.3 – Results..... | 30 |
| 3.4 – Discussion..... | 41 |
| Chapter 4 – CD3+ T Cell Mass Dynamics During Stem Cell Transplantation..... | 44 |

| | |
|---|-----------|
| 4.0 – Chapter Overview..... | 45 |
| 4.1 – Introduction..... | 45 |
| 4.2 – Methods..... | 47 |
| 4.3 – Results..... | 50 |
| 4.4 – Discussion..... | 54 |
| Chapter 5 – Applications in Basic Research..... | 57 |
| 5.0 – Chapter Overview..... | 58 |
| 5.1 – Apoptosis Assays..... | 58 |
| 5.1.1 – Introduction..... | 58 |
| 5.1.2 – Results & Discussion..... | 59 |
| 5.1.3 – Methods..... | 60 |
| 5.2 – Mast Cell Biology..... | 62 |
| 5.2.1 – Introduction..... | 62 |
| 5.2.2 – Approach..... | 64 |
| 5.2.3 – Results..... | 64 |
| 5.2.4 – Discussion..... | 70 |
| 5.2.5 – Methods..... | 72 |
| 5.3 – Kinetics of KSHV Lytic Activation..... | 79 |
| Chapter 6 – Conclusions and Future Directions..... | 82 |
| 6.0 – Chapter Overview..... | 83 |
| 6.1 – Summary of Work Presented..... | 83 |
| 6.3 – Ongoing Work..... | 84 |
| 6.3.1 – Drug-Induced Cellular Senescence..... | 84 |
| 6.3.2 – Effects of Radiation on Endothelial Cells..... | 85 |
| 6.3.3 – PDX Models with HSLCI to Study Drug Resistance..... | 86 |
| 6.4 – Future Directions..... | 92 |
| 6.4.1 – Three-Dimensional Cell Culture..... | 92 |
| 6.4.2 – Large-Scale Patient Studies..... | 94 |

| | |
|-------------------------------|-----|
| 6.5 – Conclusion..... | 95 |
| List of References..... | 96 |
| Appendix..... | 110 |
| Supplementary Figures..... | 111 |
| Supplementary Tables..... | 114 |
| Supplementary Methods..... | 115 |
| Supplementary References..... | 117 |
| Vita..... | 119 |

List of Figures

- 1 – Overview of original LCI system hardware
- 2 – Overview of original LCI system optics
- 3 – Overview of HSLCI system hardware
- 4 – Schematic of HSLCI optical hardware and accompanying ray diagrams
- 5 – Example of HSLCI image processing pipeline steps
- 6 – HSLCI performance overview
- 7 – Overview of cell viability assays used for drug sensitivity screening
- 8 – Schematic of HSLCI multi-well biomass accumulation assay
- 9 – Biomass accumulation response to Vemurafenib treatment
- 10 – Comparing relative mass between Vemurafenib-sensitive and -resistant isogenic lines
- 11 – Vemurafenib (5 μ M) sensitivity as determined by plotting pre- and post-treatment growth rates for Vemurafenib-sensitive (M249P) and Vemurafenib-resistant (M249R4) cell lines
- 12 – Detecting resistant cells in a mixed population
- 13 – Effects of kinase inhibitors on Vemurafenib-resistant melanoma as measured by HSLCI
- 14 – Summary of effect of five kinase inhibitors on Vemurafenib-resistant melanoma as measured by HSLCI
- 15 – Sample preparation and analysis procedure
- 16 – Biomass of patient-derived CD3+ T cells post-transplant
- 17 – Biomass and GVHD grade of patient-derived CD3+ T cells 60 and 100 days, post-transplant
- 18 - Boxplots showing normalized T cell population mass distributions, over time, for two representative allogeneic transplant recipients
- 19 – Correlation of apoptosis, PI fluorescence, and mass loss in three cancer cell Lines
- 20 – Distribution of cell masses from a single mast cell population
- 21 – Distinct mast cell sub-populations

- 22 – HSLCI-measured DNP-HSA response kinetics and inter-population mass variation
- 23 – Active group mass and area versus time
- 24 – Correlation of Ionomycin dosing with mass loss and YoPro1 and PI Fluorescence in a single mast cell
- 25 – RBL-2H3 cell degranulation and recovery
- 26 – Proposed model of mast cell degranulation
- 27 – Summary of triggering agent mechanisms of action
- 28 – LCI sample mount and dosing overview
- 29 – Single-cell Doxycycline-induced KSHV lytic activation
- 30 – Overview of PDX model generation and usage
- 31 – Patient-derived xenograft (PDX) lines PT52 and HCl09 sensitivity to Carboplatin
- 32 – Single-cell example of PT52 Carboplatin response heterogeneity

List of Tables

1 – Patient Demographics

List of Abbreviations

| | |
|-------------------------|---------------------------------------|
| 2D..... | two dimensional |
| 3D..... | three dimensional |
| aGVHD..... | acute graft versus host disease |
| ASCO..... | American Society of Clinical Oncology |
| ATP..... | adenosine triphosphate |
| AUC..... | area under the curve |
| BMMC..... | bone marrow mononuclear cell |
| BRAF _i | BRAF inhibitor |
| CCD..... | charge-coupled device |
| CD3..... | cluster of differentiation 3 |
| CD8..... | cluster of differentiation 8 |
| cGVHD..... | chronic graft versus host disease |
| C _{max} | peak measured serum concentration |
| CMV..... | cytomegalovirus |
| CO ₂ | carbon dioxide |
| CV..... | coefficient of variation |
| ddCD3..... | donor-derived CD3 |
| DHM..... | digital holographic microscopy |
| DMEM..... | Dulbecco's Modified Eagle Medium |
| DMSO..... | dimethyl sulfoxide |
| DNA..... | deoxyribonucleic acid |
| DNP-HSA..... | Human Serum Albumin |
| EBV..... | Epstein Barr virus |
| ELISA..... | enzyme-linked immunosorbent assay |

ER.....estrogen receptor

FDA.....Food and Drug Administration

fps.....frames per second

GFP.....green fluorescent protein

GPUgraphics processing unit

GVHD.....graft versus host disease

GWAS.....genome-wide association study

Gy.....Gray

HER2.....human epidermal growth factor receptor 2

HHV-8.....human herpesvirus 8

HLA.....human leukocyte antigen

HSLCI.....high-speed live-cell interferometry

IgE.....immunoglobulin E

IL-3.....interleukin 3

IL-6.....interleukin 6

KS.....Kaposi's sarcoma

KSHV.....Kaposi's sarcoma-associated herpesvirus

LCI.....live-cell interferometry

LED.....light-emitting diode

MMF.....mycophenolate mofetil

MRD.....matched related donor

MTT.....3-(4, 5-dimethylthiazolyl-2)-2, 5-diphenyltetrazolium bromide

MTX.....methotrexate

MUD.....matched unrelated donor

NA.....numerical aperture

NOD.....non-obese diabetic

NRM.....non-relapse mortality

| | |
|------------|--|
| OPD..... | optical path difference |
| PCS..... | pluri potent stem cells |
| PDX..... | patient-derived xenograft |
| PI..... | propidium iodide |
| PR..... | progesterone receptor |
| PRS..... | pedestal resonant sensor |
| PSI..... | phase-shifting interferometry |
| QPI..... | quantitative phase imaging |
| QWLSI..... | quadriwave lateral shearing interferometry |
| RFP..... | red fluorescent protein |
| RNA..... | ribonucleic acid |
| ROC..... | Receiver Operator Characteristic |
| RPMI..... | Roswell Park Memorial Institute |
| SCF..... | stem cell factor |
| SCID..... | severe combined immunodeficiency |
| SCT..... | stem cell transplant |
| SD..... | standard deviation |
| SLIM..... | spatial light interference microscopy |
| SMR..... | suspended microchannel resonator |
| SNP..... | single-nucleotide polymorphism |
| SSD..... | solid-state drive |
| TNBC..... | triple-negative breast cancer |
| UCLA..... | University of California - Los Angeles |
| VCU..... | Virginia Commonwealth University |
| YP1..... | YoPro1 |

Abstract

EVALUATION AND ADAPTATION OF LIVE-CELL INTERFEROMETRY FOR APPLICATIONS IN BASIC, TRANSLATIONAL, AND CLINICAL RESEARCH

By Kevin Alexander Leslie, M.S.

A dissertation submitted in partial fulfillment of the requirements for the degree of Doctor of Philosophy at Virginia Commonwealth University

Virginia Commonwealth University, 2018

Major Director: Dr. Jason Reed, Associate Professor, Department of Physics

Cell mass is an important indicator of cell health and status. A diverse set of techniques have been developed to precisely measure the masses of single cells, with varying degrees of technical complexity and throughput. Here, the development of a non-invasive, label-free optical technique, termed Live-Cell Interferometry (LCI), is described. Several applications are presented, including an evaluation of LCI's utility for assessing drug response heterogeneity in patient-derived melanoma lines and the measurement of CD3+ T cell kinetics during hematopoietic stem cell transplantation. The characterization of mast cells during degranulation, the measurement of viral reactivation kinetics in Kaposi's Sarcoma, and drug response studies in patient-derived xenograft models of triple-negative breast cancer are also discussed. Taken together, data from these studies highlight LCI's versatility as a tool for clinical, translational, and basic research applications.

Chapter 1

Cell Mass: A Versatile Biomarker

1.0 Chapter Overview

This chapter provides a brief overview of cell mass, including its relevance as an indicator of cell health, and techniques with which it can be measured. Cell mass is the common thread woven through all of the experiments described in this dissertation, and the sections that follow aim to orient the reader to this important intersection of single-cell biology and physics.

1.1 Introduction

Cell growth and proliferation are tightly regulated but incompletely understood processes.^{1,2} In unicellular organisms like bacteria, they are generally governed by resource availability in the extracellular environment.³ For multicellular organisms, comprised of varying tissue types and proceeding through multiple stages of development, a more complex and coordinated system of signaling is required to maintain homeostasis.^{4,5} This system, enabling individual cells to monitor and change or maintain their size, relies on a combination of molecular gradients within the cells themselves, mechanical signals from the extracellular environment, and paracrine and endocrine signaling.^{6,7,8,9} Further, as cells can grow (accumulate mass) without dividing, it is important to appreciate that these two processes, cell growth and cell division, can be differentially regulated.¹

A human's survival and reproduction depends on the continuous and appropriate regulation of cell growth and proliferation. Injuries to the skin must be rapidly repaired, immune cell populations must expand in response to infection, egg cells must remain viable for decades, and muscles must adapt to mechanical demands. Even cells that appear quiescent can be quite dynamic, striking a delicate metabolic balancing act by exhibiting levels of biosynthesis identical

to growing or proliferating cells while simultaneously having higher levels of protein degradation.¹⁰ However, when this system of regulated cell growth and division breaks down, disease often results. Hearts can become enlarged, cancer can develop, and developmental brain disorders can occur.¹¹⁻¹³

The work described herein focuses on measuring the mass of a variety of human cells to understand how their growth and division are impacted by different stimuli, including cytotoxic drugs. In turn, this information could allow us to better understand basic biological processes, predict drug efficacy, and even modulate therapeutic regimens for cancer patients.

1.2 Rationale

A red blood cell weighs just 27 picograms, on average, while an ovum can be 100,000 times heavier, exceeding 3.5 micrograms.¹⁴ Neutrophils, important components of the immune system, are renewed on an almost daily basis, while neurons of the cerebral cortex can last a lifetime.^{15,16} This kind of dynamic range implies a corresponding heterogeneity in rates of mass accumulation and division among human cell types.¹⁷ Logically, as common processes like apoptosis (controlled cell death), growth, and division all encompass changes in cell size or protein synthesis, cells should exhibit mass kinetic signatures that correspond with these events.¹⁸ This should also hold true for cell type-specific functions like activation in T cells or degranulation in mast cells.¹⁹⁻²³ Taken further, significant dysregulation or disruption of any of these processes should be detectable as a change in these kinetic signatures. However, accurately characterizing baseline cell growth and, subsequently, detecting these kinetic signatures requires the ability to non-invasively measure cell mass with picogram sensitivity.

Within the last 15 years, significant progress has been made on this front, seeing the advent of multiple measurement platforms capable of achieving single-cell resolution. These techniques and their subsequent applications are discussed in the sections that follow.

1.3 Techniques for Measuring Cell Mass

Cellular biomass can be measured using a variety of techniques, including biochemical stains, mass spectrometry, electron microscopy, various forms of interference microscopy, and microbalances.²⁴⁻⁵⁰ However, most have seen limited use in clinical or research settings due to their technical complexity, inadequate throughput, or limited precision.⁵¹⁻⁵³ For the purposes of this discussion, only techniques capable of measuring mass in living cells over time with picogram precision will be considered; they will be categorized as either optical or non-optical modalities.

1.3.1 Non-optical modalities

Non-optical modalities rely on indirect physical measurements to determine the mass of a cell. The two most common are Suspended Microchannel Resonators (SMRs) and Pedestal Resonant Sensors (PRSs). While these techniques can often be more precise than optical approaches, their low throughput and inability to handle a variety of cell types (i.e. adherent and non-adherent, clumps and single cells) tend to be limiting factors to their broad-scale adoption.

Suspended Microchannel Resonators

Suspended microchannel resonators derive the mass of a cell by measuring changes in the vibrational frequencies of a silicon cantilever.⁵⁴ Briefly, the cantilever contains a small channel

through which liquid and particles or cells can flow. This cantilever is vibrated at multiple frequencies and, using small piezoresistors embedded in the silicon surface or an external laser doppler vibrometer, these vibrations are recorded.⁵⁵ As a cell passes through the microchannel, a detectable alteration of vibrational patterns is induced. These patterns can be used to derive the buoyant mass of a cell. SMRs have been used successfully to measure a range of bacteria, yeast, and mammalian cell types.⁵⁶

The newest iteration of this technique involves arraying multiple SMRs in a serial fashion, allowing the measurement of the same cell multiple times over the course of 15 minutes with a precision of 50 femtograms; cells remain viable after passing through the channel. This setup has been used to correlate drug-induced changes in single-cell growth rates in myeloma cells to drug responses in several patients.⁵⁷ However, SMRs are currently limited to analyzing 60-120 cells per hour.⁵⁸ In order to detect rare cells in a heterogeneous population or conduct screens on multiple therapeutics simultaneously, a significant increase in throughput is required.

Pedestal Resonant Sensors (PRS)

Pedestal resonant sensors (PRS) operate similarly to SMRs. Briefly, the devices consist of an array of small sensors ($60 \times 60 \mu\text{m}^2$) each suspended by a set of four nanoscale springs ($80 \mu\text{m} \times 4 \mu\text{m}$).^{59,60} Single cells are deposited on, and subsequently attach to, these sensors. A laser doppler vibrometer measures the resonant frequencies of these sensors, over time, in the presence of the living cells. As cells change their mass, they detectably alter the resonant frequency of the sensor to which they are attached. From these resonant frequency changes, cell mass can be derived. Despite an ability to accurately measure cell mass over many hours, PRSs are not

compatible with fluorescence microscopy, preventing correlative studies.⁵⁶ Like SMRs, PRSs suffer from low throughput (<100 cells measured simultaneously). In addition, adherent cells often migrate off the sensor pedestals, complicating the process of tracking single cells for multiple days.⁶¹

1.3.2 Optical modalities

Quantitative optical mass measurements of single living cells began in the 1950s^{48,62} and, thanks to advances in both digital imaging technology and computing power, newer approaches have increased in speed, precision, and practicality.^{26,27}

In their most basic form, optical mass measurements of cells can be acquired using Michelson-style interferometry, which involves the extraction of information from the superimposition of two light beams that have traveled separate paths after being split from a single illumination source. The first beam passes through a target object (i.e. a cell), while the second (“reference”) beam passes through a material that simulates the optical path of the first, without the target object. Re-combination of these two beams yields an interference pattern from which the mass of the target can be derived. Specifically, the interference pattern is a result of the differing lengths of the optical paths (a product of the medium’s index of refraction and the geometric length of the light’s path) between the two beams. The dense material in the target cell, through which the first beam passes, increases the optical path length of the beam. When these path length differences are calculated across the entire area of a target object, the optical density of the object can be calculated. Optical density can be converted into dry mass by applying a whole-cell-average dry mass ratio based on the average refractive indices of biological molecules

(e.g., protein, DNA, RNA).⁴⁶ Our group's original live-cell interferometry platform utilized phase-shifting interferometry (PSI) which operates using the basic principles outlined above. However, PSI also uses a piezoelectric transducer to rapidly introduce path length changes in one arm of the Michelson-style setup during image collection, resulting in the generation of multiple interferograms that enable the enhanced resolution of optical path differences.⁶³

Variations on this technique have yielded an array of quantitative phase imaging (QPI) microscopy platforms for the examination of biological specimens.^{56,64} A notable example is digital holographic microscopy (DHM), wherein a laser light source is used to generate holograms of living cells, enabling the reconstruction of three-dimensional images.⁶⁵ The technique, like all QPI-based modalities, requires no cell staining or labeling. It is also, uniquely, afocal, as images can be digitally autofocused (within a range limited by the numerical aperture of the microscope objective) after collection depending on the z-dimension layer of interest. However, current implementations suffer from high noise as a result of multiple reflections and laser speckling inherent to DHM.⁶⁶ In addition, though DHM's use of laser illumination poses problems for long-term imaging of biological samples due to risks of phototoxicity, this can generally be mitigated by using lower intensities or longer wavelengths.⁶⁷

A low-noise alternative to DHM is quadriwave lateral shearing interferometry (QWLSI).²⁶ In this QPI variant, non-laser coherent light passes through living cells and is then sheared by a diffraction grating into multiple replica wavefronts. These wavefronts combine to produce an interference pattern that yields dry mass data on the target cells. Typically, this process is condensed into a single camera unit, wherein the diffraction grating is fixed several millimeters from the camera's CCD sensor (on which the interference pattern is produced and recorded).

This modular camera approach enables the technique to be easily incorporated into existing microscopy platforms and used in parallel with fluorescence techniques.

Recent applications of quantitative phase microscopy using other imaging platforms include measurements of cell growth, cell death, membrane mechanics, individual organelles, and preliminary imaging studies of mouse pluripotent stem cells (PSCs).^{60,68-71} Emerging translational uses of the technique are highly promising, including its use in characterizing tissue inflammation, wound healing, and circulating tumor cells.⁷²⁻⁷⁴

1.4 Live-Cell Interferometry (LCI)

Prior to the initiation of the work described herein, Reed et al. utilized early versions of an optical single-cell mass measurement technique, termed live-cell interferometry (LCI), to investigate a broad range of biological processes. Based on a Michelson-style phase-shifting interferometer, early LCI platforms were precise but low-throughput, capable of measuring single cells with picogram sensitivity and CV's less than 1%, but slowed down by required focusing and image collection times.

Initially, LCI was used to address questions in basic biology, such as the quantification of cytoskeletal rearrangements in NIH/3T3 embryonic fibroblasts in response to mechanical stimulation.⁷⁵ Later studies focused on the appropriation of mass between daughter cells during cell division, as well as the motility and distribution of mass in undifferentiated versus differentiated human stem cell colonies.^{76,77}

Applications eventually expanded to include the characterization of drug responses in a variety of human cancer lines. Experiments using H929 multiple myeloma cells demonstrated the LCI's

ability to determine sensitivity to Tunicamycin in several hundred individual cells by measuring cell mass over time.⁷⁸ This was followed by a similar set of experiments using Trastuzumab and four breast cancer cell lines of varying HER2 statuses and clustering behaviors.²⁵ Taken together, these studies highlighted LCI's ability to measure drug sensitivity in both adherent and non-adherent cell types, as well as single cells and/or cell clusters. This versatility remains one of LCI's fundamental advantages. However, at the time, the LCI's throughput was a major limiting factor in expanding to new translational research projects and improving its utility for existing applications.

Chapter 2

Technical Overview of Live-Cell Interferometry Systems

2.0 Chapter Overview

This chapter provides hardware and performance descriptions of the original LCI system and its high-speed successor, the HSLCI (High-Speed Live-Cell Interferometry) system. The sections that follow provide technical context for the diverse range of applications described in later chapters.

2.1 Original State of the VCU LCI System

In 2012, the original VCU LCI system utilized phase-shifting interferometry⁶³ and consisted of a combination of two motorized linear translation stages, one small stepper motor, one flexure stage, a CCD camera, a single LED illumination source, and a custom Michelson interferometric imaging head. It was situated on a vibration isolation table and was not enclosed. A schematic and image of the system are shown in **Figure 1**.

The core of this system was the interferometer head (**Figure 2**). Briefly, 660 nm collimated light from a fiber-coupled LED source (Thorlabs, Inc.) enters the rightmost side of the head unit. This light is split by a beam splitter into two beams: a reference beam and a sample beam. The sample beam is directed towards the sample (containing beads or cells). The reference beam is directed through a reference cell designed to mimic the optical path of the sample beam, minus the actual sample. This reference cell is composed of two pieces of glass mounted in a small aluminum block, separated by 700 μm steel spheres, and filled with distilled deionized water. After passing through the reference cell, the reference beam encounters a mirror (whose position is adjustable) and reflected back towards the original beam splitter. Both the reference and sample beams are reflected (and subsequently recombined) towards the CCD camera after re-encountering the beam splitter. The retardation of the sample beam relative to the reference

beam, caused by the higher index of refraction of the material encountered in the sample objects, results in the generation of interference patterns in the light reaching the CCD camera. In order for this technique to work, the interferometric head's mirror must be positioned with micrometer precision so that the lengths of the geometric paths traveled by both the sample and reference beams are identical. Additionally, the sample's tilt must be corrected so that the objects being imaged are parallel to the imaging lens. Reference mirror positioning was accomplished manually using an external rotary knob mounted to the side of the interferometer

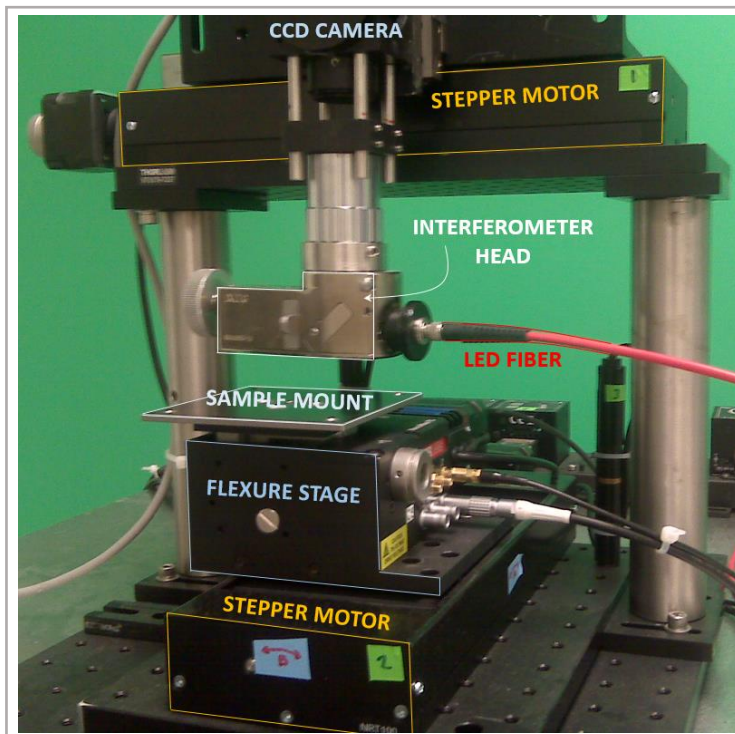


Figure 1. Overview of original LCI system hardware. Optical components are arranged to form a Michelson interferometer (the fixed interferometer head contains the reference arm and beam splitter). Stepper motors and a flexure stage are controlled using a custom MATLAB interface and enable sample navigation, focusing, and tilt correction. Coherent light is provided by an LED. A black and white CCD camera collects images. The entire system rests on a vibration isolation table to minimize noise.

head. Tilt correction was automatically performed using a stepper motor controlled by a custom MATLAB script; a three-axis flexure stage (NanoMax-TS, Part# MAX301, Thorlabs, Inc.) enabled rapid Z-direction adjustments for phase shifting. Sample navigation was performed using two linear stepper motors (NRT100, Thorlabs, Inc.). Images were collected using a CCD camera coupled to a Mitutoyo VMU and 40X objective lens.

Samples were deposited onto 20 mm x 20 mm hand cut pieces of silicon wafer, submerged in culture media, in one of four wells in a custom Teflon block. Custom “optical windows,”

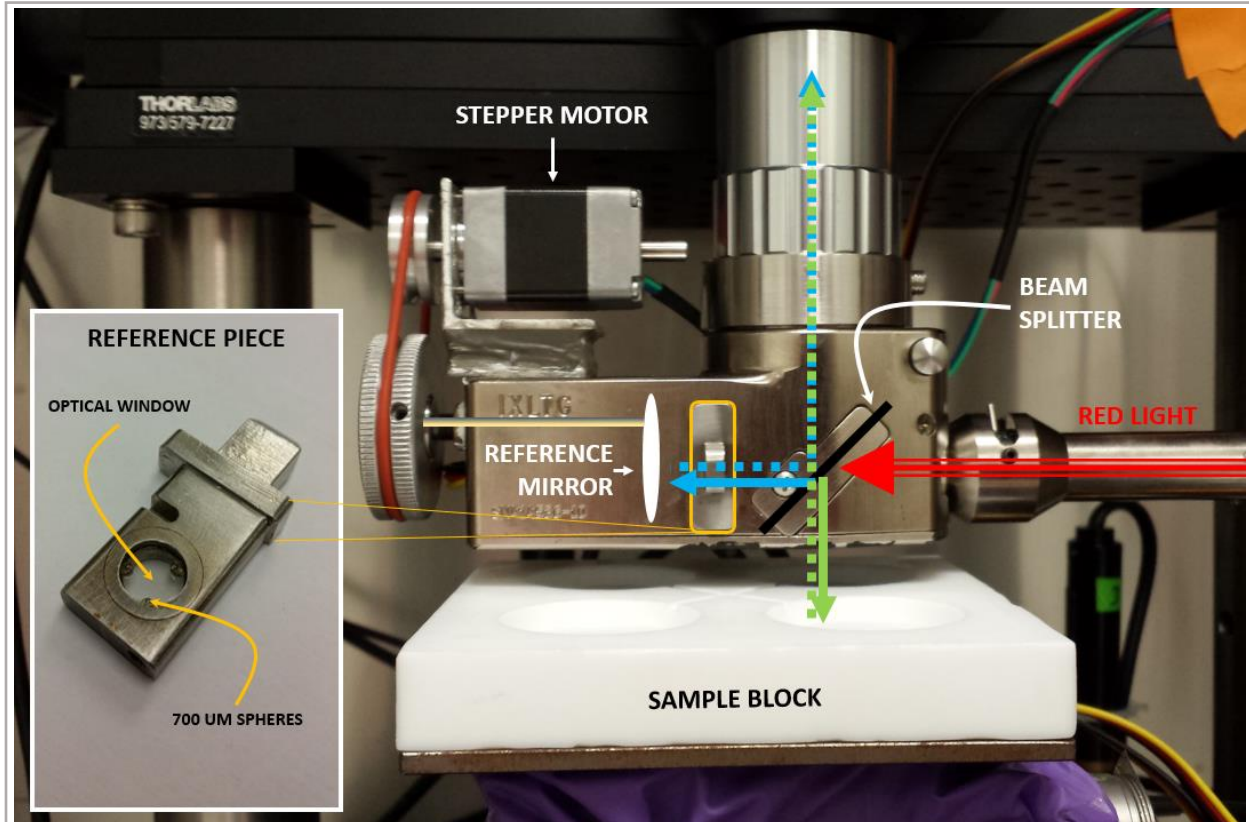


Figure 2. Overview of original LCI system optics. Collimated light from a fiber-coupled LED source enters the rightmost side of the head unit. This light is split by a beam splitter into two beams: a reference beam (blue) and a sample beam (green). The sample beam is directed towards the sample (containing beads or cells). The reference beam is directed through a reference cell designed to mimic the optical path of the sample beam, minus the actual sample. After passing through the reference cell, the reference beam encounters a mirror (whose position is adjustable) and reflected back towards the original beam splitter. Both the reference and sample beams are reflected (and subsequently recombined) towards the CCD camera after re-encountering the beam splitter.

consisting of 28.6 mm stainless steel rings coupled to optical glass and supported by three 700 μm stainless steel spheres, were then placed on top of the silicon wafers.

All sample navigation and image collection was performed and triggered using manual micrometer manipulation combined with stepper motor movement and image acquisition controlled through a simple MATLAB graphical user interface (GUI). Capturing a single 2 x 2 grid of images required approximately 90 seconds.

After collection, images were processed using a combination of custom MATLAB scripts, described previously by Reed et al. to unwrap the acquired phase images and calculate phase shifts.⁷⁸ Computed phase images were “flattened” by correcting for low-frequency background. Single cells were segmented from the background of the flattened phase images using a spatial-derivative edge detection kernel; their locations and optical volumes were recorded. Frame-to-frame cell tracking was accomplished with a previously-described particle tracking algorithm.⁷⁸ Single-cell growth tracks were generated for each object tracked and then plotted as optical volume versus time. Performance of the system in this state was slow but robust, with data revealing coefficients of variation (CV) less than 0.5% and picogram sensitivity.

2.2 Current state of the VCU LCI System

The current high-speed live-cell interferometry (HSLCI) platform consists of a custom-built inverted optical microscope coupled to a quadriwave lateral shearing interferometric camera (SID4BIO, Phasics, Inc.).^{26,79,80} The camera consists of a 1600 x 1200 pixel CCD camera (B1621, Imprex, Inc.) fitted with a modified Shack-Hartman mask. It is self-referencing, simple to mount, and capable of recording at 30 fps. The SID4BIO’s flexibility and image acquisition efficiency ultimately precipitated its replacement of the LCI’s original interferometer head. Cells are imaged in single, standard-footprint (128 mm x 85 mm), glass-bottomed, multi-well plates.

Acquired images are analyzed in near real-time by a downstream PC (Dell Precision Tower 5810). All of the platform's hardware and software components are available commercially. A basic schematic of the HSLCI system is provided in **Figure 3**.

Briefly, a multi-well plate holder coupled to three linear translation stages enables automated sample movement in three dimensions during image acquisition. The scale of topographical variation within and between multi-well plates necessitates a flexible and robust focusing scheme (**Supplementary Figure 1**). Best focus is rapidly and consistently maintained during lateral scanning using a custom-built automatic feedback loop consisting of a coaxial optical beam deflection position sensor coupled to a one-dimensional piezo stack on which the microscope objective is mounted. The sample is illuminated using a 660 nm LED light source that is collimated and then strobed to coincide with the SID4BIO camera's exposure, using a SID4BIO-generated trigger, at a rate of 4 fps. After passing through the sample, the light is magnified by an objective lens and directed to both the SID4BIO and a wide-field CCD camera (acA645-100, Basler AG) utilized for correlative and fluorescent imaging (**Figure 4**). Either a 40X objective (Nikon Plan Fluorite, NA 0.75), 20x objective (Nikon Neofluar, NA 0.5 or Nikon Plan Fluorite, NA 0.3) or a 10x objective (Nikon Plan Fluorite, NA 0.3) were used for the growth kinetics and population studies described herein, depending on the desired size of the field of view. The entire HSLCI platform is installed inside a standard cell culture incubator (Steri-Cult CO₂ Incubator, ThermoFisher) to maintain the environmental conditions necessary for cell viability.

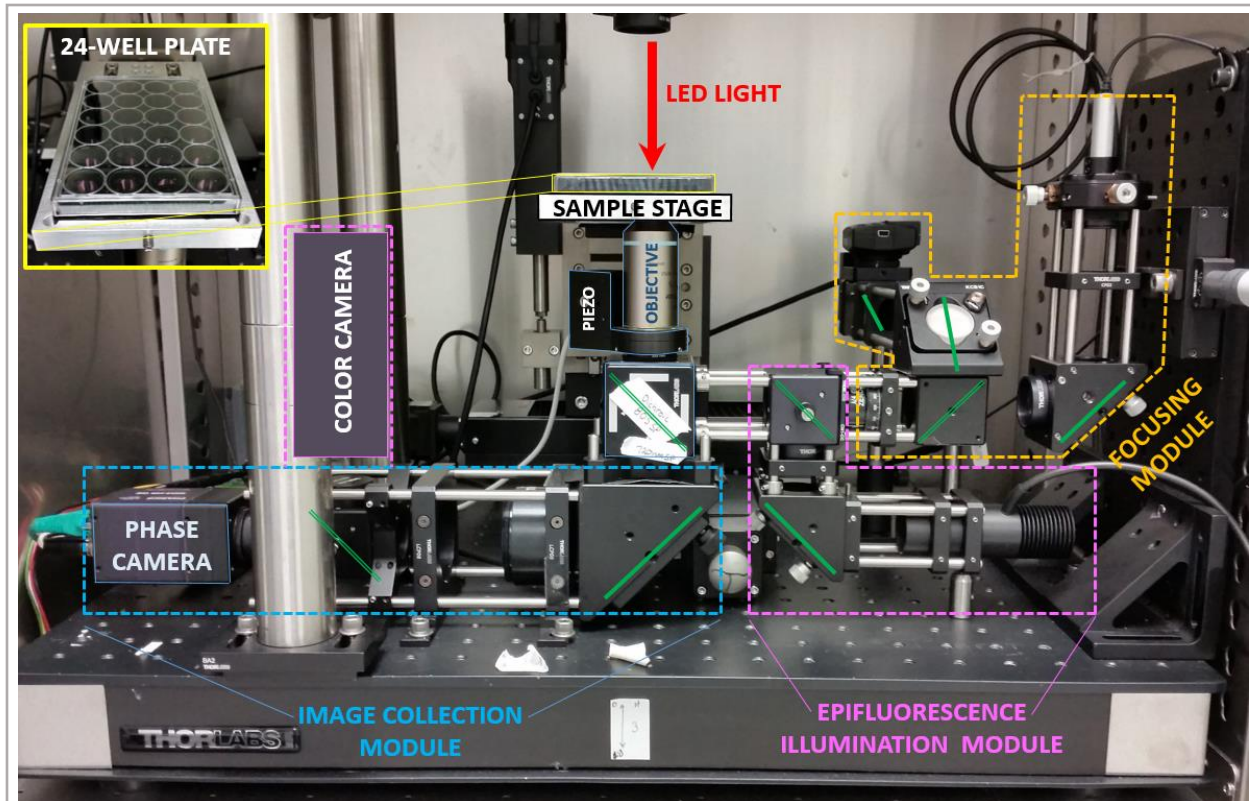


Figure 3. Overview of HSLCI system hardware. A 24-well plate containing samples for imaging is secured in a custom stage. The sample is illuminated from above using collimated light from an LED. Three stepper motors enable stage movement in X, Y, and Z directions for sample navigation. The focusing module uses a feedback loop to maintain a fixed distance between the objective and the plate bottom during imaging. The epifluorescence module provides illumination for the excitation of fluorophores. The image collection module is comprised of the Phasics QWLSI camera for the collection of interferograms and a color CCD camera for the collection of brightfield and fluorescent images. Mirrors are represented by solid green lines and dichroics are represented by double green lines.

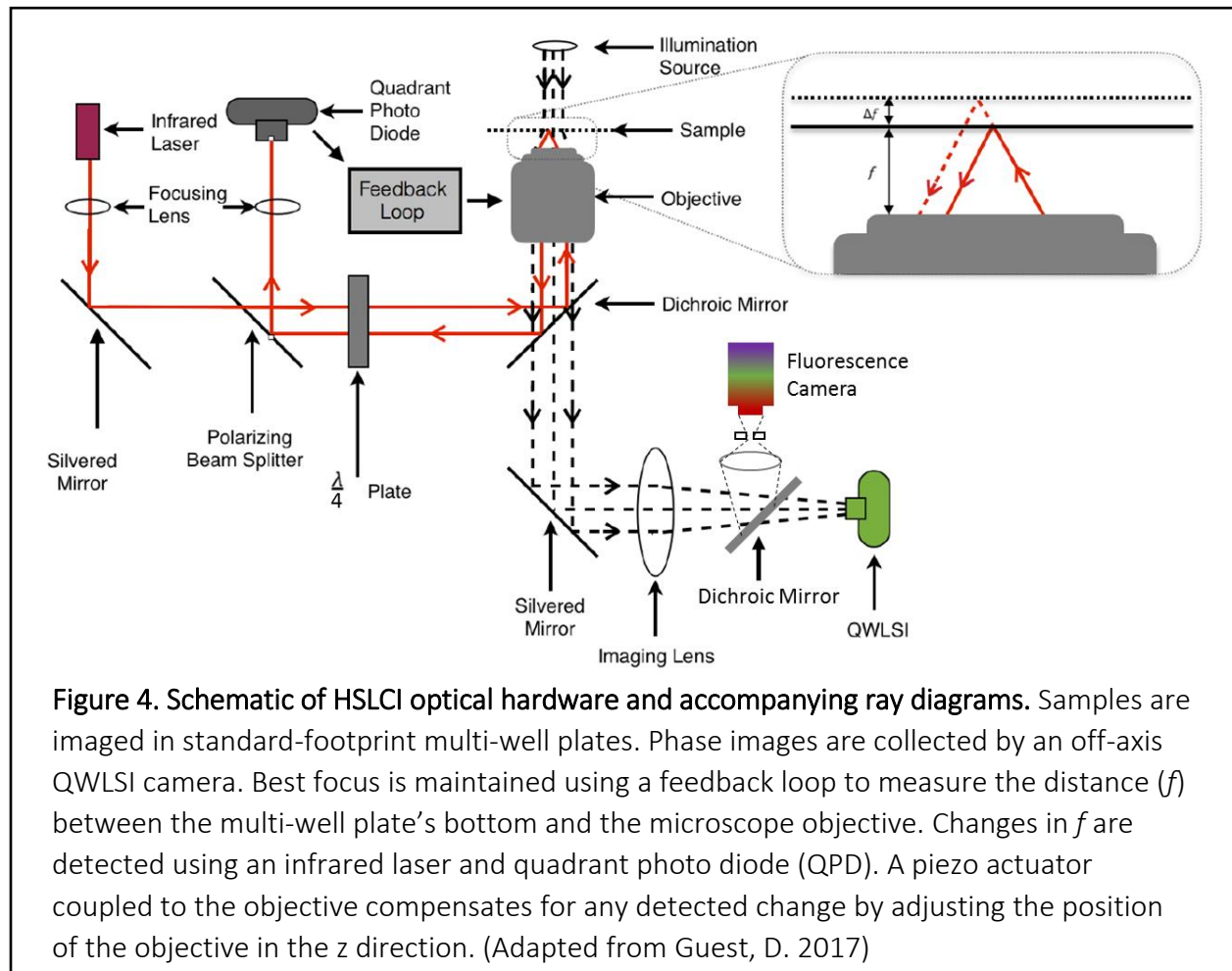
2.3 Image Analysis

Briefly, raw interferograms acquired by the SID4BIO are converted to phase images using the manufacturer's software and then analyzed with our custom MATLAB (Mathworks, Inc.) scripts. The phase calculation down-samples the raw interferogram image to 400 x 300 pixels, resulting in effective pixel sizes between 1.3 μm and 2.5 μm , depending on the objective.

The intensity signal across the phase image matrix is deconvolved in the Fourier domain around the spatial period of the diffraction grating to generate an unwrapped phase image. This a phase gradient that is then numerically integrated to derive the optical path difference. The optical path difference (OPD) is defined as a function of the spatial position in the wavefront.

$$OPD(x, y) = \int_0^h [n(x, y) - n_{medium}] dz$$

Here, n is the refractive index of the specimen and n_{medium} is the refractive index of the medium.



The difference is integrated over the total thickness h in the direction of propagation. As the resulting value is a combination of OPD from the sample and the OPD from the imaging system, a

reference image is captured prior to imaging the sample; we eliminate any contribution from the imaging system by subtracting the reference image. The OPD is then used to derive the optical volume difference OVD, wherein the OPD is integrated over the total imaging surface (S). Hence,

$$OVD = \iint_S OPD(x, y) dx dy$$

This value is directly proportional to the dry mass of the cell (referred to herein as “biomass”) by a constant known as the specific refractive increment α . The specific refractive increment is the rate of change in the refractive index n of a specific specimen.

$$\iint_S OPD(x, y) dx dy = \alpha \cdot m$$

This can be rearranged as

$$m = \frac{1}{\alpha} S \cdot OPD$$

to find the mass (m), where S is the surface area of the specimen in microns. For the experiments described herein, $\frac{1}{\alpha}$ is equal to $5.56 \frac{pg}{\mu m^3}$.⁴⁸

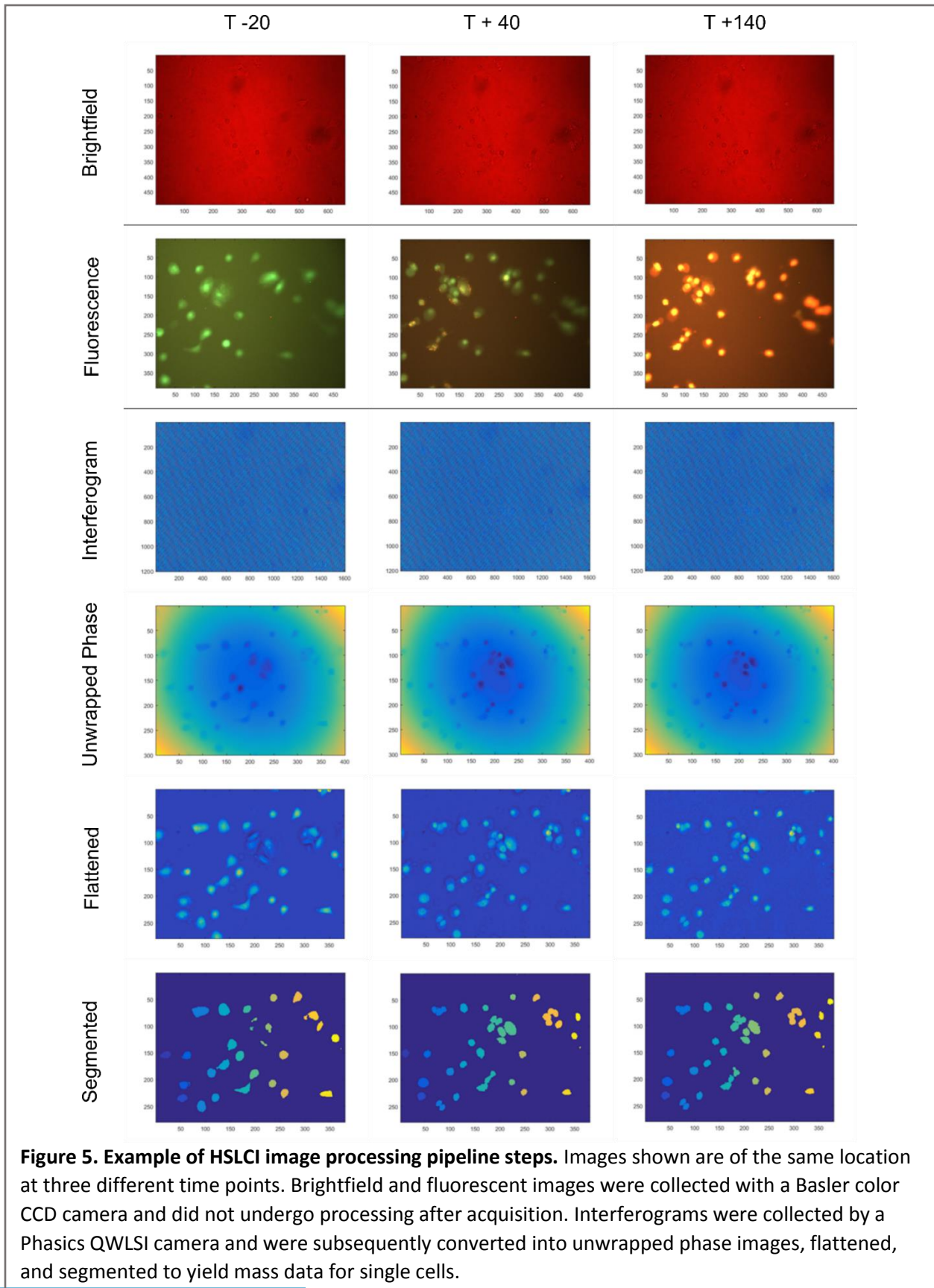
Computed phase images are “flattened” by correcting for low-frequency background noise inherent to the shearing interferometry method. Single cells are segmented from the background of the flattened phase images using a spatial-derivative edge detection kernel; their locations and optical volumes are recorded. An example of step-wise images from this process is provided in

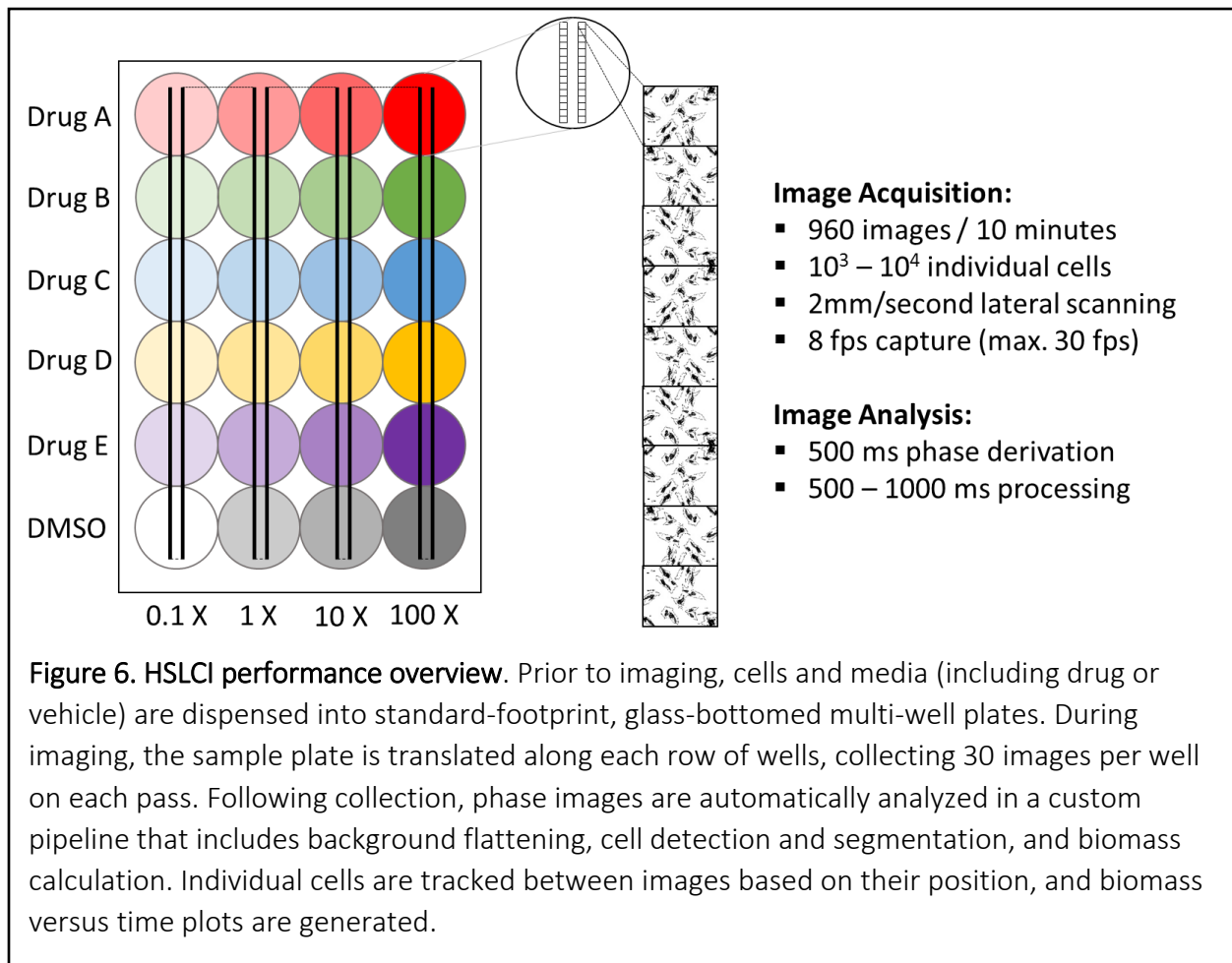
Figure 5.

Frame-to-frame cell tracking is accomplished with a previously-described particle tracking algorithm.⁷⁸ Single-cell growth tracks are quality filtered using an upper cutoff of +/-15% uncertainty (SD of residuals) in the calculated growth rate, as determined by linear fitting the dry mass versus time data.

2.4 HSLCI Platform Performance Metrics

In its current configuration, the HSLCI system can, at a minimum, collect and process 960 images from as many unique locations in a multi-well plate every 10 minutes, yielding biomass data on at least 10^3 – 10^4 individual cells. Due to the mechanical and environmental stability of the HSLCI system, we have been able to track single cells and cell clusters for up to 10 days, with no time limit yet found. The HSLCI's stages enable lateral scanning at a maximum velocity of 2mm per second, while the SID4BIO camera is capable of capturing data at rates up to 30 fps. For a 24-well plate, even at a capture rate of 4 fps, this translates to only 2.5 minutes needed to acquire 240 unique images (40 images/well) in a single six-well column. After acquisition, deriving a phase image from a single raw interferogram typically requires 500 ms, while the remainder of post-processing (flattening, cell segmentation, and cell tracking) typically requires 500-1,000 ms, on a single Intel Core i7 processor. Compared to our prior implementations, our current pipeline conducts image processing as soon as images are acquired and parallelizes these steps across eight or more processors on a single high-performance PC, resulting in near real-time processing. An overview of the HSLCI imaging and data analysis pipeline is provided in **Figure 6**.





Chapter 3

Quantifying Melanoma Drug Resistance and Heterogeneity

3.0 Chapter Overview

This chapter details the deployment of HSLCI during a multi-year study on drug resistance and heterogeneity in patient-derived melanoma cell lines. This project was planned and executed in close collaboration with the Dr. Michael Teitell's laboratory at the University of California – Los Angeles (UCLA). The text and figures that follow have been adapted (reproduced with permission of The American Chemical Society and co-authors) from a publication of the study's results, co-first authored by K. Leslie and D. Huang, in the journal *Analytical Chemistry*.⁸¹

3.1 Introduction

An estimated 91,270 new cases of cutaneous melanoma with 9,320 deaths will occur for the United States in 2018.⁸² Despite comprising less than 2% of skin cancer diagnoses, melanoma is responsible for 75% of skin cancer deaths.⁸³ Genetic landscape studies show inter-patient, intra-patient, and intra-tumor heterogeneity. About 50% of melanomas harbor an activating mutation in the BRAF gene, whereas 10-25% of cases show an activating RAS mutation, 12-18% are mutant in NF1, and 7-28% of tumors show mutations in genes that include AKT and PTEN. Most of these mutations increase MAPK pathway signaling activity, which regulates cell proliferation, differentiation, and survival.⁸⁴⁻⁸⁷ Targeted therapies, most notably against BRAF V600E and V600K activating mutations, have improved progression-free survival for many melanoma patients.⁸⁸ However, therapy resistance emerges in most cases of BRAF or MEK inhibitor monotherapy, often from preexisting or acquired mutations that reactivate the MAPK pathway downstream of the drug-targeted site.⁸⁹ Current BRAF and MEK inhibitor combination therapies aim to reduce the frequency of emergent resistance.^{90,91} Drug selection guidance comes from

clinical tumor staging, mutation screening, patient health, and prognostic factors such as lactate dehydrogenase levels.⁹² Despite multifactorial guidance, resistance eventually develops even for up to 80% of patients receiving combination therapy.⁸⁸ Genetic heterogeneity underlying mechanisms of preexisting and acquired resistance makes mutation screening incompletely predictive of drug susceptibility, both prior to the start of therapy and after the development of resistance, and increases the difficulty of selecting efficacious frontline and second-line therapies.^{93–95}

Current efforts in repeat tumor assessment focus on noninvasive liquid biopsy methodologies such as the detection and analysis of circulating exosomes, microRNAs, circulating tumor DNA, circulating tumor cells, and proteomic profiling of serum proteins by mass spectrometry.^{96,97}

While samples from the circulation provide easily accessible materials that may be more representative of a patient's tumor heterogeneity than single-site tumor biopsies, there are presently no reliable molecular biomarkers from circulation sampling to guide targeted melanoma therapy or improve outcome predictions.^{98–100} Other limitations include a lack of standardization, low sample yields, and the high cost of post-isolation analyses, which makes many circulation-sampling methods impractical for broad-scale clinical implementations in their present state.^{101,102}

An alternative to circulating biomarkers is the *in vitro* measurement of drug responses in excised tumor cells using chemosensitivity assays, such as ATP quantification or assessments of cell metabolic activity.^{103–106} Advocated by major cancer centers and international research organizations, such as the American Society of Clinical Oncology (ASCO), chemosensitivity assays have seen minimal adoption in melanoma treatment. This is due to long, three-to-seven day

turnaround times that increase the likelihood of artifacts, a lack of supporting large-scale clinical trials, and interference from heterogeneous co-harvested tumor elements (such as stromal fibroblasts) that often overrun cultures and may result in false or misleading data.^{107–111} Further, the most popular cell death assays using ATP or MTT measurements are bulk methods, which is a significant limitation for typically-heterogeneous cancers, especially given that growth arrest and senescence (rather than sudden cell death) are common drug responses and resistance mechanisms.^{108,111–114} By contrast, acute cell killing assays can provide data at a snapshot in time using fresh tissue, but have not proven sufficiently informative as stand-alone assays.^{115–119}

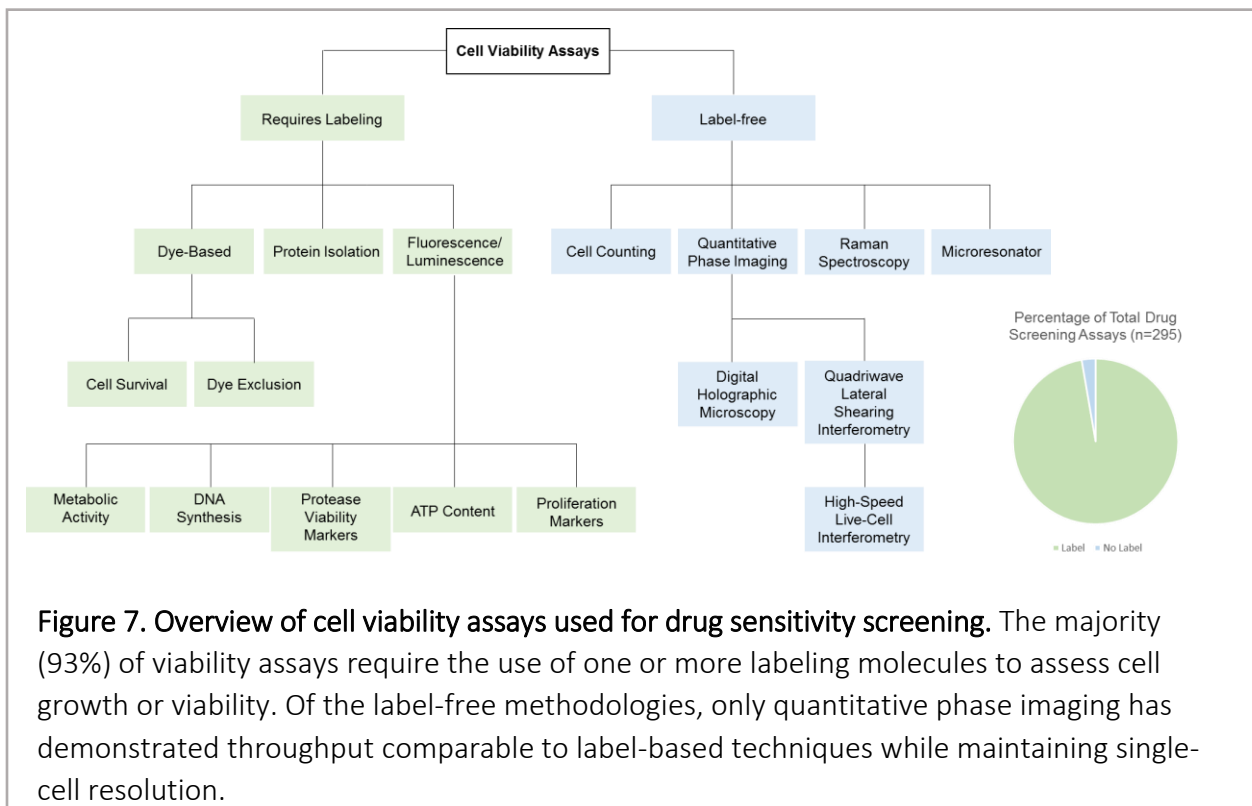
High-content screening systems based on confocal microscopy, such as the commercially-available GE In Cell Analyzer (General Electric, Inc., Boston, MA) and Yokogawa CV8000 (Yokogawa Electric Corporation, Tokyo, Japan) platforms, were introduced as a versatile solution to many of these problems through their combined use of automation, environmental controls, and compatibility with a variety of assays. Unfortunately, these systems still require that cells be labeled for chemosensitivity and cytotoxicity testing. A superior, high-throughput, reproducible, standardized, and inexpensive approach to determine drug sensitivity before (and periodically during) therapy is, therefore, desirable.

A variety of *in vitro* and *ex vivo* methodologies have emerged to address the shortcomings of these traditional cell viability assays in the context of personalized cancer care (**Figure 7**).

Specifically, newer strategies have focused on reductions in turnaround time and sample quantity via microfluidics, a more accurate simulation of the tumor microenvironment, and novel non-genetic biomarkers of drug sensitivity.^{120–122} Despite progress in these areas, the

field has not yet achieved the required combination of accuracy, throughput and single-cell sensitivity needed for predictive assays to guide cancer treatment selection

We have previously shown that optical interferometric microscopy provides an exciting potential solution by profiling drug-induced growth arrest in living single cells or cell clumps via changes in biomass over time with picogram sensitivity.^{25,78} However, this proof-of-principle work consisted of single agent, small-scale studies of limited duration. The key remaining engineering challenge is to create a reliable platform for multi-agent, multi-concentration parallel screens without sacrificing measurement accuracy or assay acceleration. Meeting this challenge

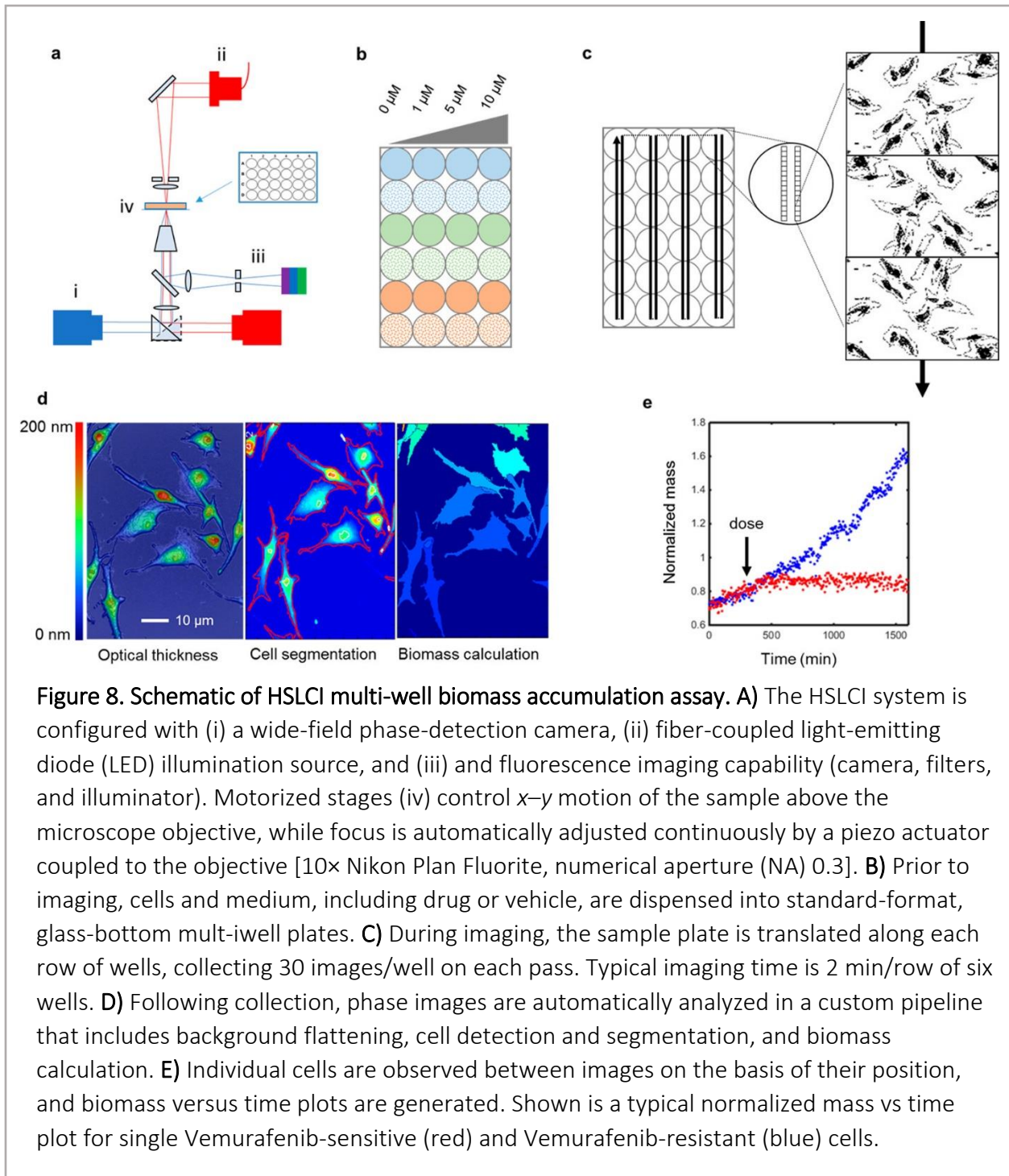


requires, at a minimum, an order of magnitude increase in the number of different conditions tested within a single experiment, and a corresponding increase in the number of individual cells analyzed per hour. This is a sizable hurdle, for a variety of methodological reasons, but is

absolutely required to enable practical, rapid response profiling of patterns of drug resistance, intra-tumor heterogeneity and for ultimately developing a reproducible therapy selection method.

To reach this goal, we created and deployed the HSLCI (**Figure 8**). HSLCI's dynamic focus stabilization enables continuous image collection over the entire sample area without pause, and stage-top or whole microscope enclosures provide long-term environment stability for imaging under physiology-approximating conditions (37 °C, 5% CO₂). The HSLCI captures images from standard format, glass bottom multi-well cell culture plates and each well can contain a different cell type exposed to a unique drug dose or combination. The experiments described here utilized 4-well and 24-well glass bottom plates, although well counts of up to 96 are possible depending on the experimental conditions, including cell concentration, population sampling depth, required temporal resolution, and other parameters. This present work describes a two-center study using HSLCI to quantify biomass kinetics for three isogenic sensitive/resistant pairs of patient-derived, V600EBRAF mutant melanoma cell lines in response to the BRAF inhibitor (BRAFi), Vemurafenib, and a battery of FDA-approved kinase inhibitors. We show that HSLCI-quantified biomass kinetic signatures during 24 hours of drug exposure discriminates between drug-sensitive and drug-resistant tumor subpopulations. HSLCI data are reproducible between study sites and consistent with longer multi-day growth inhibition assays.

Of particular practical importance for any future clinical laboratory use is HSLCI's compatibility with pre-sterilized, disposable, and standard format multi-well sample plates. This enables



efficient screening of multiple drugs and drug combinations in a single assay, simplifies sample handling, and avoids the need to sterilize and wash dedicated microfluidic components between runs.

3.2 Methods

Cell Lines

M229P, M229R5, M238P, M238R1, M249P and M249R4 cell lines were grown in DMEM high glucose with 10% heat-inactivated FBS (Omega Scientific) and 2mM glutamine in a 37 °C, humidified, 5% CO₂ incubator. M229R5, M238R1 and M249R4 cells were exposed to 1 μM Vemurafenib every 2 – 3 days. Cell counting from 6-well plates with controls and a range of Vemurafenib concentrations was performed for five days following overnight seeding.

Population Kinetic Response Experiments

Cells were synchronized by growing to confluence in 75mL tissue culture flasks and collected using a “shake-off” technique that involved repeated tapping of the flasks against the palm to loosen partially-adherent (i.e. dividing) cells. Cells were plated at 1×10^5 cells/ml in 25 mm dishes and incubated overnight. Prior to imaging, samples were equilibrated thermally for one hour on the microscope stage, then imaged for three hours, after which either 0.1% DMSO vehicle control or 5 μM Vemurafenib was administered and dishes imaged for another 25 – 30 hours.

Vemurafenib dose response experiments. Cells were first synchronized by shake-off, and each of the six melanoma cell lines seeded into four wells each of a 24-well glass bottom plate at 1×10^5 cells/ml, and incubated overnight. Each line was dosed with 0.1% DMSO carrier control, or 1 μM, 5 μM, or 10 μM Vemurafenib. Cells were incubated for 24 hours, then the entire plate was imaged on the HSLCI for 10 hours.

Fluorescence Mixing Experiments

1.25 x 10⁴ M249P and M249R4-GFP cells were added together in a total volume of 1mL tissue culture media. 0.7 mL of the mixture was dispensed into each well of an Ibidi 4-well Ph+ μ -slide. Cells settled over 6 hours after which 5 μ M Vemurafenib was added to each well. Ibidi oil sealed the liquid opening of each well before the plate was placed onto the LCI stage. All wells were imaged continuously for 48 hours. Fluorescence images were taken using a Hamamatsu EM CCD camera (C9100-02 EMCCD) serially after every 5 phase imaging loops were completed. Green fluorescence was captured using a 38 HE Green Fluorescent filter set (Zeiss) with an excitation wavelength of 450-490 nm, a beam splitter wavelength of 496nm and an emission wavelength of 500-550 nm. Fluorescence excitation was provided by an X-Cite® 120Q wide-field fluorescence microscope excitation light source (Excelitas).

Kinase Inhibitor Panel Assay

M249R4 cells were plated in a 24-well optical glass-bottomed plate (Cat.# P24-0-N, Cellvis) at 1 x 10⁴ cells/ml (total of 1 mL in each of 24 wells) in media (DMEM, 10% Fetal Bovine Serum, 2 mM L-Glutamine) containing 1 μ M Vemurafenib. Plated cells were allowed to adhere overnight at 37 °C, 5% CO₂. All cells were washed with 1x phosphate-buffered saline, pH 7.4, and provided with fresh media. Immediately following washing and feeding, cells were dosed with inhibitors at dose-escalating concentrations and incubated under standard cell culture conditions for 24 hours. After incubation, cells were imaged for 10 hours using the HSCLI system.

3.3 Results

Isogenic BRAFi-Sensitive and –Resistant Melanoma Cell Lines

We evaluated three patient-derived V600EBRAF melanoma cell lines, M229P, M238P, and M249P, which are sensitive to the BRAFi, Vemurafenib ($IC_{50} < 1 \mu M$), and their isogenic, BRAFi-resistant sub-lines, M229R5, M238R1, and M249R4, created by Vemurafenib co-incubation over time (**Supplementary Table 1**). M229R5 and M238R1 developed BRAFi resistance via epigenomic reprogramming, which is thought to occur in regressing or residual melanoma tumors from patients treated with MAPK inhibitor (MAPKi) therapy. This non-genomic evolution results in a MAPK-redundant form of resistance.³³ On the other hand, M249R4 acquired a Q61K NRAS mutation in addition to the V600EBRAF mutation. This concurrent BRAF/NRAS mutant configuration results in MAPK hyper-activation and a MAPK-addicted form of resistance, which is frequently detected during disease progression or with clinical relapses.³⁴⁻³⁶ Thus, these pairs of cell lines represent pre- and post-treatment models of differential drug-sensitivity states that are clinically relevant and, therefore, we used these lines to evaluate HSLCI performance in biomass profiling.

Biomass Kinetic Responses to Vemurafenib Exposure

Our previous work in breast cancer and multiple myeloma indicated that changes in the population median growth rates between sensitive and resistant cell lines is detectable with confidence within a few hours of drug exposure.^{25,78} We also showed that the distribution of growth rates within a population is roughly Gaussian, in both treated and control samples. There is no existing data for the rate of biomass change of BRAFi-sensitive or -resistant melanoma cells that grow as adherent single-cells or clumps. Therefore, we measured the kinetics of Vemurafenib response in the three paired, molecularly characterized melanoma lines using HSLCI, to establish rates and distributions of biomass change with or without drug

exposure. First, we performed a standard multi-day dose-escalation cell-counting assay to confirm sensitivity for the three parent and matched resistant lines at 1.0 μM to 10.0 μM Vemurafenib exposure (**Supplementary Figure 2**). As anticipated, the parental lines slowed and the matched resistant lines continued replicating with drug exposure. We next used 5 μM Vemurafenib as the mid-point drug dose to measure the median population growth rate and cell mass by HSLCI for the six cell lines in the first 25 hours of drug exposure, in order to quantify the average population kinetic response (**Figure 9-A**). Under these conditions, drug sensitivity of the M249P population was detectable as early as six hours, while sensitivity of the M238P and M229P populations was detected at approximately 15 hours. Significant growth rate reduction occurred in all three parental lines by 20 hours. We observed significant natural variation in the growth rates of individual cells within each population, a result consistent with previous LCI studies. The distribution of single cell hourly growth rates was typically symmetrical about the mean, with variation of roughly +/- 1% (SD) above and below the population mean. For example, plotting the M249P growth rate distribution obtained by HSLCI for each hour showed no change in the population median growth rate nor in the cellular growth rate distribution over the course of the 25 hour experiment. (**Supplementary Figure 3-A**) In contrast, under the same conditions 5 μM Vemurafenib exposure showed population growth rate heterogeneity and a decline below zero growth rate by about 15 hours for >50% of cells (**Supplementary Figure 3-B**), indicative of the relative sensitivity of this line to the BRAF inhibitor. Similar temporal single cell growth rate distributions were seen in the other five cell lines, with kinetics proportional to the line's overall median sensitivity. These results reproduced at both experimental sites with independently assembled HSLCI platforms.

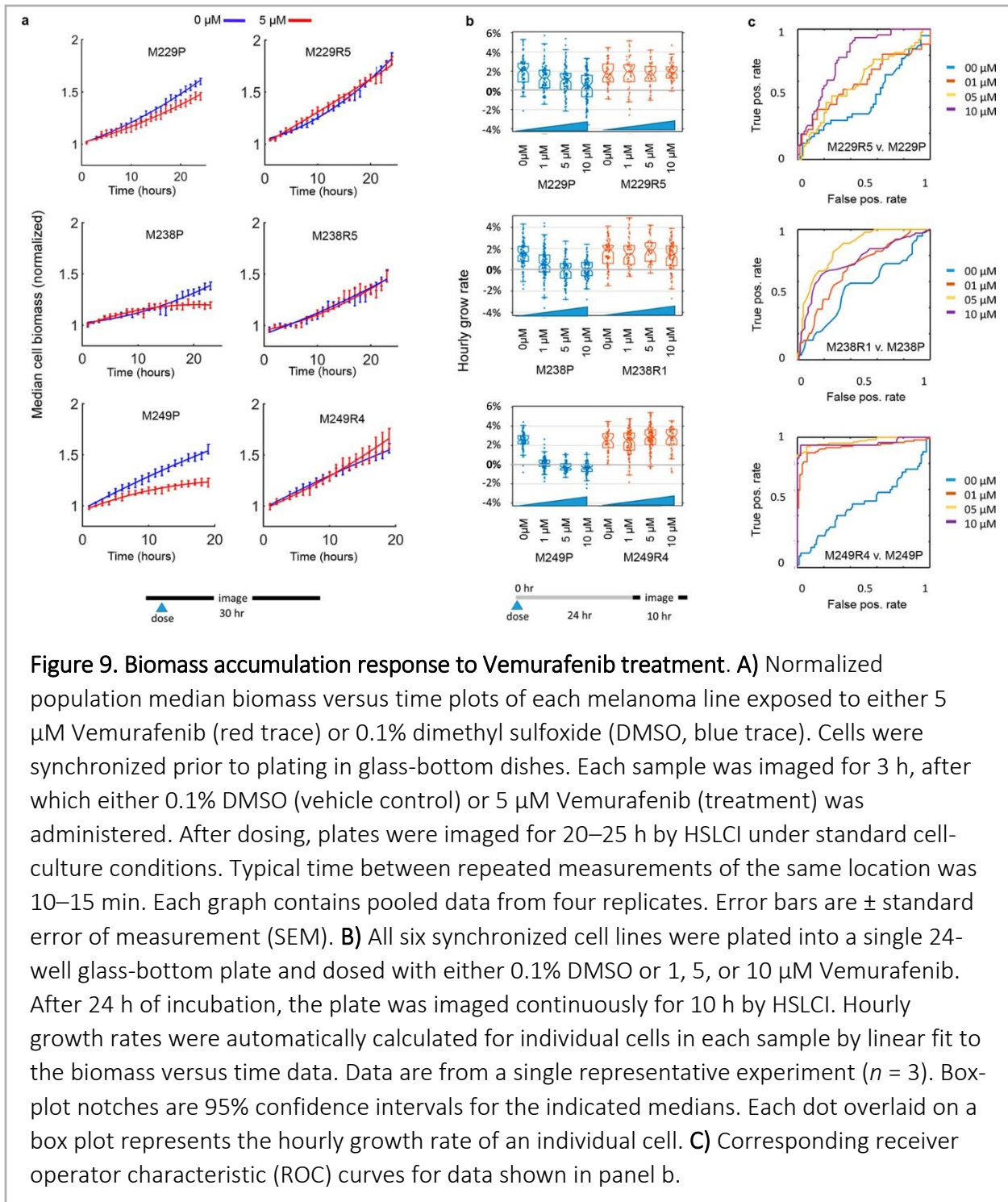
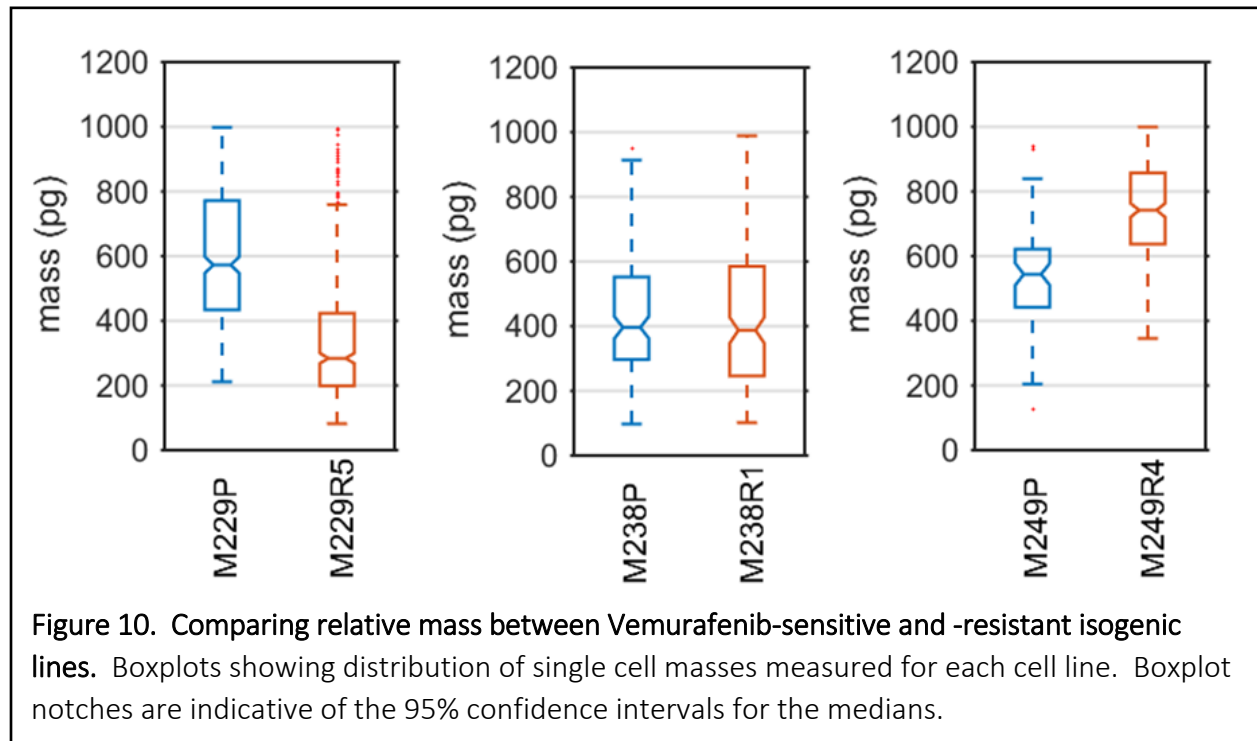


Figure 9. Biomass accumulation response to Vemurafenib treatment. A) Normalized population median biomass versus time plots of each melanoma line exposed to either 5 μM Vemurafenib (red trace) or 0.1% dimethyl sulfoxide (DMSO, blue trace). Cells were synchronized prior to plating in glass-bottom dishes. Each sample was imaged for 3 h, after which either 0.1% DMSO (vehicle control) or 5 μM Vemurafenib (treatment) was administered. After dosing, plates were imaged for 20–25 h by HSLCI under standard cell-culture conditions. Typical time between repeated measurements of the same location was 10–15 min. Each graph contains pooled data from four replicates. Error bars are \pm standard error of measurement (SEM). **B)** All six synchronized cell lines were plated into a single 24-well glass-bottom plate and dosed with either 0.1% DMSO or 1, 5, or 10 μM Vemurafenib. After 24 h of incubation, the plate was imaged continuously for 10 h by HSLCI. Hourly growth rates were automatically calculated for individual cells in each sample by linear fit to the biomass versus time data. Data are from a single representative experiment ($n = 3$). Box-plot notches are 95% confidence intervals for the indicated medians. Each dot overlaid on a box plot represents the hourly growth rate of an individual cell. **C)** Corresponding receiver operator characteristic (ROC) curves for data shown in panel b.

By comparing the median cell mass of the Vemurafenib-resistant melanoma lines to the mass of their isogenic, drug sensitive parent lines, we found no consistent correlation between mass

and resistance (**Figure 10**). This observation stands in contrast to a recent report of cell mass-drug resistance correlation in a mouse AML model, as measured by microfluidic devices.¹²³ However, that study did not compare isogenic, paired sensitive and resistant tumor lines, and it remains to be determined whether or not mass itself is a useful metric of drug sensitivity.



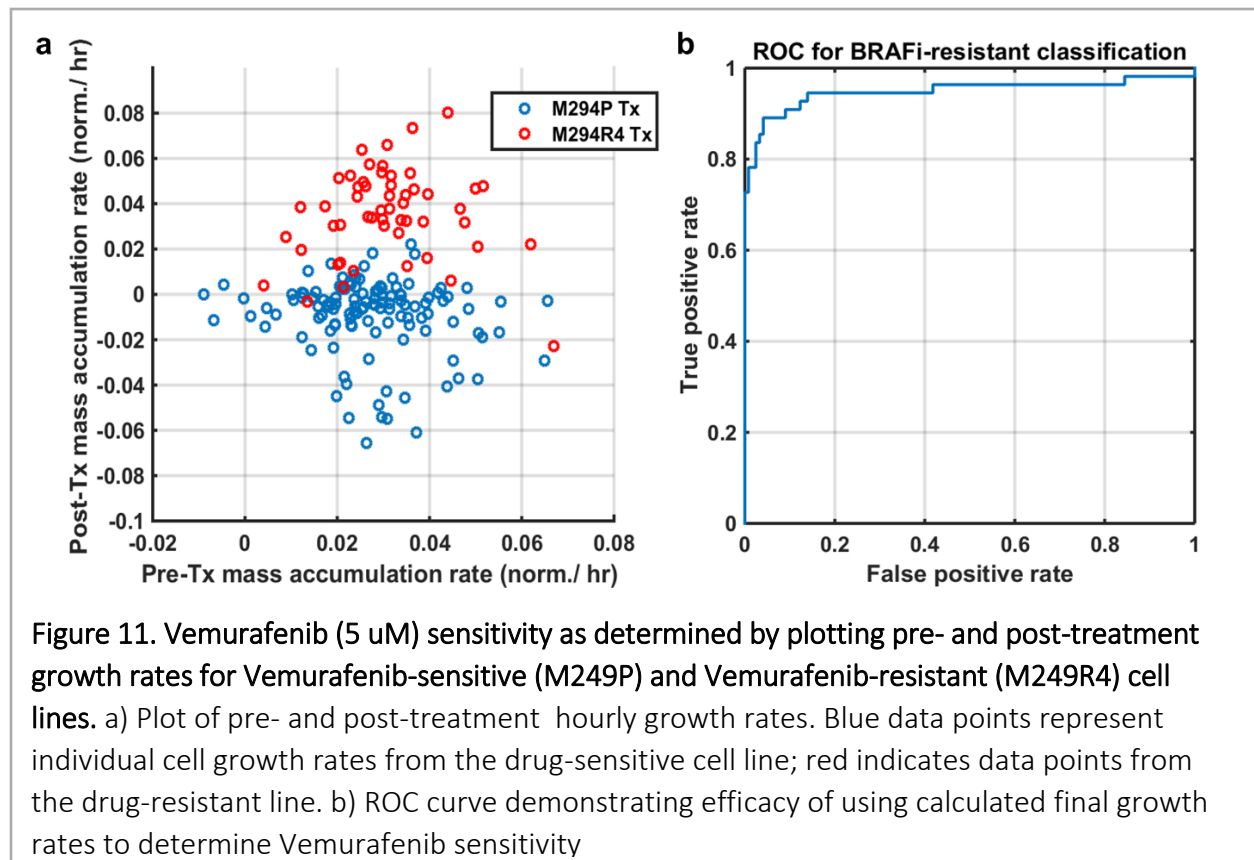
The mid-point kinetic response data suggested that Vemurafenib sensitivity, or lack thereof, would be distinguishable for all lines in a drug-escalation assay, as would be expected for cell counting, by measuring changes in sample growth rates after 24 hours of drug exposure. To test this hypothesis, and to examine the HSLCI methodology for multi-dose and multi-agent screening, we collected short-term, 10-hour growth rate measurements of all three cell line pairs in parallel, at escalating Vemurafenib doses, using a 24-well format. All six melanoma cell lines were dosed with 0.1% DMSO, or 1 μ M, 5 μ M, or 10 μ M Vemurafenib. The parental lines (M229P, M238P, and M249P) showed a clear pattern of increasing growth inhibition at

escalating drug concentrations, whereas the resistant lines (M229R5, M238R1, and M249R4) showed no growth inhibition over the drug dosing range compared to a vehicle DMSO control, consistent with cell counting assays (**Figure 9-B**).

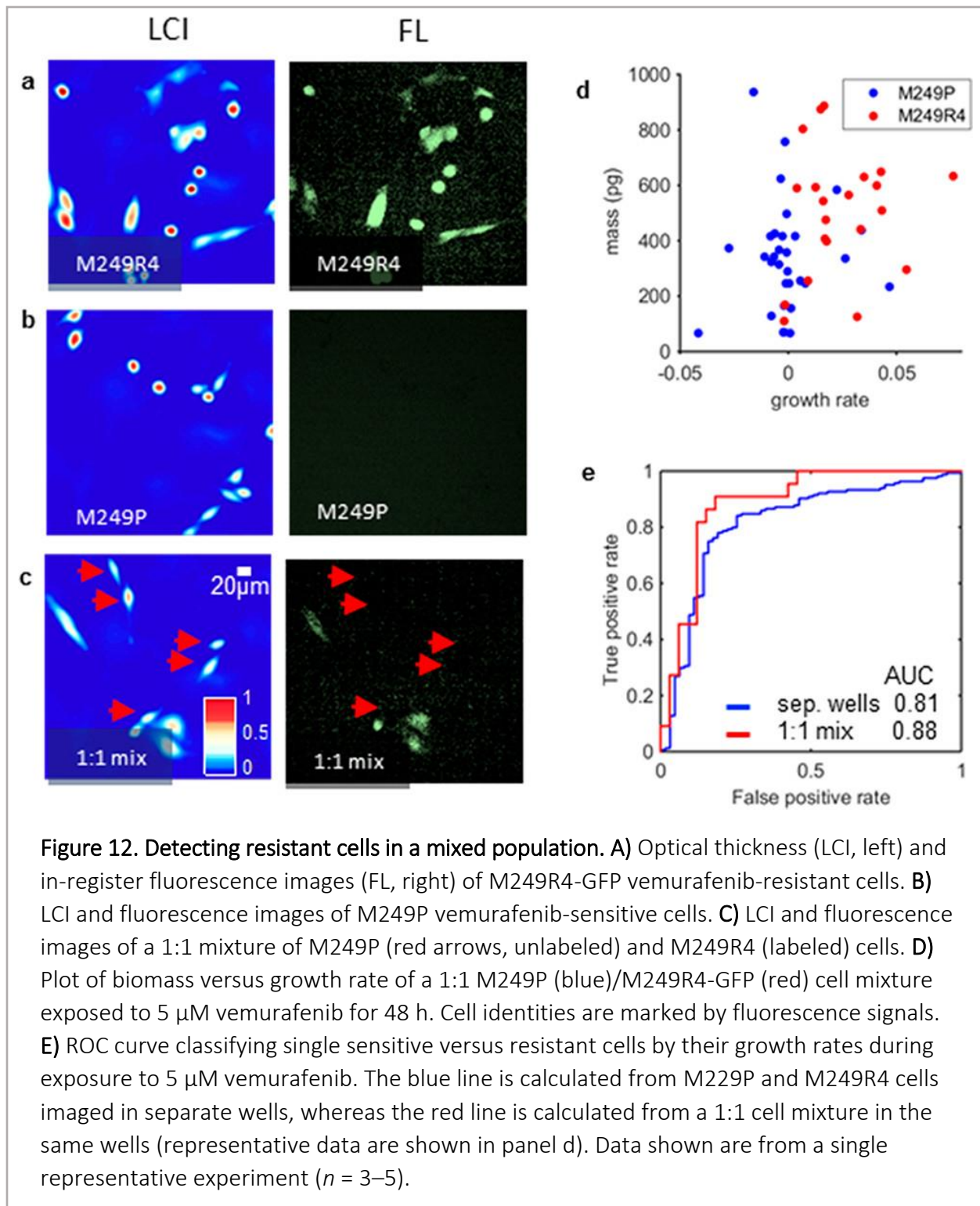
Heterogeneity Quantification

We used Receiver Operator Characteristic (ROC) analysis to determine the ability to distinguish individual resistant cells from sensitive cells, in an in silico mixture, by changes in their individual growth rates during exposure to Vemurafenib. (**Figure 9-C**) This analysis indicated that cells from both M229P and M238P lines were distinguishable from their resistant derivative counterparts at Vemurafenib doses of 5uM (area under the curve (AUC), 0.60 and 0.85, respectively) and 10uM (AUC, 0.78 and 0.75, respectively). The M249P cells were the most sensitive to drug and easily distinguishable based on changes in growth rate, with AUC greater than 0.90 at Vemurafenib doses of 1uM and above (**Figure 11**).

We then deployed HSLCI to quantify the changes in growth rates of an actual mixed population of GFP-labeled M249R4 Vemurafenib-resistant (M249R4-GFP) and unlabeled M249P Vemurafenib-sensitive cells during drug exposure. Importantly, stable GFP-expression in the M249R4 line did not significantly alter the growth rate distribution obtained by LCI for each hour of 5µM Vemurafenib exposure compared with unlabeled M249R4 cells (**Supplementary Figure 3-C**). Sensitive M249P and resistant M249R4-GFP cells grown together at a 1:1 ratio with 5uM Vemurafenib were imaged over 48 hours (**Figure 12 A-C**).



In mixed culture, individual resistant cells were discriminated from sensitive cells based on differences in growth rates (Figure 12-D) and because the M249R4 cells were GFP marked, they were easily identified relative to the unmarked M249P cells during the assay. Reproducibly, the population growth rate of the M249R4 cells exceeded the population growth rate of the M249P cells, as expected, but each marked and unmarked population also showed outlier cells. A small percentage of M249R4-GFP cells showed zero to slightly negative growth rates, whereas a small percentage of M249P cells showed net-positive growth rates, revealing unanticipated Vemurafenib sensitive or resistant outliers within each bulk population. As predicted from the in silico analysis, ROC analysis confirmed a high level of discrimination between sensitive and resistant melanoma cells (AUC 0.88), even when sensitive and resistant cells were combined in



the same sample wells (Figure 12-E). Similar trends were seen in 10:1 sensitive: resistant mixtures as well (Supplementary Figure 4).

MEK Inhibitors with Vemurafenib-Resistant Melanoma

We performed rapid HSLCI dose response assays in triplicate using a panel of three FDA-approved and two investigational kinase inhibitors tested in clinical trials for treating metastatic melanoma, to simulate selection of salvage therapy for patients who develop resistance to front line Vemurafenib. One inhibitor in the panel targets BRAF, whereas the other four target MEK1 or MEK1/2 (**Supplementary Table 2**). We selected M249R4 cells for study because of its robust growth profile and strong resistance to Vemurafenib. **Figure 13** shows typical results from two individual experimental runs, while **Figure 14** shows results from all repeats fitted to a sigmoid dose response function, for reference. Control DMSO-treated cells exhibited a median growth rate of ~2.5% per hour at 0.1% DMSO concentration (v/v), decreasing slightly to 2% per hour at higher concentrations (0.3%-0.5% v/v). For each targeted kinase inhibitor, the peak tolerated serum concentration (C_{max} (ng/mL)), as measured in clinical trials, is shown on the dose-response curves by an asterisk (*). See **Supplementary Methods** for C_{max} determination detail. As expected for this highly Vemurafenib-resistant line, the BRAFi Dabrafenib showed no growth inhibition as compared to the DMSO control. The MEK1 inhibitor Cobimetinib and the MEK1/2 inhibitor Trametinib were the most effective growth inhibitors: Cobimetinib completely arrested median sample growth at 0.255 μ M concentration, which is roughly one half of the maximum tolerated serum concentration, while Trametinib arrested growth at a concentration between 4 nM and 40 nM, or between 1/10x and 1x C_{max} . MEK1/2 inhibitor Selumetinib arrested growth at 2.55 μ M, equal to 1x C_{max} , while MEK1 inhibitor Binimetinib failed to halt growth at concentrations below 2.91 μ M, or 5x C_{max} , suggesting that Binimetinib would be an unlikely candidate for salvage therapy in this simulated case.

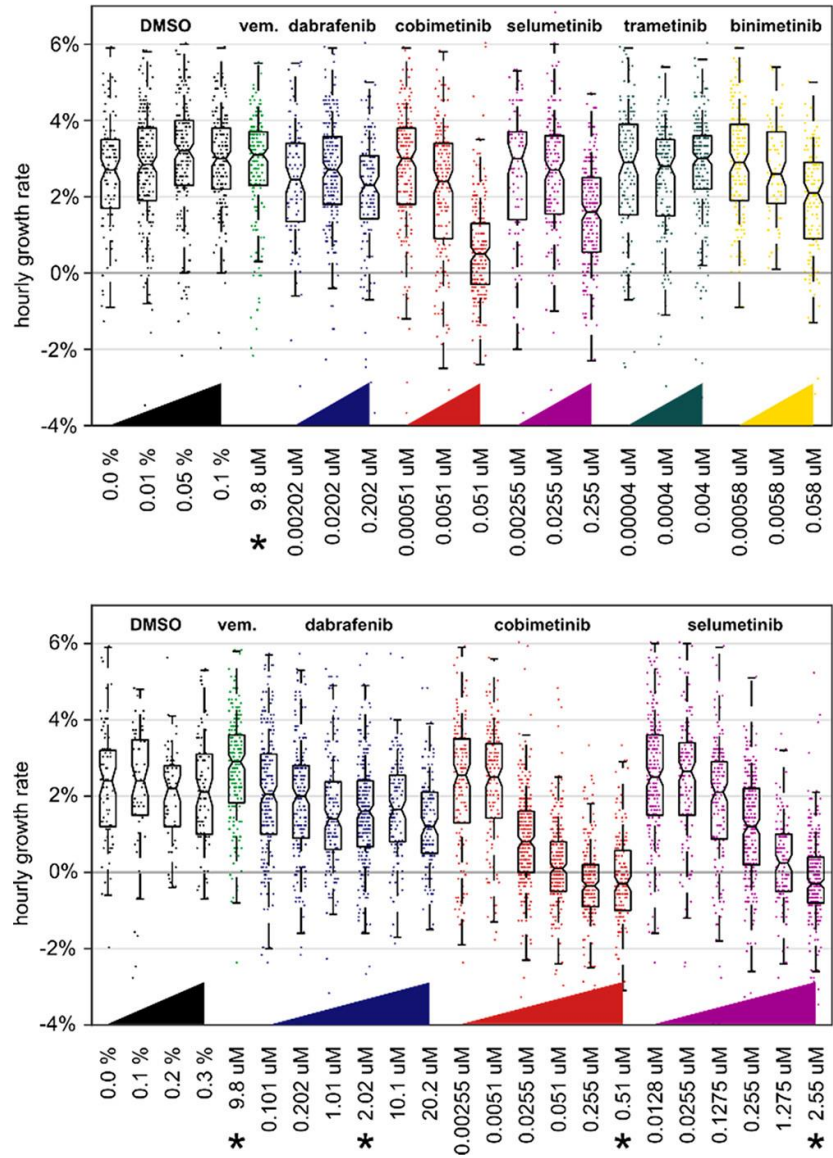


Figure 13. Effects of kinase inhibitors on Vemurafenib-resistant melanoma as measured by HSLCI. M249R4 cells were plated into 24-well plates and dosed at increasing concentrations of each inhibitor. After 24 h of incubation, the plate was imaged by HSLCI continuously for 10 h. Typically, four different doses for each inhibitor, and four DMSO controls, were measured in each run simultaneously. Data in the figure represent two typical experimental runs, using different dose gradations. Hourly growth rates were automatically calculated for individual cells in each sample by linear fit to the biomass vs time data. Each box plot summarizes the hourly growth rates of a population of cells exposed to escalating concentrations of each drug. Individual dots in the underlying scatter plots represent the growth rates of single cells. Boxplot notches are indicative of 95% confidence intervals for the medians. Median number of cells per well: top panel 159 (range 79–216); bottom panel 160 (range 59–294).

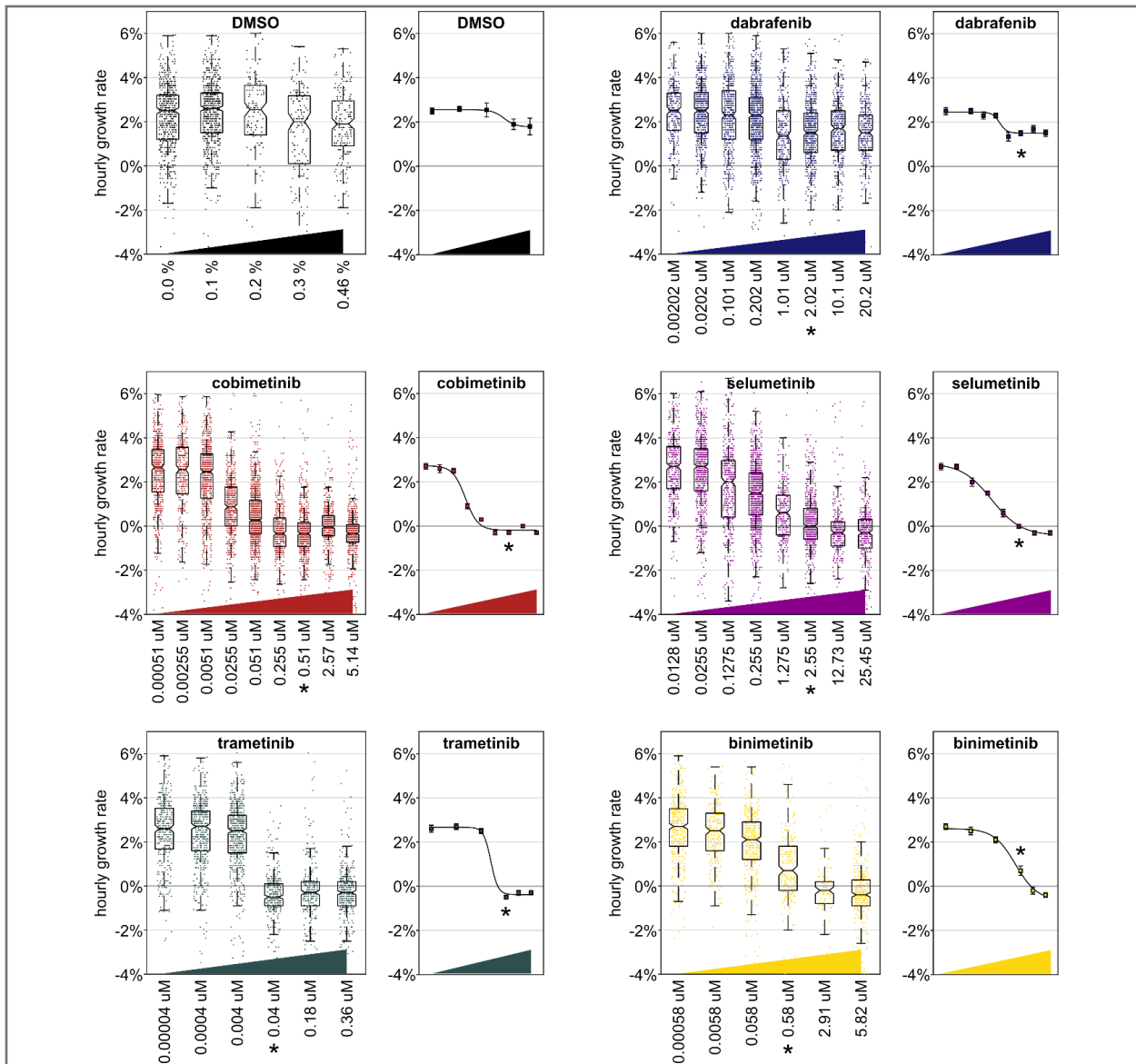


Figure 14. Summary of effect of five kinase inhibitors on Vemurafenib-resistant melanoma as measured by HSLCI. M249R4 cells were plated into 24-well plates and dosed at increasing concentrations of each inhibitor. After 24 hours incubation, plates were imaged by HSLCI continuously for 10 hours. Hourly growth rates were automatically calculated for individual cells in each sample by a linear fit to the biomass versus time data. Data for each drug-dose combination shown represents a sum of three independent replicates. Each boxplot summarizes the hourly growth rates of a population of cells exposed to escalating concentrations of each drug. Individual dots in the underlying scatter plots represent the growth rates of single cells. Boxplot notches are indicative of the 95% confidence intervals for the medians. Median population growth rates from all kinase panel repeats are plotted and fitted with sigmoid curves. Error bars indicate the 95% confidence intervals for the medians. The doses indicated by an asterisk (*) correspond to the maximum serum concentrations (C_{max}) measured in the blood during clinical trials at FDA-approved therapeutic doses. Median number of cells tracked per well per replicate was 159 (range 79 - 294).

3.4 Discussion

Here, we demonstrated the ability of our rapid HSLCI platform to quantify individual cell drug sensitivity in tumor cell populations. This quantification may provide critical data for treatment selections on a whole-tumor population level and can identify specific subpopulation drug sensitivities to predict drug resistance at a single cell level. Our results also show the reproducibility of two similar but distinct implementations by obtaining concordant data from two institutions with independently constructed and standardized HSLCI platforms. This two-center study design is unique amongst live cell response profiling approaches and provides confidence that the newly configured HSLCI has the required consistency for further development towards a clinically useful approach.

In comparison to other single live cell biomass profiling approaches, including our own prior interference microscopy studies, HSLCI represents a substantial technical advance in single cell sampling throughput, cell tracking duration and parallel measurement of multiple agents.^{34,36,74,78} For example, Stevens et al. recently used micro-channel resonators to demonstrate that the combined measurement of single cell mass and growth rates could be used to identify drug resistant cells isolated from an engineered mouse AML model.²⁸ Their high throughput 'next-gen' system with 12 micro-resonators could measure up to 60 cells per hour, where cells are measured serially, each for 15 minutes, resulting in simple 'snapshots' in time. Unfortunately, tumors that grow in small clusters or clumps, as do many melanoma samples, are inaccessible to this platform unless they are disaggregated, which affects their growth characteristics and drug sensitivity. In contrast, HSLCI typically measures between 10^3 and 10^4 cells in each experiment, tracking each cell individually for hours to days, and is well suited to

tumors that grow in clusters or clumps without disaggregation. In addition, identifying rare resistant clones in a population of normal or therapy-sensitive malignant cells will require deep sampling. For instance, typical minimal residual disease detection using multi-color flow cytometry requires sampling to a depth of at least 10^4 and up to 10^6 cells.¹²⁴ We believe that realistic improvements may allow HSLCI throughput to approach 10^5 cells per experiment.

Due to the mechanical and environmental stability of the HSLCI system, we have been able to track single cells and cell clusters for up to 10 days, with no time limit yet found. This is a dramatic increase over our previous 12-hour maximum duration interference microscopy work, and enables studying behaviors that evolve over many minutes, hours or days, encompassing the vast majority of cellular responses. Cell tracking duration is of direct relevance to detecting drug responses in cells isolated from patients, as it is necessary to distinguish between growth-arrest (cytostasis) and death resulting from drug exposure versus other influences. With HSLCI this is accomplished by repeatedly observing individual cells before and after drug exposure-response, a process that requires several hours or more.

The primary drawback of HSLCI compared to microscopic, single cell 'snapshot' fluorescent assays and micro-resonator mass assays is the relatively large data footprint and extensive image analysis required to generate a biologically interpretable result. At present, data analysis time, not hardware capability, is throughput limiting. On the other hand, the single cell images generated by HSLCI are inherently information rich, allowing not only mass accumulation but cytokinesis, motility and cell shape information to be quantitated. Integrating these mutually supporting metrics will be a direction for future research. Furthermore, system upgrades can be

largely accomplished by software rather than hardware modifications, making the upgrade path efficient and flexible.

Chapter 4

CD3+ T Cell Mass Dynamics During Stem Cell Transplantation

4.0 Chapter Overview

This chapter details the use of LCI to analyze T cells extracted from the blood of patients undergoing stem cell transplantation at VCU's Massey Cancer Center. This project was planned and executed in close collaboration with Dr. Amir Toor and Dr. Catherine Roberts. The text and figures that follow have been adapted (reproduced with permission of The Royal Society of Chemistry and co-authors) from a publication of the study's results, first-authored by K. Leslie, in the journal *Analyst*.^{125,126}

4.1 Introduction

Approximately 32,000 allogeneic stem cell transplants (SCTs) from HLA-matched donors are performed annually.¹²⁷ In addition to an increased susceptibility to infection, recipients of these transplants face competing risks of malignancy relapse and graft versus host disease (GVHD). In HLA-matched SCT recipients, GVHD results from the recognition of recipient minor histocompatibility antigens by donor T cells. Despite an evolving understanding of the complexities of these alloreactive T cell responses and significant reductions in non-relapse mortality (NRM), the incidence of GVHD ranges from approximately 10% to 50% for allogeneic SCT recipients.¹²⁸ This is particularly problematic as an increasing number of SCTs are performed each year, matched unrelated donors are utilized in more than half of allogeneic transplants, and increasingly older patients now undergo transplantation using reduced-intensity conditioning where a graft versus tumor (GVT) effect is critical for disease control and GVHD is especially deleterious. Furthermore, no reliable laboratory measures have yet emerged to allow real-time titration of post-transplant immunosuppression on an individualized basis to modulate

competing GVHD and cancer relapse risks. Essential to the development of such measures is an improved understanding of the immunobiological mechanisms underlying discrepancies in GVHD incidence, such as further characterization of the biological diversity of transplant donors and recipients, and efforts to identify a comprehensive marker of post-transplant alloreactivity.^{129,130}

Given the central role of T cell growth and differentiation in SCT, and that of processes known to alter cellular size and shape, one approach to studying alloreactivity in real-time might involve an assessment of donor-derived T cell biophysical properties. It has been shown *in vitro* that CD8+ murine T cells increase their mass upon activation and, further, that cytotoxic T cells transiently increase their mass when effecting cell killing, in a stylized cell culture system.^{58,131} Mathematical modeling by Toor et al. has identified distinct population growth kinetic signatures of lymphocyte recovery that correlate with levels of donor-derived CD3 + T cells and alloreactivity.^{132,133} Further, it has been shown that there are significant metabolic adaptations in T cell subsets upon engagement of an antigenic peptide-HLA complex by the T cell receptor. These metabolic changes include increased glycolysis and oxygen consumption as well as cytokine production.¹³⁴ Higher levels of GLUT 1 expression have been observed in activated T cells, again suggesting increased metabolic & biosynthetic rates.¹³⁵ Indeed, a weak correlation has been shown between intracellular ATP concentration in T cell subsets and severity of clinical GVHD in humans and between increasing glycolysis and GVHD in murine models.^{136,137} These results suggest that T cell activation and consequent metabolic, biosynthetic, and, logically, mass changes, may correlate with significant functional events in the SCT immune reconstitution process, as donor-derived T cells experience a new antigenic milieu, post-transplant.

At the time of this study, the HSLCI was still under development. Therefore, using the lower-throughput LCI system, we measured biomass in populations of CD3 + T cells isolated from hematopoietic stem cell transplant patients, at various times pre and post-transplant, with an aim to identify kinetic signatures associated with immune reconstitution and GVHD.

4.2 Methods

Consecutive patients undergoing myeloablative conditioning and stem cell transplantation between May 2015 and May 2016 were enrolled on a prospective study approved by Virginia Commonwealth University's Institutional Review Board (VCU-IRB #HM20004916) (**Table 1**). Patients gave informed consent for stem cell apheresis product and whole blood sample collection, and for rabbit anti-thymocyte globulin (Thymoglobulin) either 3.5 mg kg⁻¹ (MRD) or 5 mg kg⁻¹ (MUD) starting from day-3 to day-1. GVHD prophylaxis was with either tacrolimus or cyclosporine in combination with methotrexate (MTX) or mycophenolate mofetil (MMF). Antimicrobial and antifungal prophylaxis was administered. Routine surveillance for cytomegalovirus (CMV) and Epstein Barr virus (EBV) was carried out using PCR. Donor cell chimerism was studied using short tandem repeat sequence PCR. Average T cell chimerism for allogeneic transplant recipients was 90% at 30 days post-transplant (T30), 99% at 60 days post-transplant (T60), and 99% at 90 days post-transplant (T90). Donor-derived CD3 + T cell (ddCD3) counts were calculated as previously reported.¹³⁰ Average ddCD3 cell counts were 571 cells per μ l, 1417 cells per μ l, and 1019 cells per μ l at 30, 60, and 90 days post-transplant, respectively.

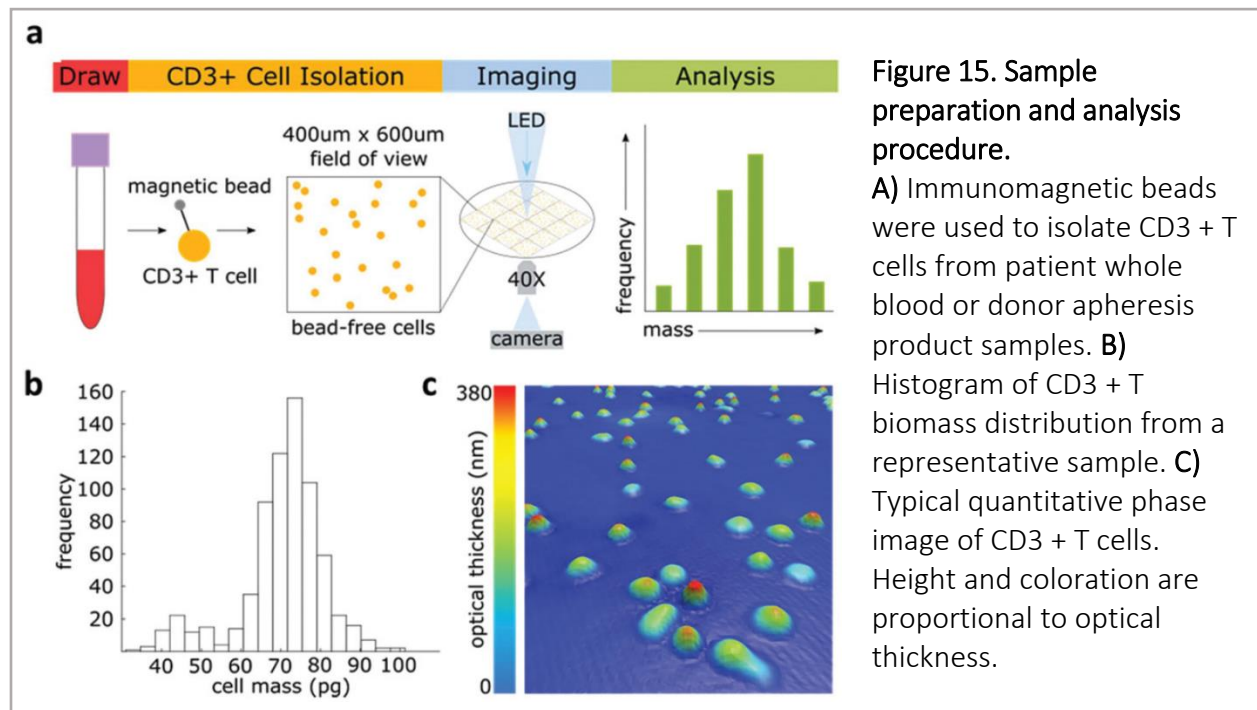
| Table 1. Patient demographics | |
|--|-------------------------|
| | n=18 |
| Median Age, y (range) | 49 (24-65) |
| Gender | |
| Female | 9 |
| Male | 9 |
| Disease | |
| Acute lymphoblastic leukemia | 3 |
| Hodgkin's Lymphoma | 2 |
| Myelodysplastic syndromes | 4 |
| Chronic myelogenous leukemia | 1 |
| Non-Hodgkin's Lymphoma | 3 |
| Acute myeloid leukemia | 2 |
| Multiple myeloma | 1 |
| Myelofibrosis | 2 |
| Donor Type | |
| Matched unrelated | 11 |
| Matched related | 3 |
| Autologous | 4 |
| Conditioning Regimen | |
| TBI/Cyclophosphamide | 2 |
| Busulfan/Cyclophosphamide | 6 |
| Busulfan/Fludarabine | 4 |
| Fludarabine/Melphalan | 2 |
| BEAM | 3 |
| Melphalan | 1 |
| CMV Status (Donor/Recipient) | |
| +/+ | 7 |
| +/- | 3 |
| -/+ | 4 |
| -/- | 0 |
| GVHD Prophylaxis | |
| Tacrolimus-Methotrexate | 6 |
| Tacrolimus-Mycophenolate mofetil | 4 |
| Cyclosporin A-Methotrexate | 2 |
| Cyclosporin A-Mycophenolate mofetil | 1 |
| Median CD34 Dose (E6 cells/kg) (range) | 4.59 (3.11-9.40) |
| *Scheduling and dosing for conditioning regimens were as follow s: | |
| • TBI/Cy 2 Gy TBI in 6 fractions bid days -6, -5, -4; Cyclophosphamide 60mg/kg/day days -3, -2 | |
| • Bu/Cy Busulfan 0.8 mg/kg for 16 doses days -7, -6, -5, -4, -3; Cyclophosphamide 60 mg/kg/day days -3, -2 | |
| • Bu/Flu Fludarabine 40 mg/m ² days -5, -4, -3, -2; Busulfan 130 mg/m ² days -4, -3, -2 | |
| • Flu/Mel Fludarabine 30 mg/m ² days -6, -5, -4, -3; Melphalan 140 mg/m ² day -2 | |
| • BEAM Carmustine 300 mg/m ² day -7; ara-C 100 mg/m ² for 8 doses days -6, -5, -4, -3; Etoposide 100mg/m ² for 8 doses days -6, -5, -4, -3; Melphalan 140 mg/m ² day -2 | |
| • Melphalan 200mg/m ² day -2 | |

Patients have had a median follow up of 11 months (range: 0.27–15.7) following SCT. Of the patients that underwent allogeneic SCT, 9 (69%) developed either acute or chronic GVHD. Median onset of acute GVHD (n = 7, 6 MUD recipients) and chronic GVHD (n = 4, all MUD recipients) were at 58 and 126 days post-transplant, respectively. The incidence of grade 3–4 acute GVHD was 15% and the incidence of moderate to severe chronic GVHD was 23%. Relapse occurred in one MUD recipient and CMV/EBV reactivation developed in nine and five (6/3, 4/1 MUD/MRD) patients, respectively. Seven of eleven MUD recipients are surviving, as are all MRD and autologous SCT recipients. Post-transplant, two patients diagnosed with GVHD later died; after

suffering multiple infections, one patient that remained GVHD-free died.

Cell Mass Measurements

Donor samples were obtained for mass measurement from apheresis products, with a 2 mL aliquot provided for each patient. Transplant recipient whole-blood samples (3 mL) were drawn at 14 ± 3 , 28 ± 3 , 56 ± 3 , and 100 ± 3 days post-transplant. After acquisition, whole-blood samples were stored at $+4^\circ\text{C}$ for no longer than four hours prior to cell isolation. CD3 + T cells were isolated directly from donor products and patient whole blood samples using the Dynabeads FlowComp Human CD3 Kit (ThermoFisher). Isolated cells were resuspended in 500 μL sterile phosphate-buffered saline.



For mass imaging, isolated CD3 + cells were transferred to optical glass-bottomed cell culture dishes to a maximum concentration of 1×10^6 cells per mL in a 3 mL volume of sterile PBS (Figure 15-A).

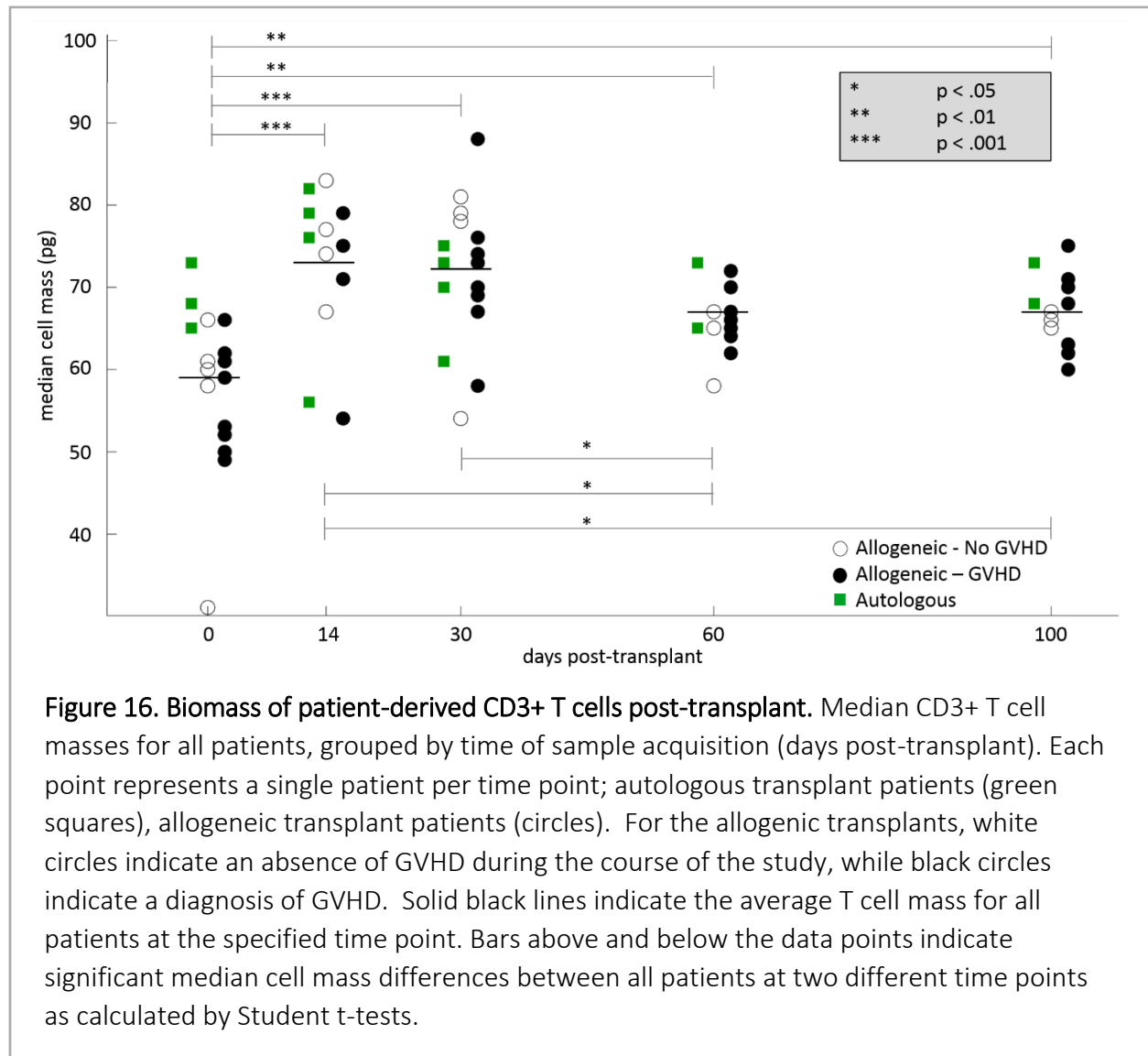
Measurements were taken using a 40X objective (Nikon, NA 0.75) under standard cell culture conditions (37 °C, 5% CO₂). The mass of each cell was calculated by taking the median of 20 individual mass measurements. **Figure 15-B** shows a representative histogram of single T cell masses found in a patient. The mass distribution was roughly symmetrical, with most median masses between 60–80 pg, and intra-patient variation of roughly 30 pg. **Figure 15-C** shows a typical field of view rendered as a 3D image, with height corresponding to local mass density or ‘optical thickness’. Individual cells appeared as extended spheres of varying density, therefore cellular diameter alone was not a good predictor of overall mass.

4.3 Results

T cell mass population medians for each sample are presented in **Figure 16** as a function of time post-transplant. We found a pronounced rise in median T cell biomass vs. infused product (median +25%; $p < 0.001$; Student's t-test) shortly after transplant (day 14), which moderated by day 60. Further, the inter-patient and intra-patient cell masses were most variable at days 14 and 30 post-transplant in both allogeneic and autologous SCT recipients (data not shown), when the ddCD3 count was the lowest. This is certainly consistent with the notion of a larger proportion of T cells post allograft being activated due to the inflammatory milieu resulting from conditioning related tissue/endothelial injury, infections and, in allogeneic transplant recipients, GVHD developing post-transplant.^{138,139}

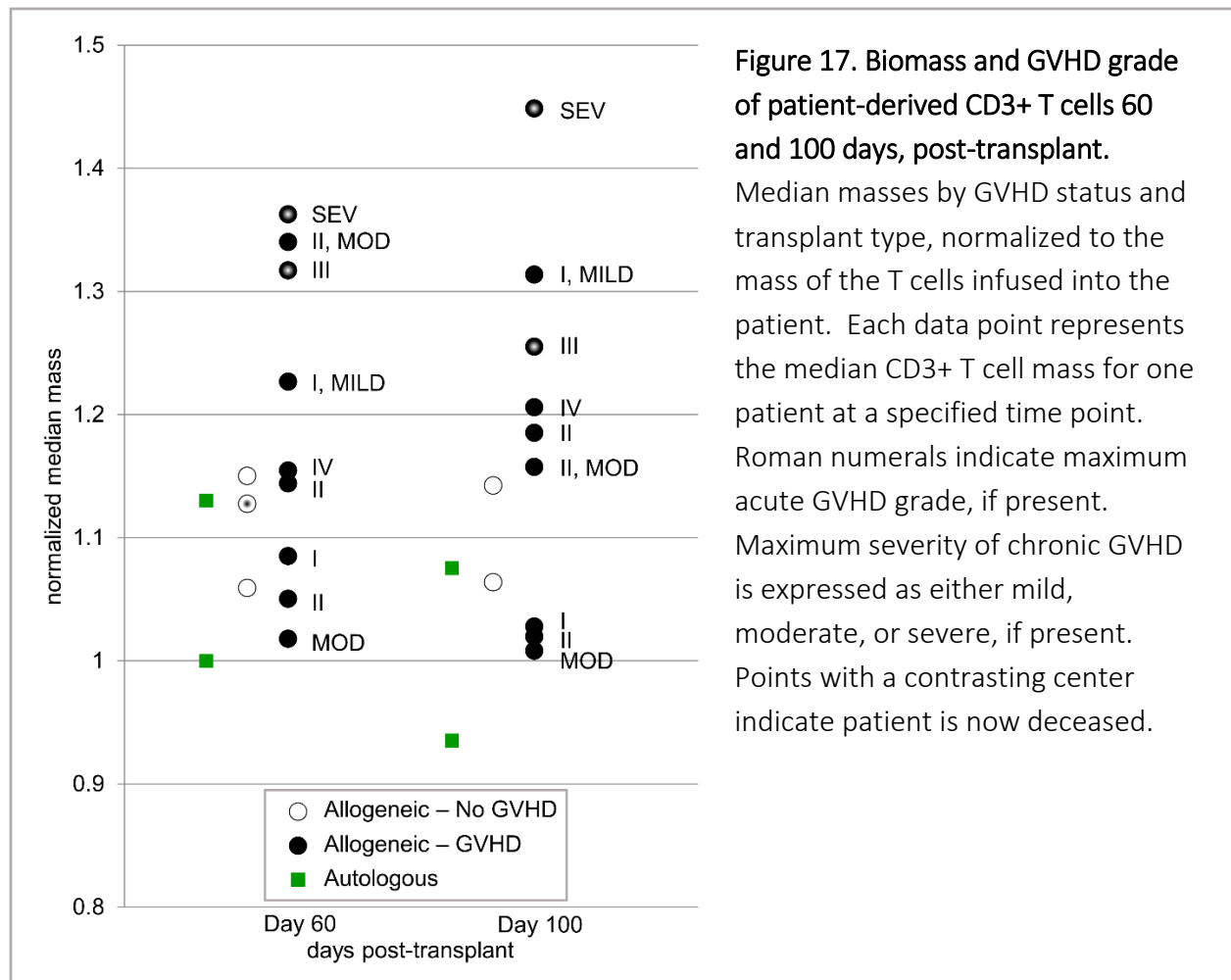
Our group has previously reported that lymphocyte count and CD3 + cell recovery post-transplant occurs as a logistic function of time, with exponential expansion occurring in the first few weeks following transplantation.¹³³ The observation that T cell mass is high at these early

time points is consistent with the notion that higher mass may be observed in proliferating T cells. The initial peak and then later plateau effect seen in our T cell mass observations is also reflected in T cell growth kinetics recorded following viral infections, which again has to do with antigen-driven



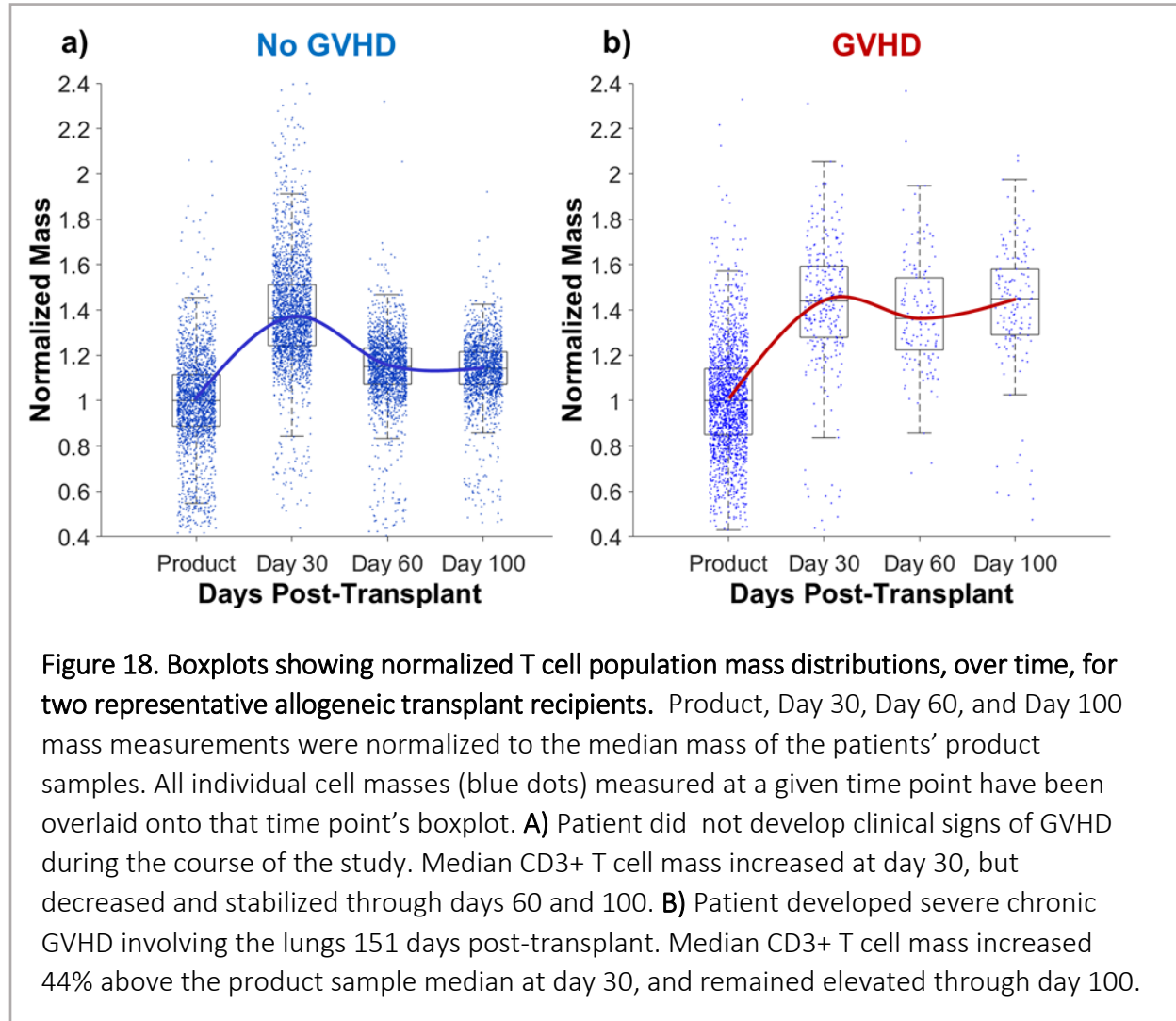
proliferation.¹⁴⁰ An alternative interpretation is that this high T cell mass in the first days reflects the effect of a 'cytokine storm' following SCT.¹⁴¹ Further, the lympho-depleted milieu of the early

post-transplant period may also contribute to the rapid growth of T cells and mass acquisition. In future studies, as T cell mass is measured, markers of proliferation will have to be assessed simultaneously to discern the effect of proliferation vs. T cell activation. Patients who developed GVHD tended to have persistently elevated or increasing masses at days 60 and 100 compared with their infused product T cell mass. Patients with GVHD exhibited a



significant ($p = 0.006$; Student's t-test) difference between product and day 100 normalized median masses, showing a persistent elevation (~18% higher median T cell masses than infused stem cell product) beyond day 30. Five patients exhibited a 20% or greater increase in median T cell mass at day 60 or 100, two of whom developed grade III–IV acute GVHD and one, severe

chronic GVHD (Figure 17). A representative example of one of these five patients is contrasted with a patient who did not develop GVHD, in Figure 18.



Finally, one of our patients, a 24-year-old male with Hodgkin's Lymphoma, suffered Grade III aGVHD and exhibited normalized median T cell masses of 32% (day 60) and 25% (day 100) greater than the infused stem cell product. The initial cell mass increase was coincident with Epstein Barr virus and Cytomegalovirus reactivation. Another, a 65-year-old male with Myelodysplastic Syndrome, was diagnosed with severe cGVHD and exhibited median T cell

masses 36% and 45% greater than infused stem cell product cells at days 60 and 100, respectively. Both patients later died.

4.4 Discussion

If this observation is validated in a larger cohort, T cell biomass could become invaluable as an inexpensive biomarker of alloreactivity and GVHD risk, and be used to guide decision making about intensity of immunosuppression post-transplant. This may also be a useful adjunct to PCR-based diagnosis of viral reactivation, where low level reactivation often raises the conundrum of whether toxic therapy should be initiated or held off on. Patients with high mass T cells in these instances may indeed be in the process of mounting a protective response and may be followed without introduction of cytotoxic drug therapy. Increasing the post-transplant sampling frequency would also be beneficial in order to account for the variability in onset of GVHD symptoms and better mitigate the effects of infections, viral reactivation, and relapse on T cell mass. Importantly, continued development of GVHD predictive models using T cell mass-based methodology must account for such potential confounding effects on this measure. However, contextualizing T cell mass measurements with conventional clinical manifestation of infections and GVHD, as well as with biomarkers, may allow real time titration of immunosuppressive therapy.¹⁴²

In order to simultaneously develop a more precise view of post-transplant alloreactivity and elucidate underlying immunobiological mechanisms, it will be necessary to go beyond CD3 + cell isolation and characterize relevant T cell subsets within each sample. Based on prior work by Meier et al. and Berrie et al. that highlight normal reconstituting T cell diversity and identify the

emergence of a limited number of dominant T cell clones in patients with GVHD, simultaneously assessing T cell clonality and mass during immune reconstitution could enhance the specificity of any predictive signatures.¹⁴³⁻¹⁴⁶ Cell mass spectra might also complement other modalities, including newly vetted biomarker panels for NRM and GVHD, such as those developed by Hartwell et al., as well as donor-derived T cell counts, lymphocyte reconstitution kinetics, and predictive modeling of minor histocompatibility antigens.¹⁴⁷ Our findings underscore the notion that alloreactive T cell response is a multifaceted reaction of the donor T cells to the recipient milieu. Aside from proliferation and T cell subset differentiation, there are critical metabolic and functional changes associated with antigen recognition, which may result in biomass change.¹⁴⁸ T cell subsets are of crucial importance to GVHD pathophysiology, therefore, measurement of T cell (and T cell subset) mass is a simple, clinically applicable parameter that summarizes the latter two adaptations of T cells to the change in the 'antigenic landscape'.¹⁴⁹ Despite a small patient cohort, results from this study provide the foundation for the continued assessment of T cell population mass in understanding and predicting metabolic changes in the T cells associated with alloreactivity and, subsequently, providing guidance for immunosuppression titration in allogeneic SCT recipients.

The cell mass measurement method we use is one of many available options, each of which has strengths and weaknesses depending on the application. The technical performance of the phase sensing camera employed has been well documented by the manufacturer in a series of papers.^{26,79,80} Our results suggest that other quantitative phase microscopy modalities, in particular digital holography, could be employed for this application with success.^{150,151} Our LCI system was automated for ease of use and reproducibility, but would not be considered high-

throughput. Improving the throughput and robustness of quantitative imaging platforms is an important direction of research for the field.

Chapter 5

Applications in Basic Research

5.0 Chapter Overview

This chapter details experiments investigating apoptosis in established cancer cell lines, the kinetics of degranulation in mast cell populations, and cell growth patterns in genetically engineered Kaposi's sarcoma cells during the latent-lytic switch of an oncogenic virus.

5.1 Apoptosis Assays

5.1.1 Introduction

As previously discussed, LCI's utility hinges on the ability to correlate biological events of interest with changes in the mass of the cells being observed. Experiments designed to validate these correlations are typically conducted using LCI *in parallel* with established analytical methods. Considering our initial goal of assessing the response of cancer cell lines to cytotoxic drugs, the ability to quantify cell death in terms of changes in mass was an important early milestone.

Cell death can occur as a result of internal processes like cell aging or external factors like acute injury or disease and, further, can proceed via several mechanisms.¹⁵² Injury and disease typically cause cells to die by necrosis, while certain drugs, immune cell killing, cell aging, and mitotic errors result in programmed cell death via apoptosis or autophagy.^{153–155}

Of the cell death mechanisms, apoptosis is particularly dramatic owing to its irreversible nature and array of associated morphological changes.¹⁵⁶ Commercially-available kits can detect different stages of apoptosis using cytotoxic chemicals and fluorescent dyes, allowing researchers to understand the impact of specific conditions or drugs on a given cell.¹⁵⁷ By coupling LCI and fluorescent imaging, we hypothesized that the induction of apoptosis and

subsequent cell destruction would result in significant decreases in mass that correlated with appropriate fluorescent dye signals. Based on this hypothesis, we designed an experiment to evaluate the correlation between mass loss and fluorescently-indicated apoptosis in established lung (A549), kidney (786-0), and breast (MCF7) cancer cell lines.

Briefly, cells would be exposed to the apoptosis-inducing agents Actinomycin D and Camptothecin in the presence of the fluorescent dyes YoPro1 (YP1) and Propidium Iodide (PI).¹⁵⁸ YoPro1 is a DNA-intercalating dye that fluoresces green; PI is a DNA-intercalating dye that fluoresces red.^{159,160} Both dyes enter cells through plasma membranes whose structures have been compromised due. Because apoptosis triggers morphological changes that compromise a cell's plasma membrane, these dyes can enter and bind to DNA. Importantly, as the smaller of the two dyes, YP1 is capable of entering dying cells earlier than PI. Taken together, we would expect that cells exposed to Actinomycin D and Camptothecin, in the presence of YP1 and PI, would simultaneously exhibit a detectable loss of mass while first fluorescing green and then red.

5.1.2 Results & Discussion

Control groups in each of the three lines exhibited steady single-cell growth rates of 2%/hr (MCF-7), 2%/hr (786-0), and 3%/hr (A549). As expected of cultured populations, ~5% of cells in each control group were non-viable as evidenced by detectable YP1 and PI fluorescence.

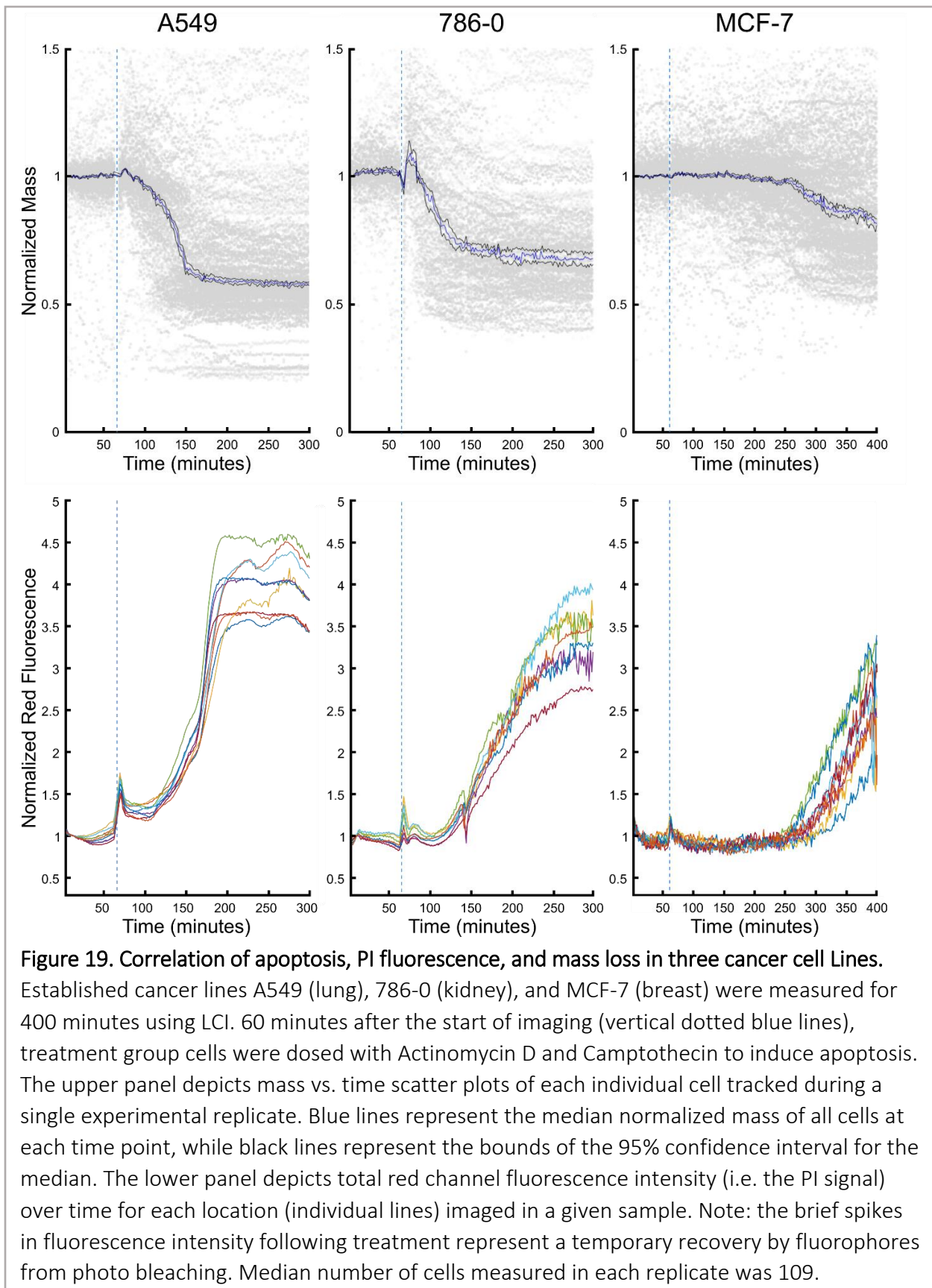
Treatment groups for each line exhibited pre-dosing growth rates similar to controls. After dosing, median mass lost per cell ranged from 10-60%. Line A549 responded both more robustly and more quickly than the other two lines, with PI fluorescence visible in almost all cells within 140 minutes of treatment and median mass loss per cell of approximately 40%. In line 786-0, PI

fluorescence was similarly visible for all cells by 200 minutes, post-treatment, with a median mass loss of 30%. Finally, line MCF-7 exhibited the slowest response, with PI fluorescence visible in all cells at approximately 450 minutes after dosing. Results are summarized in **Figure 19**.

Data show a correlation between the timing of drug-induced apoptotic mass loss and PI fluorescence in all three lines measured. However, variation between the extent and the timing of mass loss between cell lines was apparent. Interestingly, the longer the published doubling time for each cell line, the longer the amount of time required to induce mass loss and fluorescence. While the underlying mechanism behind this observed disparity in timing is unclear, our results demonstrate a clear link between the timing of cell mass loss and the fluorescence of established markers following exposure to inducers of apoptosis.

5.1.3 Methods

For each experimental replicate, cells were seeded at 5×10^4 cells/ml in a 25 cm² diameter optical-glass-bottomed dish and allowed to grow for 24 hours in appropriately-supplemented RPMI 1640 or DMEM-based media under standard mammalian cell culture conditions (5% CO₂, 37 °C). Media was exchanged 24 hours after plating. After the media exchange, the dish was placed on the sample stage in the LCI system for one hour to reach thermal equilibrium. YP1 and PI were added to the dish to final concentrations of 1 μM and 1μg/mL, respectively. After dosing, brightfield, fluorescence, and phase images were collected for one hour, at 10X magnification, in a 3x3 grid pattern to measure baseline growth rates. After one hour, 1X concentrations of Actinomycin D and Camptothecin were administered, and imaging proceeded for an additional 800 minutes.



For each cell line, one control (media vehicle) and three treatment replicates were performed. To ensure consistency and enable troubleshooting, the temperature and CO₂ concentration in the incubator (as well as the Z focus position of the objective) were logged during each experiment. These measurements are critical because fluctuations in any of the three metrics can alter the mass measured by the LCI, either by actually impacting the biological health of a cell, or producing out-of-focus images that result in artificially high or low measurements.

5.2 Mast Cell Biology

5.2.1 Introduction

Mast cells are multifaceted components of the immune system best known for their role in mediating allergic responses.^{161,162} They are found in almost all tissues of the body, including the skin, gastrointestinal tract, respiratory mucosa, brain, and peritoneal cavity.¹⁶³ Capable of responding rapidly to stimuli, mast cells contain an array of effector molecules (mediators), including histamine, serotonin, and multiple cytokines.^{164–166} The majority of these mediators are packaged into granules and, upon a cell receiving a sufficient signal to “degranulate,” are released.¹⁶⁷ Effects of mediator release are numerous, including changes in the permeability of blood vessels and the recruitment of immune cells.¹⁶¹ In addition to their role in normal physiological responses, mast cells are implicated in wide range of conditions and diseases, including cancer, cardiovascular disease, obesity, and autoimmune diseases.^{168–172}

Degranulation is the process by which mast cells release their array of preformed mediators. The process can be initiated through a variety of pathways, though the most common is IgE-mediated.^{173–175} Briefly, mast cells express FcεRI, a high-affinity receptor for IgE, on their

surfaces. IgE binds to FcεRI receptors and, when bound by its specific antigen, results in the crosslinking of multiple FcεRI receptors. This crosslinking triggers a signal cascade that ultimately results in the release of intracellular calcium and, subsequently, degranulation.¹⁷⁶ Once degranulation has been initiated, granules move to the mast cell's membrane, fuse, and release their contents. This entire process occurs in minutes and is accompanied by striking morphological changes.¹⁷⁷⁻¹⁷⁹

As degranulation plays a central role in mast cell activity, studying its biological underpinnings enables both a better understanding of mast cells' roles in disease and our ability to develop new therapeutic interventions.¹⁸⁰ Of particular relevance are characterizing the quantities of mediators released and the recovery period required between successive triggering events.¹⁸¹⁻¹⁸³ Literature on the latter is sparse, with one study suggesting an approximately 48-hour recovery period in murine bone marrow-derived mast cells.¹⁷⁹ Research laboratories commonly measure degranulation by fluorescently tagging released effector molecules like histamine, prostaglandin D₂, beta-hexosaminidase, or IL-6 and then quantifying fluorescent signals.¹⁸⁴ This is a useful "endpoint assay" approach, but it precludes labeled cells from being used in downstream experiments and requires bulk averaging of signals from cells in a population. Our goal, in close collaboration with Dr. John Ryan's laboratory in the VCU Department of Biology, was to evaluate LCI and HSLCI as label-free tools for studying mast cell biology. In the process, we hoped to gain insight into how much mass was lost by mast cells undergoing degranulation in response to various stimuli and how long it takes for them to recover from this process.

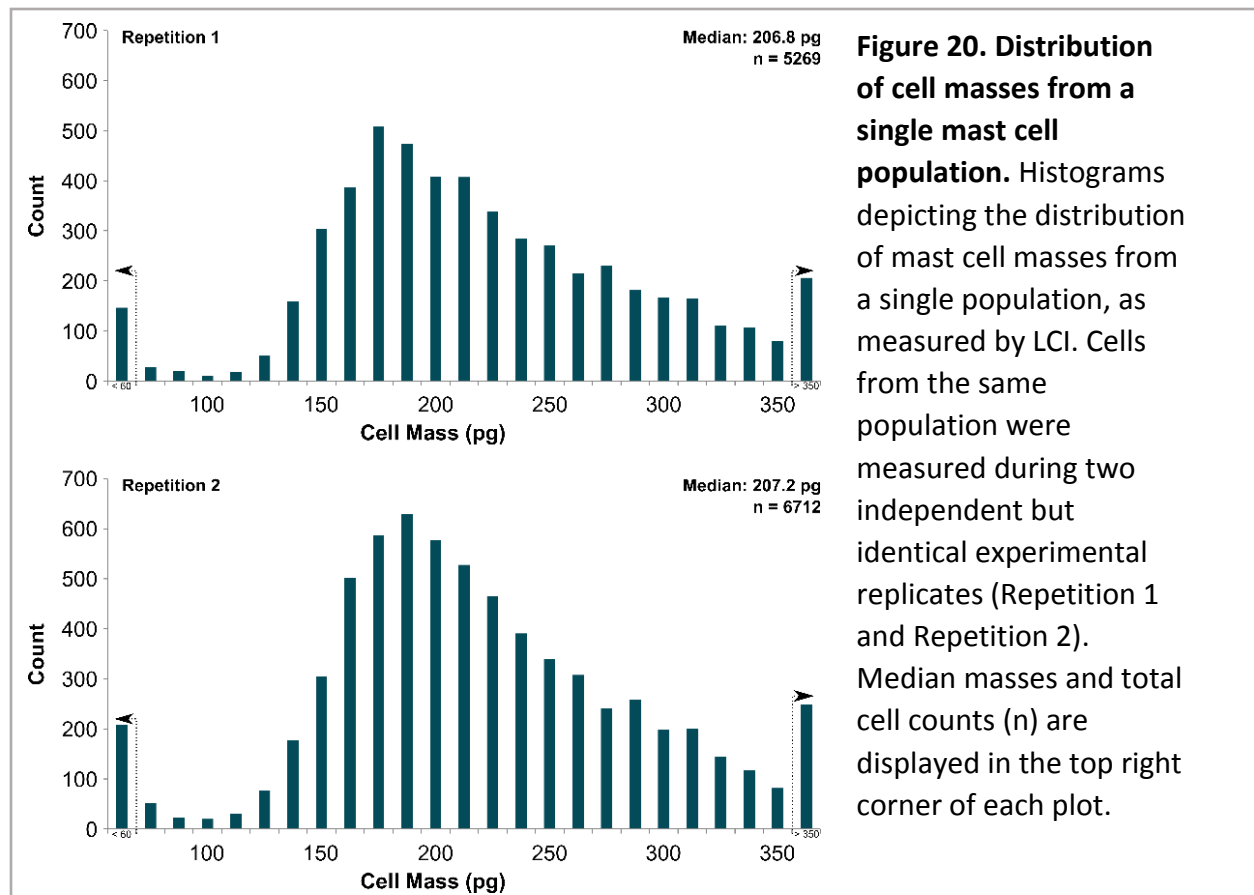
5.2.2 Approach

Our approach centered around a robust characterization of mast cell population mass, size, and behavior. A series of population-level and single-cell experiments were conducted. Briefly, investigations of cell mass distributions and measurement reproducibility involved imaging thousands of mast cells from distinct populations to examine intra- and inter-batch variation, as well as differences between unprimed, primed, and triggered cells. Degranulation assays focused on measuring mast cell masses before, during, and after the administration of known triggering agents to examine response kinetics and recovery time. These assays were also conducted using established fluorescent markers to correlate mass loss events with cell membrane disruptions associated with degranulation. Two triggering agents were used: Ionomycin, a calcium ionophore, and DNP-HSA, a biologically-relevant antigen.

5.2.3 Results

Cell Mass Distribution and Variation

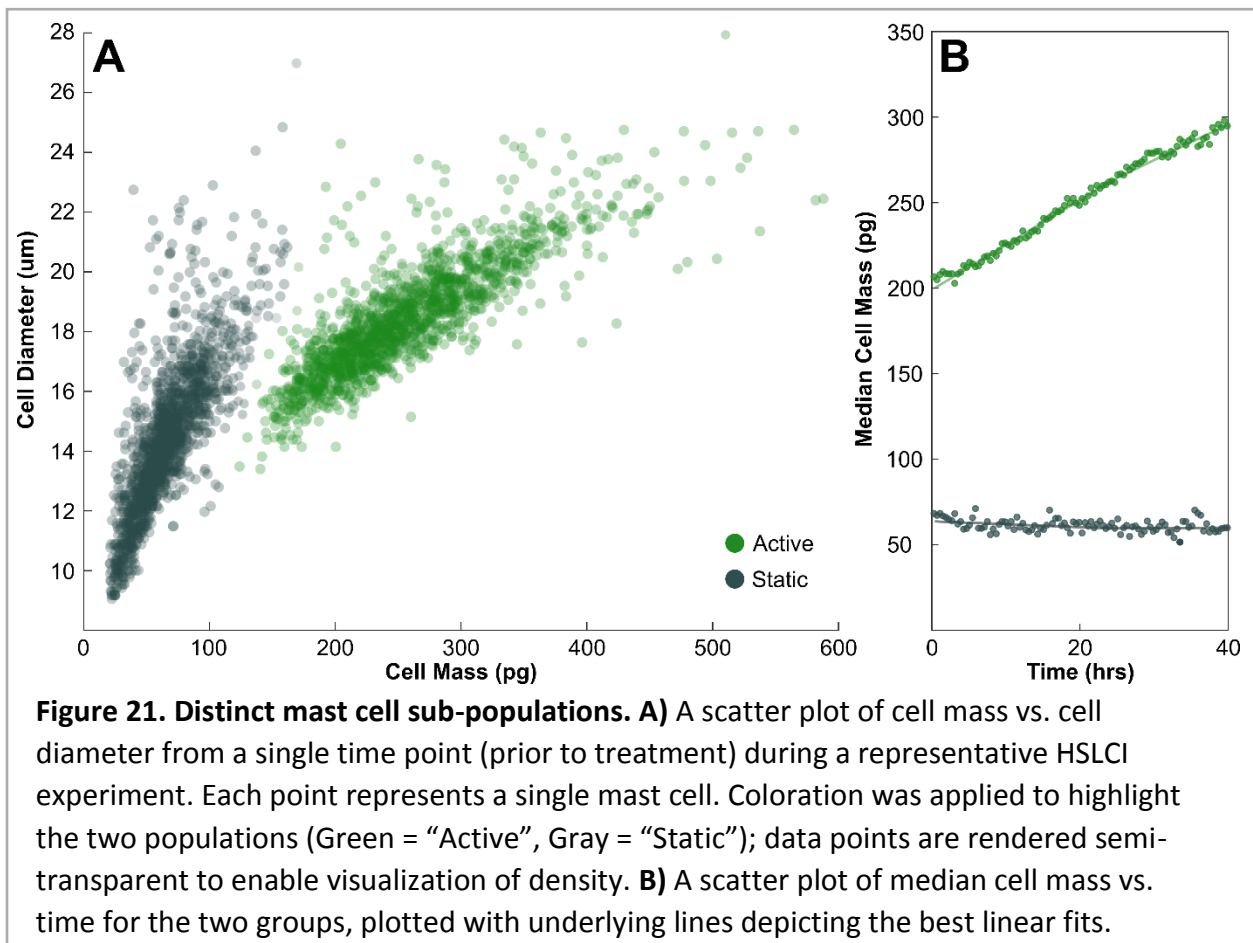
Taken together, population-level studies revealed a consistently positively skewed distribution of masses within a given mast cell population. Median masses ranged from 150-350 pg. The distribution of cell masses in a representative population is shown in **Figure 20**. Variation in pre-treatment median masses between different cell batches was observed, with the largest median masses measuring 2X larger than the lowest recorded medians. Experiments comparing the masses of primed vs. unprimed cells from the same batch of cells revealed median masses in primed cell populations to be 4-9% larger than unprimed populations.



HSLCI Degranulation and Recovery Assays

HSLCI degranulation and recovery assays revealed the presence of two distinct groups of cells based on cell size and mass (**Figure 21**). These groups were present in all samples and all treatment groups. Interestingly, the smaller of the two groups remained essentially static throughout the course of each experiment, neither gaining or losing mass or area. This group was termed “Static.” The larger of the two, termed “Active,” exhibited growth in all experiments. Further, a re-analysis of data from experiments conducted on the original LCI system revealed the presence of these same two distinct populations of cells.

Examples of both successful and unsuccessful DNP-HSA triggering of cells in the Active groups are shown in **Figure 22-A**. An analysis of pre-treatment population median masses revealed that degranulation was only detected in the two most massive mast cell populations (**Figure 22-B**). In addition, in these responsive groups, a distinct pattern emerged in which treated cells rapidly lost mass in response to DNP-HSA, then rapidly increased in size (area). Their size quickly diminished to pre-treatment levels and the growth of the cells (in terms of mass and area) resumed (**Figure 23**).



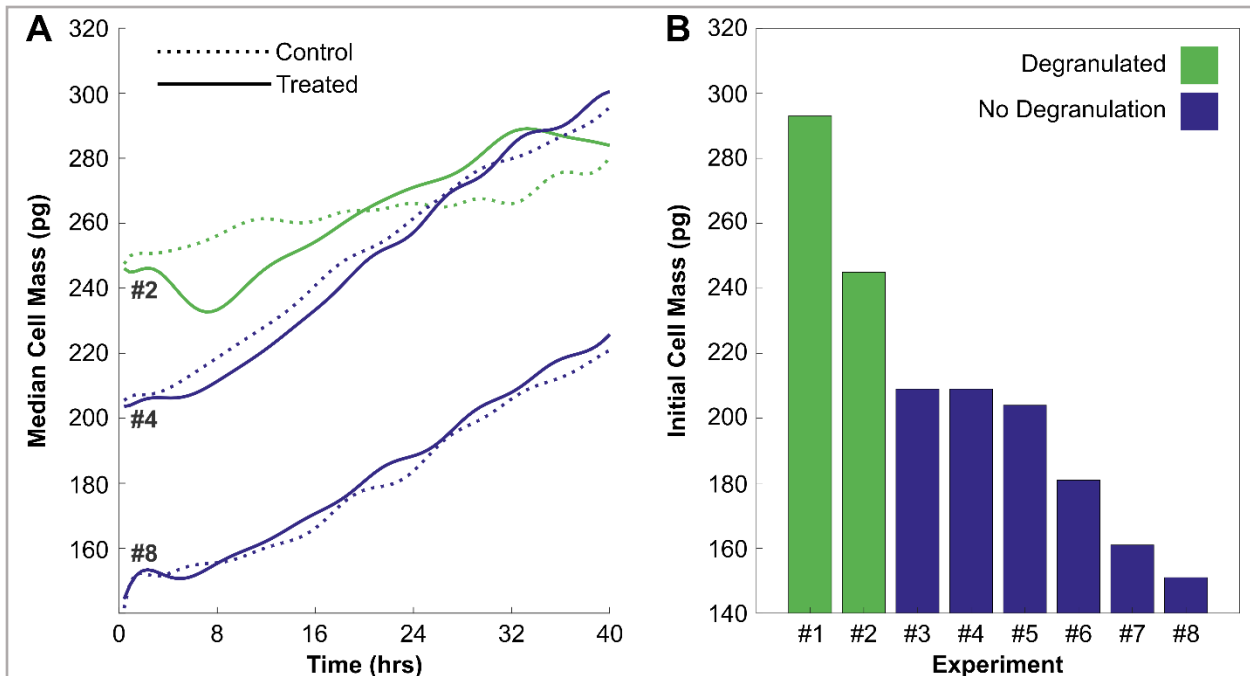


Figure 22. HSLCI-measured DNP-HSA response kinetics and inter-population mass variation. **A)** Plot of median Active cell mass vs. time for three different representative DNP-HSA response assay replicates, as measured by HSLCI. Dotted lines represent control groups, while solid lines represent groups treated with DNP-HSA. Green coloration indicates an experiment in which degranulation was successfully detected. Blue coloration indicates that no degranulation was detected. Numbers and coloration correspond to those shown in **B**. **B)** Bar plot of pre-treatment median masses from independent HSLCI experimental replicates. As stated previously, coloration indicates whether or not degranulation was measured in response to DNP-HSA treatment. Experiment number is arbitrary and not reflective of chronological order. Median number of cells measured for each experiment was 1422.

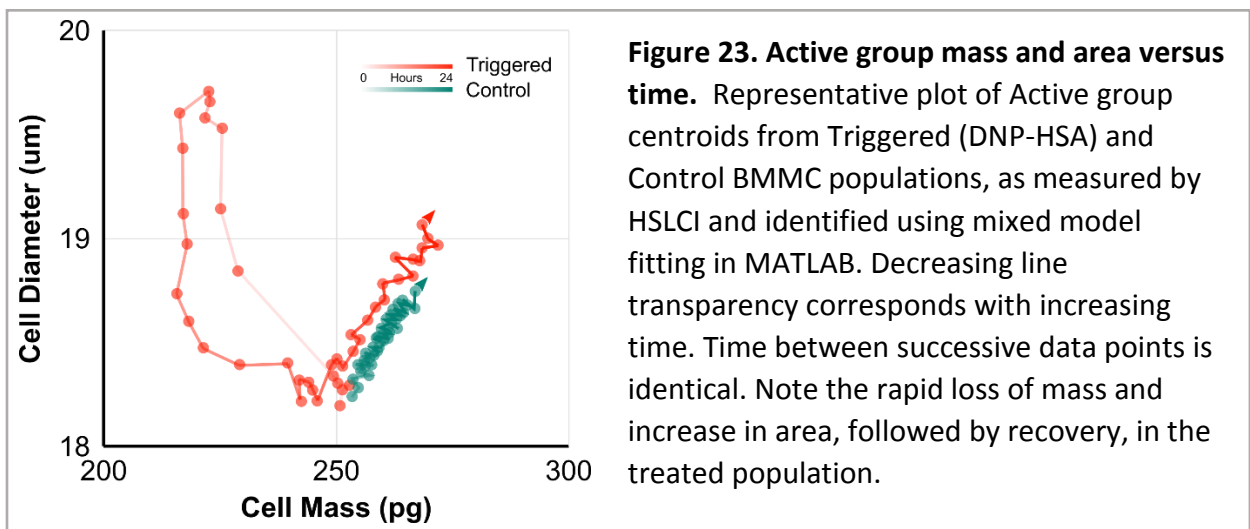
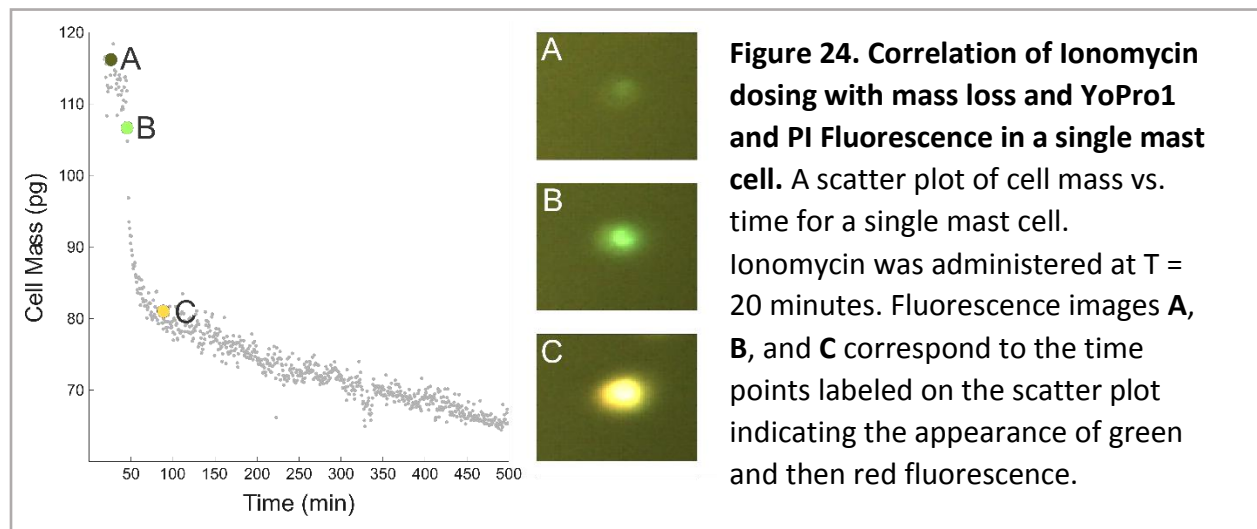


Figure 23. Active group mass and area versus time. Representative plot of Active group centroids from Triggered (DNP-HSA) and Control BMMC populations, as measured by HSLCI and identified using mixed model fitting in MATLAB. Decreasing line transparency corresponds with increasing time. Time between successive data points is identical. Note the rapid loss of mass and increase in area, followed by recovery, in the treated population.

Correlation of Degranulation with Mass Loss and Fluorescence

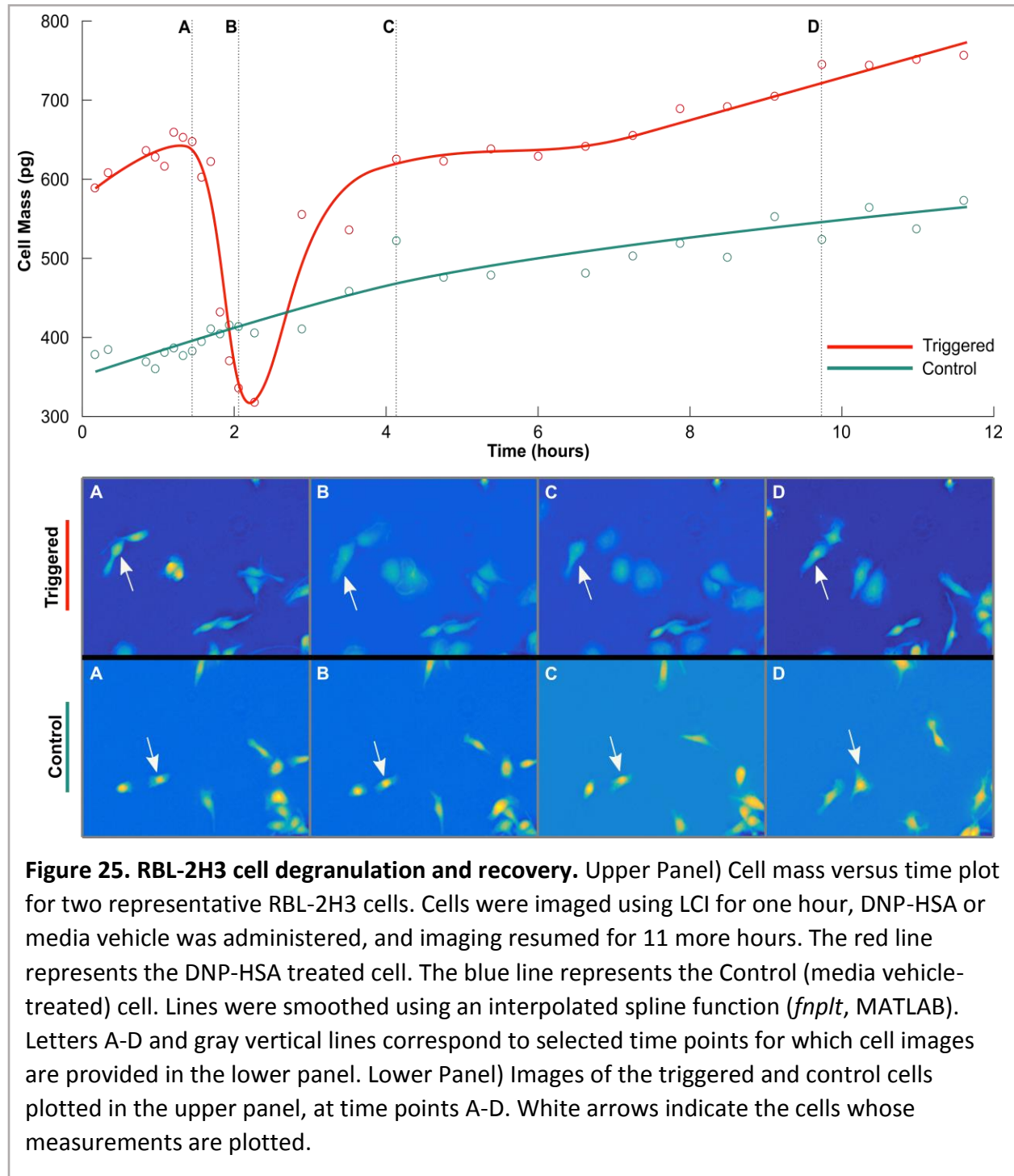
Methylcellulose was successfully employed in short-term fluorescence correlation experiments. Mass losses ranging from 20-50% were observed in hundreds of individual cells suspended in 1% methylcellulose following the administration of Ionomycin. The appearance of fluorescent signals from PI and YP1 correlated precisely with the decline of each cell's mass, with YP1 (the smaller of the two molecules) appearing several minutes prior to PI. A single-cell example is provided in **Figure 24**.



Characterization of RBL-2H3 Degranulation and Recovery

Tumor line RBL-2H3 control and pre-treatment cells exhibited growth rates ranging from 2-5% per hour. Cells treated with 1X DNP-HSA exhibited a rapid 30-50% decrease in mass within one hour of dosing, while control cells grew unabated (**Figure 25**). Interestingly, mass lost by treated cells was recovered within 1-3 hours, with cells continuing to grow steadily at 2-3% per hour for 18 more hours. In addition to their robust growth, many RBL-2H3 cells exhibited significant

motility during the experiment's 20-hour duration. This is consistent with behavior noted in other studies.¹⁸⁵



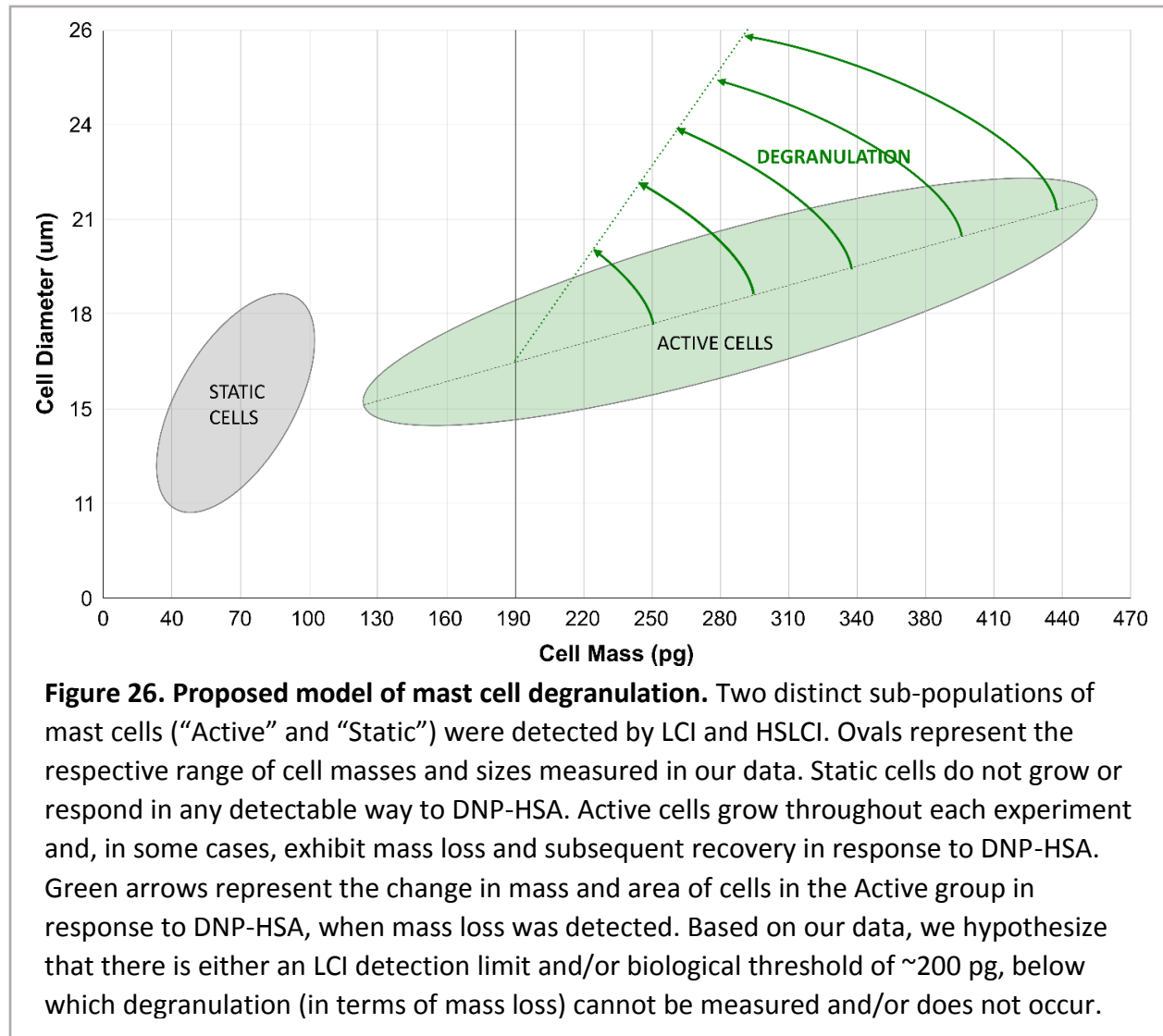
5.2.4 Discussion

Taken together, the data demonstrate LCI and HSLCI's ability to reliably detect and measure mast cell degranulation in the form of cellular mass loss, without the need for dyes or labels. At present, HSLCI is best suited for population-level studies in mast cells due to its speed and multi-sample capacity, while the system's single-cell tracking capabilities require refinement for this cell type due to their rapid drifting in culture vessels. In the course of coming to these conclusions, several important observations were made.

First, the presence of two distinct populations of cells was apparent in every experiment conducted. It is unclear what, other than their size and growth behavior, differentiate the two groups. Second, significant variation was seen in the median pre-treatment masses of Active groups from different batches of mast cells. While all mast cell populations tended to consistently exhibit a positively skewed distribution of cell masses, observed medians ranged from 150 pg to 350 pg. Priming mast cells with IgE does not seem to contribute significantly to this variation

Third, as previously mentioned, our HSLCI data indicate that mass loss due to DNP-HSA-triggered degranulation was only detectable when median pre-treatment masses were greater than 225 pg. The majority of cell populations measured across our experiments had median masses lower than this threshold. However, these same cell populations were successfully triggered using DNP-HSA (as measured by IL-6 ELISA), at a variety of cell densities, in the Ryan lab. It is possible that these response disparities might stem from a detection limit in our population-level approach to measuring mass loss (**Figure 26**). A second explanation is that there is a minimum

biological threshold for degranulation. Perhaps cell size and mass correlates with a measure of maturity (i.e. sufficient mediator content) and, therefore, cells that are not mature (i.e. too small, insufficient content) will not degranulate in response to FCεRI-mediated activation. This explanation would fit with our data, but would need to be borne out using additional assays for degranulation in light of the positive IL-6 ELISA.



Fourth, RBL-2H3 cells consistently exhibited a rapid recovery of mass (~90 minutes) following degranulation. Regardless of the cause, RBL-2H3 cells behave differently from murine BMMC-

derived mast cells. As the tumor line is a familiar presence in mast cell research laboratories, a more thorough understanding of its biology is warranted.

Mast cells play a multifaceted role of in allergy and disease. Providing a means by which to assess degranulation, in addition to understanding the mechanisms that underlie the process, is important for basic and translational research. These studies raise important questions about the way in which degranulation is measured, and the effect that population variations, natural or otherwise, affect the outcome of experiments.

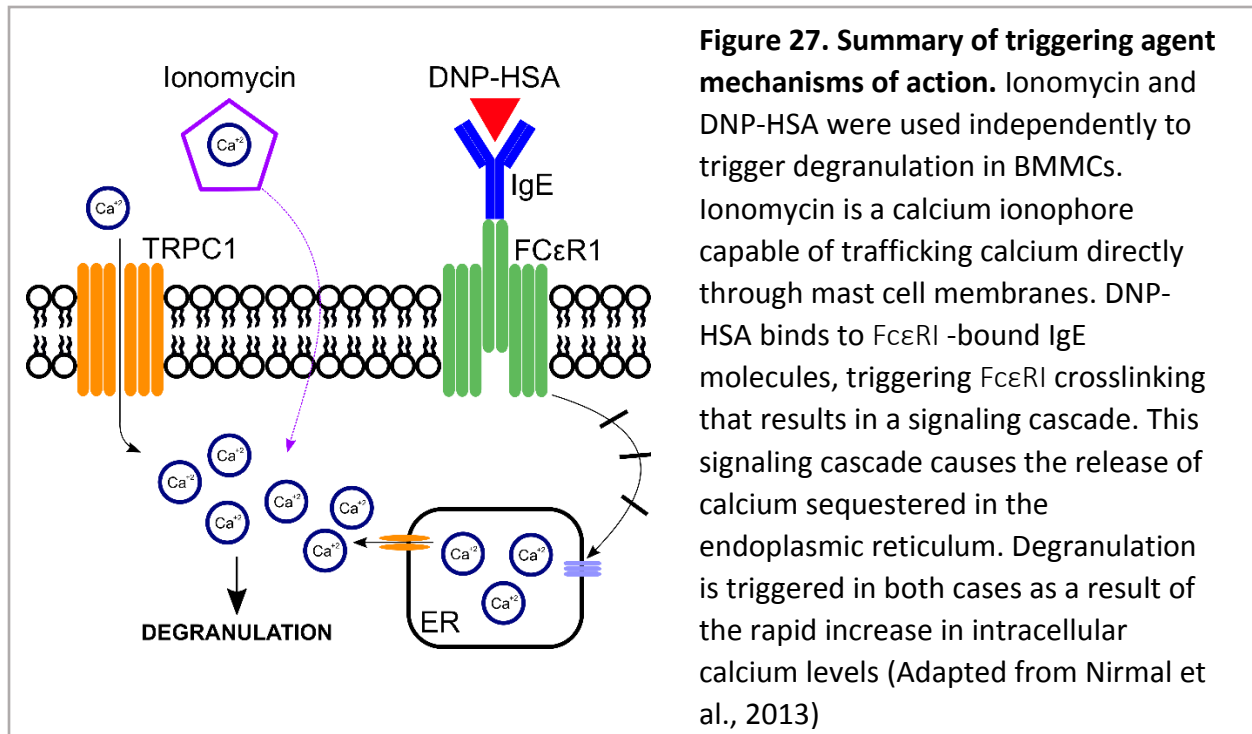
5.2.5 Methods

Mast cells

All mast cells were provided by and obtained from Dr. Ryan's laboratory at Virginia Commonwealth University. Unless otherwise noted, cells were derived by the Ryan lab using a Black 6 genetic background. Briefly, bone marrow cells are harvested from the femurs of the mice. These cells are cultured with Interleukin 3 (IL-3) and Stem cell factor (SCF) for four to six weeks, resulting in their differentiation into mast cells. These differentiated cells are subsequently viable for experiments for up to eight weeks when maintained with continuous supplementation of IL-3 and SCF in RPMI culture medium.

Triggering Agents

Cells triggered using DNP-HSA were first "primed" overnight using 100 ng/ml of mouse anti-DNP IgE. Media was exchanged and cells washed prior to experimentation and exposure to DNP-HSA. Cells triggered using Ionomycin did not require priming and, therefore, only a media



exchange was necessary prior to experimentation (**Figure 27**). Stocks of all triggering agents and media were prepared and provided by the Ryan lab.

Population-level Dose Response Studies using LCI

Initially, population-level investigations of mast cell degranulation utilized the first iteration of the LCI system. Mast cell responses to Ionomycin and DNP-HSA were assessed at multiple time intervals and across a range of doses. In our inaugural experiments, cells were imaged by the LCI in a custom, 4-well Teflon sample block. Briefly, two 20 mm x 20 mm hand-cut silicon squares were prepared from silicon wafers and cleaned with 70% ethanol. One silicon square was placed in the center of each of two wells, designated Control or Treatment, in the Teflon block. 3mL of cells suspended in culture medium (5×10^5 cells/ mL) was then added directly to each of the two wells. An optical imaging window was placed on top of each of the silicon chips.

Response kinetics were measured in response to a 1X (1 nM) dose of Ionomycin. Cells in the Treatment well were measured prior to dosing to establish a baseline distribution of population cell masses. Ionomycin was administered after these baseline mass measurements, followed by additional measurements every 5 minutes for 25 minutes. Imaging of the Control well was conducted similarly, with the administration of a media vehicle control (6 μ l) in place of Ionomycin. Three replicates of this experiment were conducted.

Follow-on experiments examined our ability to resolve responses across a wide range of Ionomycin doses. To accommodate an increased number of samples, cells were imaged on a modified Teflon sample block (**Figure 28-A**). Three standard glass microscope slides () were painted matte black and arrayed in parallel on the Teflon block's surface. 20 mm x 20 mm hand-cut squares were prepared from silicon wafers, cleaned with 70% ethanol, and arrayed in a 2x3 grid pattern. 0.25 mm thick plastic shims were placed on top of each silicon chip. Number X glass cover glass squares were then placed on top of each shim. The effective imaging area for each sample using this arrangement of components was approximately 200 mm². Mast cell responses to Ionomycin were assessed across a log scale of doses (**Figure 28-B**). Briefly, 1×10^6 unprimed mast cells were deposited on to each silicon chip and covered with cover glass. Pre-treatment mass measurements were collected from each dosing group's sample. Ionomycin was then added to all samples at indicated doses and allowed to take effect for five minutes. Four images at different locations within the sample well were taken for each dose condition. After

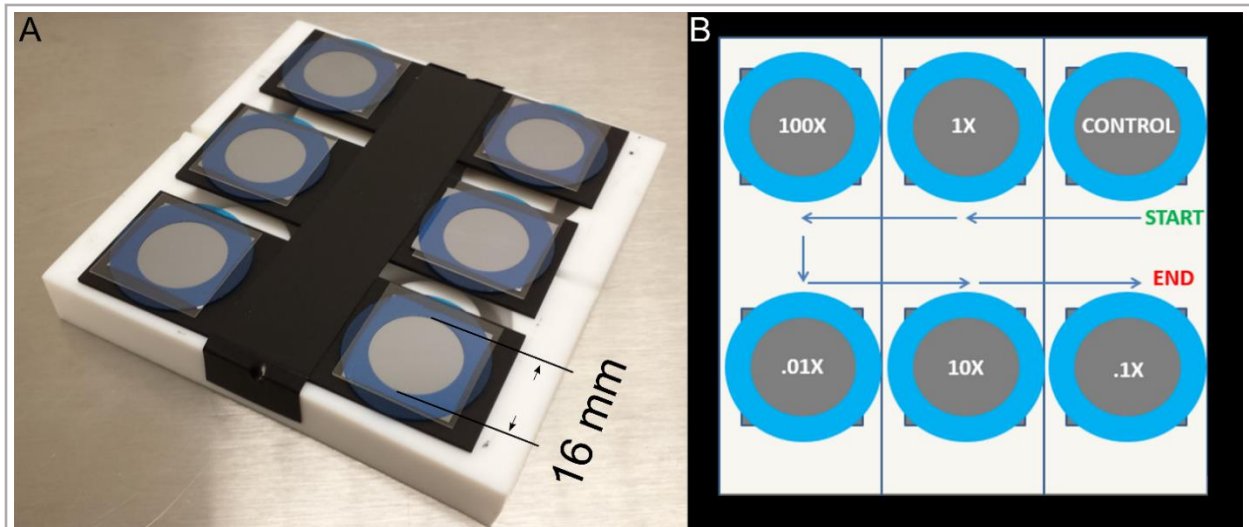


Figure 28. LCI sample mount and dosing overview. A) Three standard glass microscope slides were painted matte black and arrayed in parallel on the surface of the Teflon block's surface. 20 mm x 20 mm hand-cut squares were prepared from silicon wafers, cleaned with 70% ethanol, and arrayed in a 2x3 grid pattern. 0.25 mm thick plastic shims were placed on top of each silicon chip. Number X glass cover glass squares were then placed on top of each shim. The effective imaging area for each sample using this arrangement of components was approximately 200 mm². **B)** Schematic of the sample imaging order and dosing used in a single Ionomycin response assay replicate.

each dose group had been imaged, the imaging process was repeated for a second cycle. Replicates of this experiment were performed three times. The order of imaging for dosing groups was randomized for each replicate. These time interval and log-scale dose response experiments were repeated, each in triplicate, with DNP-HSA (1X = 50 ng/mL) as a triggering agent instead of Ionomycin.

Effects of IgE Priming on Mast Cell Mass

Investigations of Primed vs. Unprimed mast cells consisted of comparing cells from the same initial population of mast cells. A group of viable cells was split and one half primed (as previously described). The next day, cells from both groups were deposited and imaged on the

modified, six-sample Teflon block (approximately 1500 cells measured per group). This was repeated three times, with each replicate occurring on a different day.

Validation of LCI Measurement Reproducibility

Reproducibility validation experiments utilized fresh unprimed mast cells. 2 mL of 5×10^5 cells/mL cell suspension was pipetted on to each of six silicon chips on the modified Teflon block and covered with cover glass, as previously described. Four images were collected of each chip. Immediately following this first imaging cycle, a second identical cycle was performed. This experiment was performed in triplicate using different populations (different isolation days) of mast cells.

Measurement reproducibility was further assessed by imaging fresh untreated cells on a single silicon chip. 2 mL of 5×10^5 cells were deposited onto the chip and covered with cover glass, as previously described. 25 images (5x5 grid pattern) were collected. After this first cycle, an additional five imaging cycles were performed on the same sample. Three replicates of this experiment were conducted, each using a different population of mast cells.

Single-Cell Degranulation Studies Using LCI

Experiments involving single-cell tracking utilized 35 mm, single-well, glass-bottomed dishes, unless otherwise noted. A custom double-dish mount was constructed to enable the simultaneous use of up to two of these dishes (i.e. Control and Treatment). Additionally, all mast cell experiments described from this point forward utilized a Phasics camera to acquire mass measurements (as opposed to the modified Michelson interferometer described previously).

Proof-of-concept cell immobilization studies were conducted using 2.5 ml of fresh untreated mast cells suspended to a final concentration of 5×10^5 cells/mL in a 1% methylcellulose solution prepared using complete RPMI culture medium. A 4x4 grid of images was collected by the LCI every 10 minutes for 16 hours. Phase images were processed as previously described to generate mass measurements for individual mast cells.

Fluorescent imaging studies (summary provided in **Supplementary Table 3**) designed to correlate mass loss events with degranulation were performed as follows. 2.5 mL of fresh untreated mast cells were aliquoted and 1X concentrations of YoPro1 (YP1) and Propidium Iodide (PI) were added. A 1% methylcellulose solution was prepared using complete RPMI culture medium. Dyed cells were suspended in the solution to a final concentration of 5×10^5 cells / ml. This cell suspension was transferred to a single 35 mm glass-bottomed dish and incubated under standard cell culture conditions for one hour. After incubation, the dish was transferred to the LCI. Image collection was initiated in a 2 x 2 grid, with brightfield, fluorescent, and phase images being collected in rapid succession at each location. Ionomycin was administered to the sample at 1X after approximately 20 minutes of imaging. Post-dosing, imaging continued for eight hours. Three replicates of this experiment were performed. Variations of this experiment were also conducted using DNP-HSA instead of Ionomycin.

Phase images from these fluorescent imaging studies were processed as previously described to generate mass measurements for individual mast cells. Fluorescent images were separated into individual RGB channels, with each channel being subsequently analyzed to track intensity over time for regions of interest identified by MATLAB's *otsu* thresholding function.

Experiments with the adherent rat basophilic leukemia cell line RBL-2H3 were performed as follows. RBL-2H3 cells were obtained from the Ryan lab and immediately deposited in provided culture medium to a final concentration of 2×10^5 cells/mL in two glass-bottomed dishes. Dishes were placed in a cell culture incubator overnight to allow time for cell adherence to the dish surface. After incubation, dishes were transferred to the LCI system and allowed to reach thermal equilibrium for one hour. After one hour, 4x4 grids of images were collected from each dish every 15 minutes for one hour, at which point one of the dishes received a 1X dose of DNP-HSA. After dosing, cells were imaged for an additional 36 hours. This experiment was repeated twice.

Measurement of Degranulation and Recovery

Experiments investigating the population-level mass kinetics of degranulation in response to DNP-HSA were conducted as follows. Mast cells were primed overnight with IgE (as previously described) by the Ryan lab. 3mL of primed cells in culture medium were deposited into each well of a 24-well plate at a final concentration of 5×10^5 cells/mL. The plate was placed in the HSLCI and allowed to reach thermal equilibrium for one hour. Imaging was conducted at a rate of 30 images/well every eight minutes for one hour, with plate tilting every 10 minutes. After one hour, half of the wells in the plate were dosed with 1X (50ng/mL) DNP-HSA. After dosing, imaging continued for an additional 39 hours. Replicates of this experiment were performed seven times with moderate variations, including the simultaneous measurement of different batches of primed cells or the inclusion of an unprimed population from which primed cells were generated. Data generated by the experiments were filtered using manually-implemented cutoffs for cell mass and area to remove spurious data points.

5.3 Kinetics of KSHV Lytic Activation

Kaposi's sarcoma (KS) is an incurable cancer associated with immunosuppression or immunodeficiency, often occurring in patients with AIDS or those who have undergone organ transplantation.¹⁸⁶ It typically effects the skin, but can occur in the lymph nodes, gastrointestinal tract, and major organs.¹⁸⁷ The primary cause of KS is infection with human herpesvirus-8 (HHV-8), also known as Kaposi's sarcoma-associated herpesvirus (KSHV), which is commonly transmitted via saliva.¹⁸⁸ Briefly, after infecting host cells, KSHV's latency program is activated by default, resulting in the production of several important proteins that interfere with host p53 and retinoblastoma protein activity, ultimately compromising the cells' genetic integrity.^{189,190} Certain signals can also activate the virus' lytic program, during which it makes thousands of infectious copies of itself and eventually destroys the host cell.¹⁹¹⁻¹⁹³ KSHV is a particularly interesting because of its possession of numerous human genes, its strong association with multiple cancers, and its shared membership in the same viral family as Epstein-Barr virus.¹⁹⁴

In collaboration with the Dr. Blossom Damania's laboratory at the University of North Carolina's Lineberger Cancer Center, we conducted pilot studies on genetically-modified Kaposi's Sarcoma cells in an effort to evaluate HSLCI as a tool for studying the kinetics of lytic program activation in KSHV. Our studies used iSLK.219 cells, a genetically engineered endothelial cell line containing Doxycycline-inducible latent KSHV.¹⁹⁵ These cells also contain two fluorescent markers: green fluorescence protein (GFP), which is constitutively expressed, and red fluorescent protein (RFP), which is expressed exclusively during lytic replication of KSHV. All cells, media, and reagents were provided by the Damania lab.

Using this model, we aimed to study mass kinetics of iSLK.219 cells immediately after exposure to KSHV-inducing Doxycycline. Briefly, 2 mL of 5×10^4 cells were dosed with Doxycycline (1 $\mu\text{g/ml}$) and imaged by HSLCI for 65 hours (once every 15 minutes); both phase and fluorescent images were collected. Based on this approach, we would expect to see green fluorescence in individual cells which transitions to yellow as KSHV lytic programs are activated and RFP expression begins. This experiment was repeated three times ($n_{\text{avg}} = 600$ cells/experiment).

Several interesting trends were observed. First, as measured by the emergence of red fluorescence, approximately 20-24 hours is required for Doxycycline to induce KSHV's lytic program. Second, three hours after lytic activation, cell growth ceased. This "static" period lasted for approximately 30 hours, followed by a slow loss of mass and, finally, cell death. A representative single-cell example of these observations is provided in **Figure 29**.

In addition to fulfilling their role as a proof of concept for our ability to conduct multi-day fluorescent imaging runs, these experiments show that, at least in KSHV, lytic activation has a distinct kinetic signature. This has implications for basic virology research as changes in cell growth patterns can give clues to the involvement of specific pathways during the latent-lytic switch. Further, it could provide a label-free metric of lytic activation for wild type cells. Beyond KSHV, HSLCI could be used to study the kinetics of primary infection in across a range of viruses and cell types.

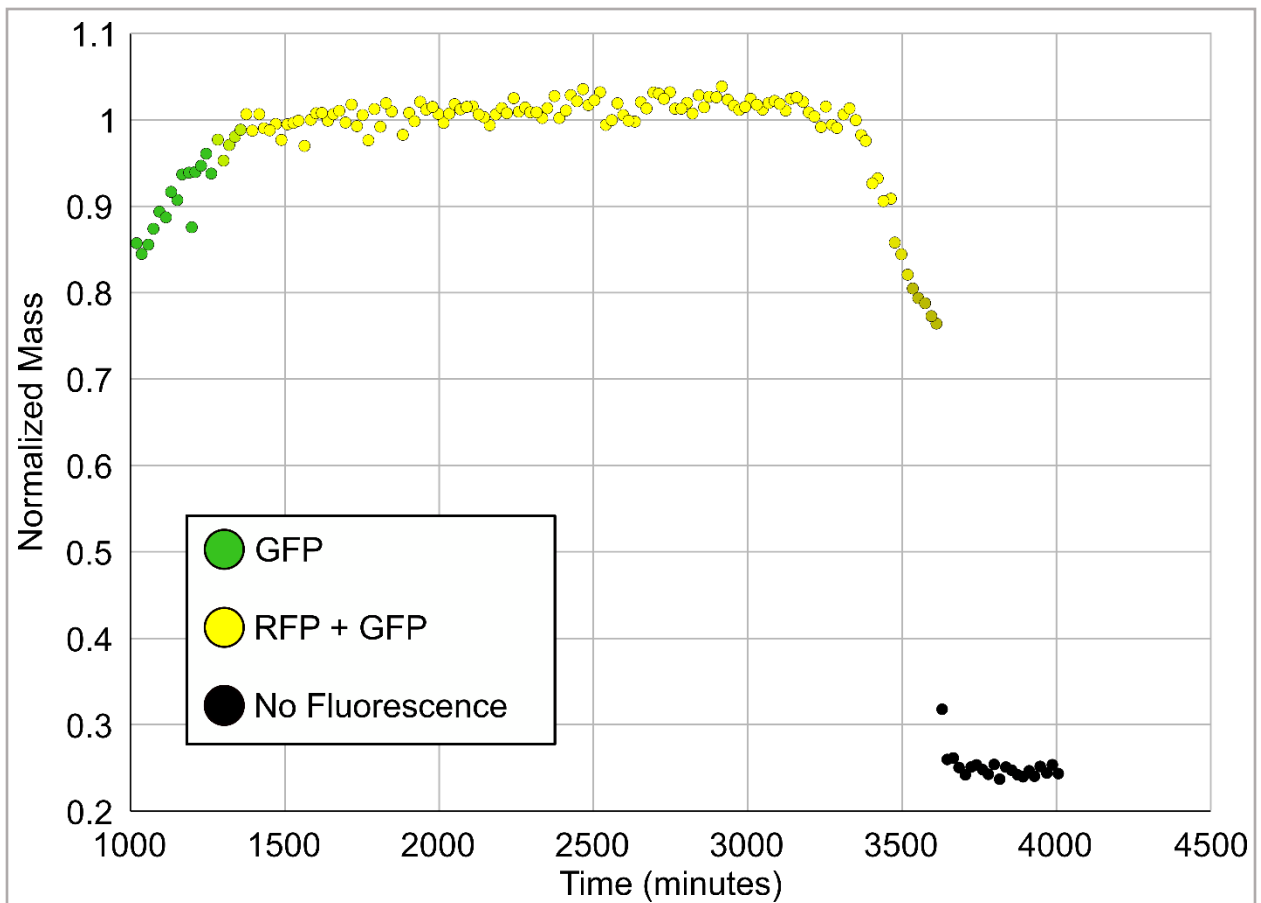


Figure 29. Single-cell Doxycycline-induced KSHV lytic activation. A representative plot of cell mass versus time for a single iSLK.219 cell dosed at 0 minutes with Doxycycline. Individual point coloration indicates the fluorescence color emitted by the cell (i.e. yellow indicates simultaneous GFP and RFP expression, black indicates a lack of fluorescence). Note: iSLK.219 cells constitutively express GFP and contain latent, Doxycycline-inducible KSHV virus. Induction of the virus' lytic program with Doxycycline also induces RFP expression.

Chapter 6

Conclusions and Future Directions

6.0 Chapter Overview

This chapter provides a summary of the work presented thus far, an overview of ongoing HSLCI experiments, and a discussion of future directions.

6.2 Summary of Work Presented

Cell mass is emerging as an important indicator of cell health and status. Improvements in digital imaging and processing technologies have enabled quantitative phase imaging to become a precise method for non-invasively studying cell mass kinetics at the single-cell level. Our work using the LCI and HSLCI systems has resulted in several important achievements. First, we have demonstrated an ability to measure cells continuously for over 10 days. This is significantly longer than similar QPI-based techniques and provides a sufficient window of time to observe the vast majority of cellular processes. Second, we have demonstrated an ability to handle a range of sample types on the same instrument, including single cells and clusters, non-adherent and adherent cells, and established cell lines and patient samples. Third, the HSLCI has enabled us to visualize unique mast cell populations and processes, as well as confirmed our ability to conduct correlative fluorescent studies. Fourth, our work with melanoma validated LCI and HSLCI in two independent laboratories. We demonstrated an ability to quantify heterogeneous responses to therapeutics and discriminate between drug-sensitive and drug-resistant cells in multiple patient-derived melanoma cell lines, adding to the body of evidence that the *in vitro* measurement of cell mass after drug exposure can achieve the resolution and throughput necessary to be clinically relevant. Finally, our pioneering work on T cell mass dynamics during immune reconstitution revealed previously undescribed kinetics that could be informative in

tailoring post-transplant immunosuppression. In summary, we have developed, validated, and deployed a microscopy platform that has the potential to become a powerful tool in applications from the bench to the bedside.

6.3 Ongoing Work

Work by several members of the Reed laboratory, including Graeme Murray and Daniel Guest, have resulted in numerous improvements in HSLCI system performance (enabling imaging speeds of 16 fps, 4X faster than described in our work on melanoma) and an expansion of its applications. The following sub-sections describe ongoing HSLCI pilot projects.

6.3.1 Drug-Induced Cellular Senescence

Senescence, is a protective and stable state in which the cell cycle has been arrested in response to a variety of signals, including telomere shortening, drug exposure, and the expression of growth-promoting oncogenes.¹⁹⁶ For previously-healthy cells, entering a senescent state can help prevent the development of malignancies.¹⁹⁷ In cancer cells, senescence induced by chemotherapy or radiation treatments can have the opposite effect: promoting aggressive drug-resistant phenotypes.^{198,199} As such, the characterization and quantification of therapy-induced senescence is an urgent and important area of research for improving patient outcomes.

In collaboration with Dr. David Gewirtz in the VCU Department of Pharmacology and Toxicology, our lab is conducting pilot studies on the mass kinetics of drug-induced senescence in cancer cells. Briefly, H460 (lung carcinoma) cells are exposed to Etoposide, a chemotherapeutic used in the treatment of a range of solid tumor and blood cancers. Following drug exposure, cells are sorted into senescent and non-senescent groups by flow cytometry using an established

fluorescent marker for cellular senescence ($C_{12}FDG$, a modified substrate of β -galactosidase).²⁰⁰

Sorted groups are then imaged by HSLCI for up to six days to measure cell mass and detect proliferative recovery. Three replicates of this experiment have been performed, to-date.

Our data indicate that cells sorted as “senescent” are 3-4X larger in mass and area than both control cells and drug-treated cells that did not become senescent. These larger cells, though theoretically growth static, exhibited mass accumulation rates of 1% per hour, while non-senescent treated and control cells grew at approximately 3% per hour. In addition, a small percentage of senescent cells eventually transitioned into a rapidly-growing (3% per hour) state and, subsequently, divided at three or more days, post-treatment. While further experimental replicates are required to confirm the reproducibility of these trends, the data demonstrate our ability to detect changes in proliferative states and quantify the heterogeneity of responses in senescent lung carcinoma cells. In addition to aiding the characterization of drug-induced senescence as a process, this approach could help in screening new and existing therapeutics for their propensity to promote drug resistance.²⁰¹

6.3.2 Effect of Radiation on Endothelial Cells

Prostate cancer is the most commonly-diagnosed cancer in men.²⁰² Treatment generally consists of classical chemotherapy, hormone ablation, or radiotherapy (targeted radiation).²⁰³ Morbidity and mortality vary significantly by socioeconomic status, ethnicity, and geographic location.²⁰⁴ Even taking into account disparities in access to medical care and screening, men of African descent have significantly worse outcomes, including higher rates of radiation treatment-induced side effects like erectile dysfunction and proctitis.²⁰⁵ Single-nucleotide polymorphism

(SNP) and genome-wide association studies (GWAS) have both supported these observations.²⁰⁶

The underlying cause of many of the observed side effects and poor treatment outcomes is radiation-induced damage to endothelial cells that make up critical vasculature around the prostate.^{207,208}

In this context, our lab is evaluating HSLCI, in collaboration with Dr. Ross Mikkelsen in the VCU Department of Radiation Oncology, as a tool to measure the effects of radiation exposure in endothelial cells. These pilot studies utilize EA.hy926 cells, a hybrid cell type that is a fusion of drug-resistant lung cancer with human umbilical vein cells.²⁰⁹ Briefly, EA.hy926 cells are exposed to a range of radiation doses (0, 2, 4, and 8 Gray (Gy)), seeded in a multi-well plate, incubated for eight hours, and then observed using HSLCI for 24 hours to measure mass kinetics. This experiment has been repeated two times.

Interestingly, dose-dependent increases in median population mass were observed in treated groups. Specifically, while control cells grew and then divided, division in treated populations was not observed. Instead, treated cells accumulated mass but did not divide, with the 8 Gy group exhibiting the largest median cell masses at 32 hours, post-dosing. Follow-on studies aim to reproduce these results while observing cells over a longer time window to detect any cell divisions in treated groups. We hope to continue this work by comparing responses of cell lines derived from Caucasian and African American patients in an effort to better understand the effects of radiation therapy and, potentially, develop markers for the retroactive quantification of radiation exposure.

6.3.3 PDX Models with HSLCI to Study Drug Resistance

HSLCI is highly complementary to a powerful emerging clinical research tool: patient-derived xenografts (PDX). PDX models maintain the genetic and histologic characteristics of the patient from whom they originate.^{210–213} Therapeutic compound screening in these models can identify drugs that are effective in treating tumors from the patients from which they were derived and/or for patients with a similar genomic profile. One of the best attributes of PDX models is that they are maintained within an *in vivo* setting from the time they are isolated from a patient. This feature conserves cellular heterogeneity by avoiding clonal selection due to 2D culturing on plastic surfaces. Further, cell-to-cell variability observed within established cell lines has been well documented, and studies with transgenic models have revealed genomic mechanisms that drive drug resistance in response to targeted therapeutics.^{214–216} Pairing HSLCI with PDX models could enable the rapid identification of patient-specific efficacious chemotherapeutics.

We have tested the HSLCI system with patient-derived melanoma, breast, brain, lung, and blood cancer cell lines, as well as PDX lines. The platform is unique among biomass measurement methods in its combination of sampling depth, speed, and compatibility with both adherent and non-adherent cells, single cells and cell clusters.

An overview of PDX model generation and usage methodologies is shown in **Figure 30**. Briefly, a tumor surgically resected from a cancer patient is disaggregated into a single-cell suspension. The suspension is transplanted into an immunodeficient mouse and allowed to grow. After sufficient growth, the tumor is removed and transplanted into a second immunodeficient mouse for tumor expansion. Expanded tumors can then be utilized in studies or cryopreserved for future use.²¹⁷

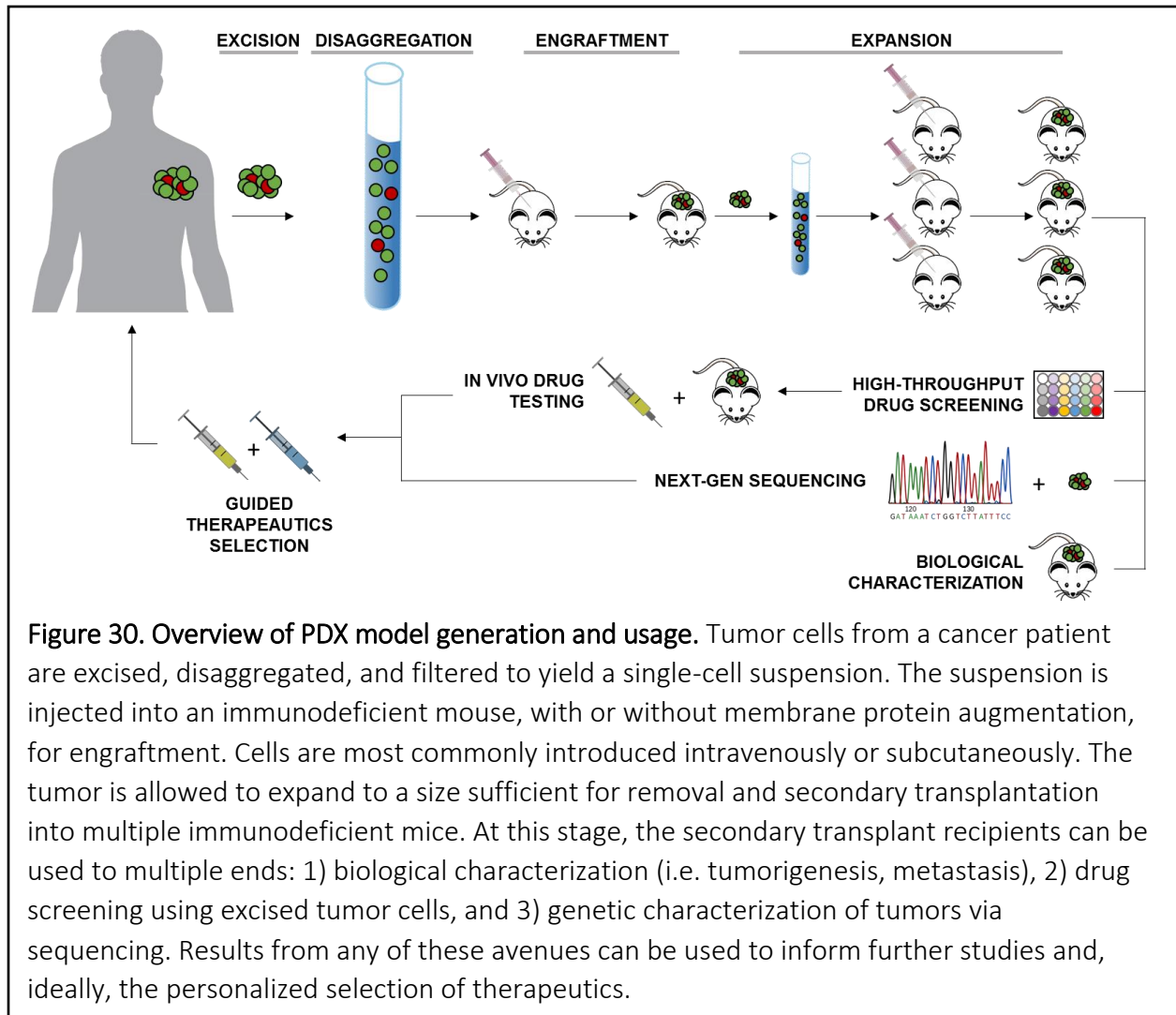


Figure 30. Overview of PDX model generation and usage. Tumor cells from a cancer patient are excised, disaggregated, and filtered to yield a single-cell suspension. The suspension is injected into an immunodeficient mouse, with or without membrane protein augmentation, for engraftment. Cells are most commonly introduced intravenously or subcutaneously. The tumor is allowed to expand to a size sufficient for removal and secondary transplantation into multiple immunodeficient mice. At this stage, the secondary transplant recipients can be used to multiple ends: 1) biological characterization (i.e. tumorigenesis, metastasis), 2) drug screening using excised tumor cells, and 3) genetic characterization of tumors via sequencing. Results from any of these avenues can be used to inform further studies and, ideally, the personalized selection of therapeutics.

Successful PDX model generation depends upon the optimization of several parameters, including the choice of an appropriate genetic background of immunodeficient mouse and selection of transplantation methodology and location. These choices depend both on the type of cancer being transplanted and the overall research aims. Specifically, establishment of models from primary tumor samples requires mice with a high degree of immunodeficiency and, therefore, necessitates the use of mouse strains such as NOD/SCID/IL2rg^{-/-} (NSI), which lack B, NK, and T cells. Further, these models are now frequently humanized after transplantation via

the infusion of human hematopoietic stem cells to better mimic the human immune environment, improving the model's general relevance. To enhance the likelihood of successful tumor establishment, transplantation of cells into these mice is frequently augmented with basement membrane proteins (i.e. Matrigel, Corning, Inc.) and/or fibroblasts and endothelial cells. Intravenous and subcutaneous (heterotopic) injections are the most common for initial implantation due to their relative technical simplicity and ease of monitoring, though organ-specific (orthotopic) implantation is an option that, theoretically, better mirrors the environment of human tumors. Once established, PDX models are valuable tools for both basic and preclinical cancer research. In addition to enabling the study of complex processes like metastasis and tumorigenesis, they provide a platform for screening drugs and identifying new therapeutic targets, both *in vitro* and *in vivo*.²¹⁸⁻²²⁰

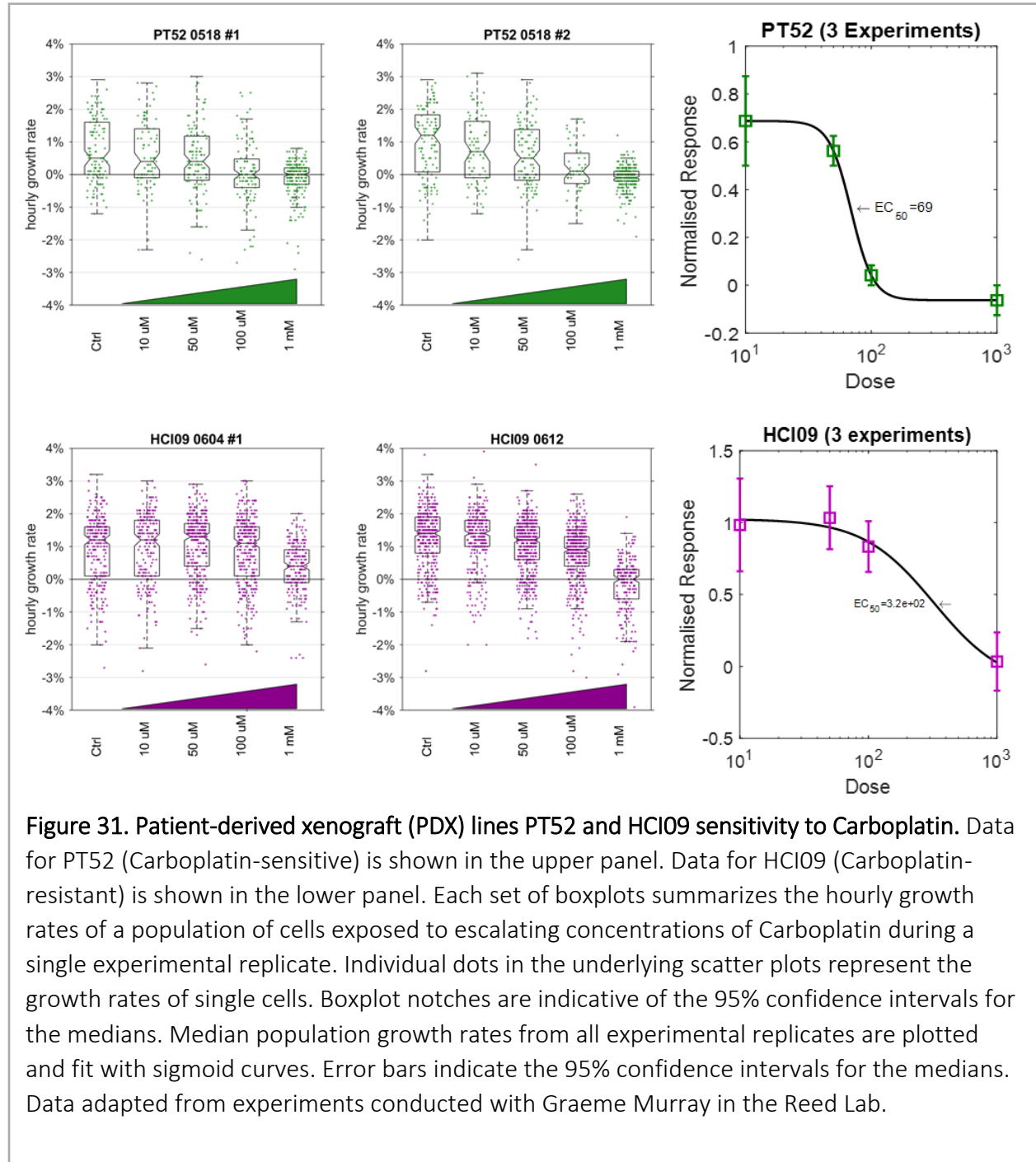
In collaboration with Dr. Chuck Harrell in the VCU Department of Pathology, we are investigating drug responses in PDX models of Triple-Negative Breast cancer (TNBC). Briefly, in 2018, an estimated 266,000 women in the United States will be diagnosed with invasive breast cancer and ~40,000 will die of the disease.⁸² The annual death rate due to breast cancer has declined over the past several decades due to earlier detection and advances in our understanding of the disease's molecular subtypes, which govern treatment and predict prognosis.^{221,222} However, clinical courses and outcomes for this common malignancy remain variable despite the use of therapies guided by a combination of clinical assessments that include tumor subtyping, clinical grading and staging, and the expression of estrogen (ER), progesterone (PR), or amplified HER2/neu cell surface receptors.^{223,224}

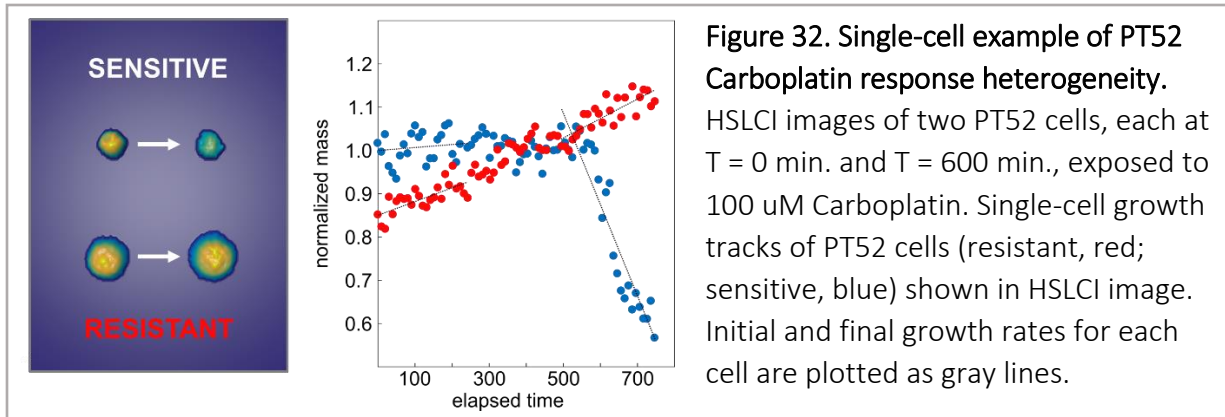
Accounting for ~15% of all breast cancers, TNBC is a particularly aggressive form of the disease that often metastasizes to vital organs, including the brain, bone, liver, and lungs.^{225–228} Breast tumors that are genetically characterized as basal-like tumors (most of which are TNBC) often metastasize before they are surgically resected.^{221,222,229} This metastatic propensity contributes to the poor prognosis associated with this subtype.^{230,231} Women with TNBC are limited to receiving chemotherapy and, despite highly toxic therapeutic regimens, many eventually die from the burden of their disease.^{93,94,232,233}

Repeated assessments of tumor sensitivity to available therapeutics could improve clinical outcomes by staying ahead of developing drug resistance in patients with breast and other cancers. Therefore, the main goal of our current collaboration is to determine whether HSLCI can predict *in vivo* PDX drug sensitivity and resistance and, eventually, to assess the ability of the HSLCI to characterize mechanisms of tumor heterogeneity in PDX breast cancer models. Over the past four years, Dr. Harrell has developed a set of models and methods to study the growth, progression, and molecular mechanisms driving drug sensitivity within breast cancer PDX models. The focus of our current efforts are PDXs that represent the most aggressive breast cancer subtypes. These include TNBCs WHIM2, WHIM30, HCI01, HCI09, and HCI10. Each of the PDX models we are investigating has been RNA-Seq expression profiled and analyzed by immunohistochemistry for ER, PR, and HER2 status. Dr. Harrell has experience growing each PDX model as mammary tumors and has quantified their growth rates.

Thus far, we have demonstrated a capability to detect cell growth and death responses in cells freshly isolated from the WHIM2, WHIM30, HCI01, HCI09, HCI11, and PT52 TNBC PDX mouse models with the HSLCI platform. An example of this drug sensitivity data from two PDX lines is

provided in Figure 31, while an example of our ability to resolve drug resistance at the single-cell level is provided in Figure 32.





Importantly, the drug responses measured to-date match those observed in *in vivo* studies conducted by Dr. Harrell (i.e. tumors sensitive to drug administered are also sensitive *in vitro*). This data establishes the viability of the sample handling techniques we will use to obtain HSLCI-measurable results from surgically resected material, and lays the groundwork for large-scale studies for quantifying drug resistance and heterogeneity.

6.4 Future Directions

Following the efforts described above, additional studies are planned to expand the scope of previous experiments and keep pace with emerging trends.

6.4.1 Three-Dimensional Cell Culture

While two-dimensional *in vitro* culturing remains dominant in cancer and drug development studies, mounting evidence on the importance of the tumor microenvironment has led to the emergence of new three-dimensional techniques that aim to better mimic *in vivo* conditions.²³⁴⁻

²³⁶ Specifically, two-dimensional cultures lack stromal cells and features like the extracellular matrix, have altered rates of drug diffusion, and subject cells to different surface textures than encountered in the body, all of which can alter behavior and responses to therapeutics. Tumor

spheroids and organoids are two distinct but similar 3D approaches that have been developed to address these concerns.^{237,238}

There is currently no single standard protocol for developing these 3D models. Spheroids typically refer to self-assembled spherical aggregates of cells several hundred microns in diameter.²³⁹ Creating them involves starting with purified tumor cells (though mixed populations can be used) and using a variety of techniques to encourage them to form such assemblages. Some methods rely on preventing adhesion to culture vessel surfaces to promote cell clustering, while others use a synthetic extracellular matrix called Matrigel (Corning Life Sciences, Inc.) to foster 3D architectures and separate tumor cells from fibroblast feeder layers.²⁴⁰ Others keep cells suspended under continuous motion to prevent adhesion; some allow them to sediment to the bottoms of individual media droplets. Finally, a whole range of micropatterned surfaces have been created to coax cells into various shapes and structures using microfluidics. Organoids generally refer to slightly larger, more complex, and more organized clusters of tissue excised from a mouse or human using enzymatic and mechanical digestion.²⁴¹ Once excised, these primary organoids are often similarly cultured in Matrigel or collagen. Spheroids and organoids can eventually be transferred to traditional multi-well plates for imaging, or cultured in custom PDMS molds which allow gas and nutrient diffusion and have refractive indices similar to glass. As 3D culture becomes more common, it will be necessary to demonstrate HSLCI's compatibility with spheroids and organoids.²⁴² We have already shown an ability to reliably image cell clumps and clusters in two-dimensional culture models. Therefore, the biggest challenge will be the acquisition of data from different focal planes. If we aim to simply study whole clusters, generating this data requires no modifications to our system because our measurements take

into account the entire optical path of the light measured, whether it passes through one cell or ten. However, if we hope to maintain single-cell resolution for correlative fluorescent imaging, image acquisition approaches similar to those employed by confocal microscopy will be considered, in addition to the incorporation of additional QPI modalities like DHM or spatial light interference microscopy (SLIM).²⁴³

6.4.2 Large-Scale Patient Studies

A logical extension of our completed and ongoing experiments is the design of larger scale patient studies. For our work in melanoma, HSLCI dose response testing of primary tumor samples prior to the administration of therapeutic regimens would enable a comparison of our assays' outcomes with actual patient responses. With this material, we could also begin attempts at comparing 2D and 3D culture methodologies in parallel. In addition, these assays could be performed for other cancers in which biopsies are straightforward to attain, including breast and blood cancers. Other groups have demonstrated success in correlating drug-induced *in vitro* mass changes with therapeutic efficacy in small numbers of patients.⁵⁷ If HSLCI is to be adapted for clinical use, this type of validation will be a mandatory next step.

Regarding our work in T cells, follow-on studies with larger patient cohorts will enable several lines of inquiry. First, considering the small size of our pilot study, we would hope to reproduce the trends we observed in our original data and increase the number of control group patients (autologous transplant recipients). Second, we hope to identify important T cell subsets that could enhance the resolution of our kinetic signatures. Accomplishing this goal requires both more patient material and additional resources for requisite analyses. Finally, given the range of

diseases that can lead to the need for SCT and the broad demographics of those patient populations, a larger cohort would help us account for any effects these variables might impart.²⁴⁴

6.5 Conclusion

HSLCI shows promise as a powerful and versatile research tool. We have demonstrated its compatibility with a wide range of cell types and applications and validated its performance in two independent laboratories. At present, HSLCI's large data footprint is its most significant drawback, both in terms of the cost of data storage and time required for processing. Addressing this issue is, fortunately, straightforward given the existence of hardware solutions like powerful graphics processing units (GPUs) that are better suited to image-based tasks and high-capacity solid-state drives (SSDs) capable of rapidly reading and writing data. In addition, minor software modifications will streamline data acquisition and analysis, increasing the efficiency of storage and processing times. These improvements, coupled with our laboratory's ongoing work and planned studies, will enable HSLCI to continue contributing to the understanding of mass kinetics and their importance in biology and medicine.

References

1. Lloyd, A. C. The Regulation of Cell Size. *Cell* **154**, 1194–1205 (2013).
2. Mueller, R. L. Genome Biology and the Evolution of Cell-Size Diversity. *Cold Spring Harbor Perspectives in Biology* **7**, a019125 (2015).
3. Levin, P. A. & Angert, E. R. Small but Mighty: Cell Size and Bacteria. *Cold Spring Harbor Perspectives in Biology* **7**, a019216 (2015).
4. O'Farrell, P. H. Growing an Embryo from a Single Cell: A Hurdle in Animal Life: Figure 1. *Cold Spring Harbor Perspectives in Biology* **7**, a019042 (2015).
5. Hindupur, S. K., González, A. & Hall, M. N. The Opposing Actions of Target of Rapamycin and AMP-Activated Protein Kinase in Cell Growth Control. *Cold Spring Harbor Perspectives in Biology* **7**, a019141 (2015).
6. Amodeo, A. A. & Skotheim, J. M. Cell-Size Control. *Cold Spring Harbor Perspectives in Biology* **8**, a019083 (2015).
7. LeGoff, L. & Lecuit, T. Mechanical Forces and Growth in Animal Tissues. *Cold Spring Harbor Perspectives in Biology* **8**, a019232 (2015).
8. Penzo-Méndez, A. I. & Stanger, B. Z. Organ-Size Regulation in Mammals. *Cold Spring Harbor Perspectives in Biology* **7**, a019240 (2015).
9. Reber, S. & Goehring, N. W. Intracellular Scaling Mechanisms. *Cold Spring Harbor Perspectives in Biology* a019067 (2015).doi:10.1101/cshperspect.a019067
10. Lemons, J. M. S. *et al.* Quiescent fibroblasts exhibit high metabolic activity. *PLoS biology* **8**, e1000514 (2010).
11. Loffredo, F. S. *et al.* Growth differentiation factor 11 is a circulating factor that reverses age-related cardiac hypertrophy. *Cell* **153**, 828–839 (2013).
12. Collins, M. J., Napoli, I., Ribeiro, S., Roberts, S. & Lloyd, A. C. Loss of Rb Cooperates with Ras to Drive Oncogenic Growth in Mammalian Cells. *Current Biology* **22**, 1765–1773 (2012).
13. Crino, P. B. mTOR: A pathogenic signaling pathway in developmental brain malformations. *Trends in molecular medicine* **17**, 734–742 (2011).
14. Milo, R., Jorgensen, P., Moran, U., Weber, G. & Springer, M. BioNumbers—the database of key numbers in molecular and cell biology. *Nucleic acids research* **38**, D750–D753 (2010).
15. Summers, C. *et al.* Neutrophil kinetics in health and disease. *Trends in Immunology* **31**, 318–324 (2010).
16. Ernst, A. & Frisén, J. Adult neurogenesis in humans- common and unique traits in mammals. *PLoS biology* **13**, e1002045 (2015).
17. Weber, T. S., Jaehnert, I., Schichor, C., Or-Guil, M. & Carneiro, J. Quantifying the Length and Variance of the Eukaryotic Cell Cycle Phases by a Stochastic Model and Dual Nucleoside Pulse Labelling. *PLoS Computational Biology* **10**, e1003616 (2014).
18. Alberts, B. *Molecular Biology of The Cell*. (Garland Science: 2008).
19. Iritani, B. M. *et al.* Modulation of T-lymphocyte development, growth and cell size by the Myc antagonist and transcriptional repressor Mad1. *The EMBO journal* **21**, 4820–4830 (2002).

20. Böhmer, R. M., Bandala-Sanchez, E. & Harrison, L. C. Forward light scatter is a simple measure of T-cell activation and proliferation but is not universally suited for doublet discrimination. *Cytometry Part A* **79A**, 646–652 (2011).
21. Malik, N. M., Gilroy, D. W. & Kabouridis, P. S. Regulation of growth and survival of activated T cells by cell-transducing inhibitors of Ras. *FEBS letters* **583**, 61–69 (2009).
22. Krystel-Whittemore, M., Dileepan, K. N. & Wood, J. G. Mast Cell: A Multi-Functional Master Cell. *Frontiers in immunology* **6**, 620 (2015).
23. Qin, S. *et al.* Cell-based phenotypic screening of mast cell degranulation unveils kinetic perturbations of agents targeting phosphorylation. *Scientific reports* **6**, 31320 (2016).
24. Barer, R., Ross, K. F. A. & Tkaczyk, S. Refractometry of living cells. *Nature* **171**, 720–724 (1953).
25. Chun, J. *et al.* Rapidly quantifying drug sensitivity of dispersed and clumped breast cancer cells by mass profiling. *The Analyst* **137**, 5495 (2012).
26. Bon, P., Maucort, G., Wattellier, B. & Monneret, S. Quadriwave lateral shearing interferometry for quantitative phase microscopy of living cells. *Optics express* **17**, 13080–13094 (2009).
27. Rappaz, B. *et al.* Noninvasive characterization of the fission yeast cell cycle by monitoring dry mass with digital holographic microscopy. *Journal of Biomedical Optics* **14**, 034049 (2009).
28. Stevens, M. M. *et al.* Drug sensitivity of single cancer cells is predicted by changes in mass accumulation rate. *Nature biotechnology* **34**, 1161–1167 (2016).
29. M. Fukuda, A. S. Biochemical studies on the number and the composition of liver cells in postnatal growth of the rat. *Journal of Biochemistry* **40**, 95–110 (1953).
30. Nie, Z. *et al.* High-speed mass analysis of whole erythrocytes by charge-detection quadrupole ion trap mass spectrometry. *Analytical chemistry* **79**, 7401–7407 (2007).
31. Ruch, F. & Bahr, G. F. Dry mass determination by interference microscopy; agreement with quantitative electron microscopy. *Experimental cell research* **60**, 470 (1970).
32. Barer, R. Interference microscopy and mass determination. *Nature* **169**, 366–367 (1952).
33. Boseck, S. Extension of the pehland and hager theory of interference-microscope dry-mass determination of biological substances to optically anisotropic systems. *Optik* 1–4 (1966).
34. Popescu, G. Quantitative phase imaging of nanoscale cell structure and dynamics. *Methods in cell biology* **90**, 87–115 (2008).
35. Burg, T. P. *et al.* Weighing of biomolecules, single cells and single nanoparticles in fluid. *Nature* **446**, 1066–1069 (2007).
36. Godin, M. *et al.* Using buoyant mass to measure the growth of single cells. *Nature methods* **7**, 387–390 (2010).
37. Brown, A. F. & Dunn, G. A. Microinterferometry of the movement of dry matter in fibroblasts. *Journal of Cell Science* **92**, 379–389 (1989).
38. Davies, H. G. & Wilkins, M. H. F. Interference microscopy and mass determination. *Nature* **169**, 541 (1952).
39. Adair, G. S. & Robinson, M. E. The specific refraction increments of serum-albumin and serum-globulin. *The Biochemical journal* **24**, 993–1011 (1930).
40. Davies, H. On microscope interferometry and the specific refraction increment of a crystalline protein. *JOURNAL OF HISTOCHEMISTRY & CYTOCHEMISTRY* **6**, 393–393 (1958).

41. Grampp, W., HALLEN, O. & ROSENGREN, B. Mass determination by interference- and x-ray microscopy. A comparative study. *Experimental cell research* **19**, 437–442 (1960).
42. Ottoson, R., KAHN, K. & GLICK, D. Studies in histochemistry. XLVIII. Dry mass of mast cells measured by interference microscopy and x-ray absorption. *Experimental cell research* **14**, 567–574 (1958).
43. Magnani, M. *et al.* Effect of age on some properties of mice erythrocytes. *Mechanisms of ageing and development* **42**, 37–47 (1988).
44. Myśliwski, A. & Lass, P. Increase of size and dry mass of mouse erythrocytes depending on age of donors. *Mechanisms of ageing and development* **29**, 107–110 (1985).
45. Barer, R. Refractometry and interferometry of living cells. *Journal of the Optical Society of America* **47**, 545–556 (1957).
46. Barer, R. & Joseph, S. Refractometry of Living Cells. Part 1. Basic principles. *Journal of Cell Science* **s3-95**, 399–423 (1954).
47. Davies, H. G., WILKINS, M. H. F., CHAYEN, J. & LA COUR, L. F. The Use of the Interference Microscope to Determine Dry Mass in Living Cells and as a Quantitative Cytochemical Method. *Journal of Cell Science* **s3-95**, 271–304 (1954).
48. Ross, K. F. A. *Phase Contrast and Interferencce Microscopy for Cell Biologists*. (Edward Arnold: 1967).
49. Barer, R. & Joseph, S. Refractometry of Living Cells. Part 3. Technical and optical methods. *Journal of Cell Science* **s3-96**, 423–447 (1955).
50. Gamble, C. N. & Glick, D. Studies in Histochemistry. *The Journal of Cell Biology* **8**, 53–60 (1960).
51. Loferer-Krössbacher, M., Klima, J. & Psenner, R. Determination of bacterial cell dry mass by transmission electron microscopy and densitometric image analysis. *Applied and environmental microbiology* **64**, 688–694 (1998).
52. Zhao, Y., Lai, H. S. S., Zhang, G., Lee, G.-B. & Li, W. J. Measurement of single leukemia cell's density and mass using optically induced electric field in a microfluidics chip. *Biomicrofluidics* **9**, 022406 (2015).
53. Phillips, K. G., Jacques, S. L. & McCarty, O. J. T. Measurement of single cell refractive index, dry mass, volume, and density using a transillumination microscope. *Physical review letters* **109**, 118105 (2012).
54. Pastina, A. D., Maillard, D. & Villanueva, L. G. Fabrication of suspended microchannel resonators with integrated piezoelectric transduction. *Microelectronic Engineering* **192**, 83–87 (2018).
55. Lee, J. *et al.* Suspended microchannel resonators with piezoresistive sensors. *Lab Chip* **11**, 645–651 (2011).
56. Popescu, G., Park, K., Mir, M. & Bashir, R. New technologies for measuring single cell mass. *Lab on a chip* **14**, 646–652 (2014).
57. Cetin, A. E. *et al.* Determining therapeutic susceptibility in multiple myeloma by single-cell mass accumulation. *Nature communications* **8**, 1613 (2017).
58. Kimmerling, R. J. *et al.* Linking single-cell measurements of mass, growth rate, and gene expression. (2018).doi:10.1101/331686
59. Park, K. *et al.* Measurement of adherent cell mass and growth. *Proceedings of the National Academy of Sciences of the United States of America* **107**, 20691–20696 (2010).

60. Park, Y. *et al.* Measurement of red blood cell mechanics during morphological changes. *Proceedings of the National Academy of Sciences of the United States of America* **107**, 6731–6736 (2010).
61. Corbin, E. A., Dorvel, B. R., Millet, L. J., King, W. P. & Bashir, R. Micro-patterning of mammalian cells on suspended MEMS resonant sensors for long-term growth measurements. *Lab on a Chip* **14**, 1401 (2014).
62. Mellors, R. C., KUPFER, A. & HOLLENDER, A. Quantitative cytology and cytopathology. I. Measurement of the thickness, the volume, the hydrous mass, and the anhydrous mass of living cells by interference microscopy. *Cancer* **6**, 372–384 (1953).
63. Creath K, S. J. Encyclopedia of Modern Optics. 364–374 (2005).
64. Majeed, H. *et al.* Quantitative phase imaging for medical diagnosis. *Journal of biophotonics* **10**, 177–205 (2017).
65. Marquet, P., Depeursinge, C. & Magistretti, P. J. Review of quantitative phase-digital holographic microscopy: promising novel imaging technique to resolve neuronal network activity and identify cellular biomarkers of psychiatric disorders. *Neurophotonics* **1**, 020901 (2014).
66. Zeng, Y., Chang, X., Lei, H., Hu, X. & Hu, X. Characteristics analysis of digital image-plane holographic microscopy. *Scanning* **38**, 288–296 (2016).
67. Calabuig, A., Mugnano, M., Miccio, L., Grilli, S. & Ferraro, P. Investigating fibroblast cells under “safe” and “injurious” blue-light exposure by holographic microscopy. *Journal of biophotonics* **10**, 919–927 (2017).
68. Mir, M. *et al.* Optical measurement of cycle-dependent cell growth. *Proceedings of the National Academy of Sciences* **108**, 13124–13129 (2011).
69. Pavillon, N. *et al.* Early Cell Death Detection with Digital Holographic Microscopy. *PLoS ONE* **7**, e30912 (2012).
70. Bon, P., Savatier, J., Merlin, M., Wattellier, B. & Monneret, S. Optical detection and measurement of living cell morphometric features with single-shot quantitative phase microscopy. *Journal of biomedical optics* **17**, 076004 (2012).
71. Anand, A., Chhaniwal, V. K. & Javidi, B. Imaging Embryonic Stem Cell Dynamics Using Quantitative 3-D Digital Holographic Microscopy. *IEEE Photonics Journal* **3**, 546–554 (2011).
72. Singh, D. K., Ahrens, C. C., Li, W. & Vanapalli, S. A. Label-free, high-throughput holographic screening and enumeration of tumor cells in blood. *Lab on a Chip* **17**, 2920–2932 (2017).
73. Li, Y., Petrovic, L., La, J., Celli, J. P. & Yelleswarapu, C. S. Digital holographic microscopy for longitudinal volumetric imaging of growth and treatment response in three-dimensional tumor models. *Journal of Biomedical Optics* **19**, 116001 (2014).
74. Bettenworth, D. *et al.* Quantitative phase microscopy for evaluation of intestinal inflammation and wound healing utilizing label-free biophysical markers. *Histology and histopathology* **33**, 417–432 (2018).
75. Reed, J. *et al.* Live Cell Interferometry Reveals Cellular Dynamism During Force Propagation. *ACS Nano* **2**, 841–846 (2008).
76. Zangle, T. A., Teitell, M. A. & Reed, J. Live Cell Interferometry Quantifies Dynamics of Biomass Partitioning during Cytokinesis. *PLoS ONE* **9**, e115726 (2014).
77. Zangle, T. A., Chun, J., Zhang, J., Reed, J. & Teitell, M. A. Quantification of Biomass and Cell Motion in Human Pluripotent Stem Cell Colonies. *Biophysical Journal* **105**, 593–601 (2013).

78. Reed, J. *et al.* Rapid, Massively Parallel Single-Cell Drug Response Measurements via Live Cell Interferometry. *Biophysical Journal* **101**, 1025–1031 (2011).
79. Aknoun, S. *et al.* Living cell dry mass measurement using quantitative phase imaging with quadriwave lateral shearing interferometry: an accuracy and sensitivity discussion. *Journal of Biomedical Optics* **20**, 126009 (2015).
80. Savatier, J., Bon, P., Marguet, D. & Monneret, S. Correlative Microscopy of Living Cells between Fluorescence and Quantitative Phase Imaging with a High Resolution Wavefront Sensor. *Biophysical Journal* **100**, 356a (2011).
81. Huang, D. *et al.* High Speed Live Cell Interferometry: A New Method for Rapidly Quantifying Tumor Drug Resistance and Heterogeneity. *Analytical chemistry* (2018).doi:10.1021/acs.analchem.7b04828
82. Siegel, R. L., Miller, K. D. & Jemal, A. Cancer statistics, 2018. *CA: a cancer journal for clinicians* **68**, 7–30 (2018).
83. Rogers, H. W., Weinstock, M. A., Feldman, S. R. & Coldiron, B. M. Incidence Estimate of Nonmelanoma Skin Cancer (Keratinocyte Carcinomas) in the U.S. Population, 2012. *JAMA dermatology* **151**, 1081–1086 (2015).
84. Eskiocak, B. *et al.* Biomarker Accessible and Chemically Addressable Mechanistic Subtypes of BRAF Melanoma. *Cancer discovery* **7**, 832–851 (2017).
85. Kunz, M. & Hölzel, M. The impact of melanoma genetics on treatment response and resistance in clinical and experimental studies. *Cancer metastasis reviews* **36**, 53–75 (2017).
86. Zhang, T., Dutton-Regester, K., Brown, K. M. & Hayward, N. K. The genomic landscape of cutaneous melanoma. *Pigment cell & melanoma research* **29**, 266–283 (2016).
87. Shtivelman, E. *et al.* Pathways and therapeutic targets in melanoma. *Oncotarget* **5**, 1701–1752 (2014).
88. Welsh, S. J., Rizos, H., Scolyer, R. A. & Long, G. V. Resistance to combination BRAF and MEK inhibition in metastatic melanoma: Where to next? *European journal of cancer (Oxford, England : 1990)* **62**, 76–85 (2016).
89. Inamdar, G. S., Madhunapantula, S. V. & Robertson, G. P. Targeting the MAPK pathway in melanoma: why some approaches succeed and other fail. *Biochemical pharmacology* **80**, 624–637 (2010).
90. Simeone, E. *et al.* Combination Treatment of Patients with BRAF-Mutant Melanoma: A New Standard of Care. *BioDrugs : clinical immunotherapeutics, biopharmaceuticals and gene therapy* **31**, 51–61 (2017).
91. Luke, J. J., Flaherty, K. T., Ribas, A. & Long, G. V. Targeted agents and immunotherapies: optimizing outcomes in melanoma. *Nature reviews. Clinical oncology* **14**, 463–482 (2017).
92. Spagnolo, F. *et al.* BRAF-mutant melanoma: treatment approaches, resistance mechanisms, and diagnostic strategies. *OncoTargets and therapy* **8**, 157–168 (2015).
93. Ahronian, L. G. & Corcoran, R. B. Strategies for monitoring and combating resistance to combination kinase inhibitors for cancer therapy. *Genome medicine* **9**, 37 (2017).
94. Bedard, P. L., Hansen, A. R., Ratain, M. J. & Siu, L. L. Tumour heterogeneity in the clinic. *Nature* **501**, 355–364 (2013).

95. Wagle, N. *et al.* Dissecting therapeutic resistance to RAF inhibition in melanoma by tumor genomic profiling. *Journal of clinical oncology : official journal of the American Society of Clinical Oncology* **29**, 3085–3096 (2011).
96. Ulz, P., Heitzer, E., Geigl, J. B. & Speicher, M. R. Patient monitoring through liquid biopsies using circulating tumor DNA. *International journal of cancer* **141**, 887–896 (2017).
97. Huang, S. K. & Hoon, D. S. B. Liquid biopsy utility for the surveillance of cutaneous malignant melanoma patients. *Molecular oncology* **10**, 450–463 (2016).
98. Siravegna, G., Marsoni, S., Siena, S. & Bardelli, A. Integrating liquid biopsies into the management of cancer. *Nature reviews. Clinical oncology* **14**, 531–548 (2017).
99. De Luca, F. *et al.* Mutational analysis of single circulating tumor cells by next generation sequencing in metastatic breast cancer. *Oncotarget* **7**, 26107–26119 (2016).
100. Klinac, D., Gray, E. S., Millward, M. & Ziman, M. Advances in personalized targeted treatment of metastatic melanoma and non-invasive tumor monitoring. *Frontiers in oncology* **3**, 54 (2013).
101. Gold, B., Cankovic, M., Furtado, L. V., Meier, F. & Gocke, C. D. Do circulating tumor cells, exosomes, and circulating tumor nucleic acids have clinical utility? A report of the association for molecular pathology. *The Journal of molecular diagnostics : JMD* **17**, 209–224 (2015).
102. Cree, I. A. Designing personalised cancer treatments. *Journal of controlled release : official journal of the Controlled Release Society* **172**, 405–409 (2013).
103. Singer, C. F. *et al.* Response prediction to neoadjuvant chemotherapy: comparison between pre-therapeutic gene expression profiles and in vitro chemosensitivity assay. *PloS one* **8**, e66573 (2013).
104. Haglund, C. *et al.* In vitro evaluation of clinical activity and toxicity of anticancer drugs using tumor cells from patients and cells representing normal tissues. *Cancer chemotherapy and pharmacology* **69**, 697–707 (2012).
105. Bellot, G. L., Tan, W. H., Tay, L. L., Koh, D. & Wang, X. Reliability of tumor primary cultures as a model for drug response prediction: expression profiles comparison of tissues versus primary cultures from colorectal cancer patients. *Journal of cancer research and clinical oncology* **138**, 463–482 (2012).
106. Wiberg, K. *et al.* In vitro activity of bortezomib in cultures of patient tumour cells—potential utility in haematological malignancies. *Medical oncology (Northwood, London, England)* **26**, 193–201 (2009).
107. Burstein, H. J. *et al.* American Society of Clinical Oncology clinical practice guideline update on the use of chemotherapy sensitivity and resistance assays. *Journal of clinical oncology : official journal of the American Society of Clinical Oncology* **29**, 3328–3330 (2011).
108. Wu, B., Zhu, J.-S., Zhang, Y., Shen, W.-M. & Zhang, Q. Predictive value of MTT assay as an in vitro chemosensitivity testing for gastric cancer: one institution's experience. *World journal of gastroenterology* **14**, 3064–3068 (2008).
109. Franken, N. A. P., Rodermond, H. M., Stap, J., Haveman, J. & Bree, C. van Clonogenic assay of cells in vitro. *Nature protocols* **1**, 2315–2319 (2006).
110. Kurbacher, C. M. & Cree, I. A. Chemosensitivity testing using microplate adenosine triphosphate-based luminescence measurements. *Methods in molecular medicine* **110**, 101–120 (2005).

111. Whitehouse, P. A. *et al.* Heterogeneity of chemosensitivity of colorectal adenocarcinoma determined by a modified ex vivo ATP-tumor chemosensitivity assay (ATP-TCA). *Anti-cancer drugs* **14**, 369–375 (2003).
112. Mi, Z. *et al.* Feasibility assessment of a chemoresponse assay to predict pathologic response in neoadjuvant chemotherapy for breast cancer patients. *Anticancer research* **28**, 1733–1740 (2008).
113. Kurbacher, C. M. *et al.* Use of an ex vivo ATP luminescence assay to direct chemotherapy for recurrent ovarian cancer. *Anti-cancer drugs* **9**, 51–57 (1998).
114. Waldman, T. *et al.* Cell-cycle arrest versus cell death in cancer therapy. *Nature medicine* **3**, 1034–1036 (1997).
115. Murray, D., McWilliams, L. & Wigglesworth, M. High-Throughput Cell Toxicity Assays. *Methods in molecular biology (Clifton, N.J.)* **1439**, 245–262 (2016).
116. Pamenter, M. E. & Haddad, G. G. High-throughput cell death assays. *Methods in molecular biology (Clifton, N.J.)* **1254**, 153–163 (2015).
117. Kepp, O., Galluzzi, L., Lipinski, M., Yuan, J. & Kroemer, G. Cell death assays for drug discovery. *Nature reviews. Drug discovery* **10**, 221–237 (2011).
118. Kravtsov, V. D., Daniel, T. O. & Koury, M. J. Comparative analysis of different methodological approaches to the in vitro study of drug-induced apoptosis. *The American journal of pathology* **155**, 1327–1339 (1999).
119. Bosanquet, A. G., Burlton, A. R., Bell, P. B. & Harris, A. L. Ex vivo cytotoxic drug evaluation by DiSC assay to expedite identification of clinical targets: results with 8-chloro-cAMP. *British journal of cancer* **76**, 511–518 (1997).
120. Montero, J. *et al.* Drug-induced death signaling strategy rapidly predicts cancer response to chemotherapy. *Cell* **160**, 977–989 (2015).
121. Kenny, H. A. *et al.* Quantitative high throughput screening using a primary human three-dimensional organotypic culture predicts in vivo efficacy. *Nature communications* **6**, 6220 (2015).
122. Schayowitz, A. *et al.* Functional profiling of live melanoma samples using a novel automated platform. *PloS one* **7**, e52760 (2012).
123. Moriceau, G. *et al.* Tunable-combinatorial mechanisms of acquired resistance limit the efficacy of BRAF/MEK cotargeting but result in melanoma drug addiction. *Cancer cell* **27**, 240–256 (2015).
124. Dongen, J. J. M. van, Velden, V. H. J. van der, Brüggemann, M. & Orfao, A. Minimal residual disease diagnostics in acute lymphoblastic leukemia: need for sensitive, fast, and standardized technologies. *Blood* **125**, 3996–4009 (2015).
125. Leslie, K. A. *et al.* Reconstituting donor T cells increase their biomass following hematopoietic stem cell transplantation. *The Analyst* **143**, 2479–2485 (2018).
126. Leslie, K. *et al.* Single-Cell Mass Profiling of Reconstituting Donor T Cells Following Stem Cell Transplantation to Predict Alloreactivity. *Biology of Blood and Marrow Transplantation* **23**, S374 (2017).
127. Niederwieser, D. *et al.* Hematopoietic stem cell transplantation activity worldwide in 2012 and a SWOT analysis of the Worldwide Network for Blood and Marrow Transplantation Group including the global survey. *Bone marrow transplantation* **51**, 778–785 (2016).

128. MacDonald, K. P. A., Hill, G. R. & Blazar, B. R. Chronic graft-versus-host disease: biological insights from preclinical and clinical studies. *Blood* **129**, 13–21 (2017).
129. Sampson, J. K. *et al.* Whole exome sequencing to estimate alloreactivity potential between donors and recipients in stem cell transplantation. *British journal of haematology* **166**, 566–570 (2014).
130. Abdul Razzaq, B. *et al.* Dynamical System Modeling to Simulate Donor T Cell Response to Whole Exome Sequencing-Derived Recipient Peptides Demonstrates Different Alloreactivity Potential in HLA-Matched and -Mismatched Donor-Recipient Pairs. *Biology of blood and marrow transplantation : journal of the American Society for Blood and Marrow Transplantation* **22**, 850–861 (2016).
131. Zangle, T. A., Burnes, D., Mathis, C., Witte, O. N. & Teitell, M. A. Quantifying Biomass Changes of Single CD8⁺ T Cells during Antigen Specific Cytotoxicity. *PLoS ONE* **8**, e68916 (2013).
132. Toor, A. A. *et al.* Favorable outcomes in patients with high donor-derived T cell count after in vivo T cell-depleted reduced-intensity allogeneic stem cell transplantation. *Biology of blood and marrow transplantation : journal of the American Society for Blood and Marrow Transplantation* **18**, 794–804 (2012).
133. Toor, A. A. *et al.* Dynamical System Modeling of Immune Reconstitution after Allogeneic Stem Cell Transplantation Identifies Patients at Risk for Adverse Outcomes. *Biology of blood and marrow transplantation : journal of the American Society for Blood and Marrow Transplantation* **21**, 1237–1245 (2015).
134. Jones, N. *et al.* Metabolic Adaptation of Human CD4, `javax.xml.bind.JAXBElement@5b60efc8`, and CD8, `javax.xml.bind.JAXBElement@75320d64`, T-Cells to T-Cell Receptor-Mediated Stimulation. *Frontiers in immunology* **8**, 1516 (2017).
135. Cretenet, G. *et al.* Cell surface Glut1 levels distinguish human CD4 and CD8 T lymphocyte subsets with distinct effector functions. *Scientific Reports* **6**, (2016).
136. Martínez, C. *et al.* Pharmacodynamics of T cell function for monitoring pharmacologic immunosuppression after allogeneic hematopoietic stem cell transplantation. *International journal of hematology* **105**, 497–505 (2017).
137. Nguyen, H. D. *et al.* Metabolic reprogramming of alloantigen-activated T cells after hematopoietic cell transplantation. *The Journal of clinical investigation* **126**, 1337–1352 (2016).
138. Min, C. K. *et al.* The kinetics of circulating cytokines including IL-6, TNF-alpha, IL-8 and IL-10 following allogeneic hematopoietic stem cell transplantation. *Bone marrow transplantation* **28**, 935–940 (2001).
139. Furlan, S. N. *et al.* Systems analysis uncovers inflammatory Th/Tc17-driven modules during acute GVHD in monkey and human T cells. *Blood* **128**, 2568–2579 (2016).
140. Jameson, S. C. & Masopust, D. Diversity in T cell memory: an embarrassment of riches. *Immunity* **31**, 859–871 (2009).
141. Henden, A. S. & Hill, G. R. Cytokines in Graft-versus-Host Disease. *Journal of immunology (Baltimore, Md. : 1950)* **194**, 4604–4612 (2015).
142. Levine, J. E. *et al.* A prognostic score for acute graft-versus-host disease based on biomarkers: a multicentre study. *The Lancet Haematology* **2**, e21–e29 (2015).

143. Meier, J. *et al.* Fractal organization of the human T cell repertoire in health and after stem cell transplantation. *Biology of blood and marrow transplantation : journal of the American Society for Blood and Marrow Transplantation* **19**, 366–377 (2013).
144. Berrie, J. L. *et al.* Distinct oligoclonal T cells are associated with graft versus host disease after stem-cell transplantation. *Transplantation* **93**, 949–957 (2012).
145. Tsutsumi, Y. *et al.* Molecular Analysis of T-Cell Repertoire in Patients with Graft-Versus-Host Disease after Allogeneic Stem Cell Transplantation. *Leukemia & Lymphoma* **45**, 481–488 (2004).
146. Yew, P. Y. *et al.* Quantitative characterization of T-cell repertoire in allogeneic hematopoietic stem cell transplant recipients. *Bone marrow transplantation* **50**, 1227–1234 (2015).
147. Hartwell, M. J. *et al.* An early-biomarker algorithm predicts lethal graft-versus-host disease and survival. *JCI insight* **2**, e89798 (2017).
148. Chiaranunt, P., Ferrara, J. L. M. & Byersdorfer, C. A. Rethinking the paradigm: How comparative studies on fatty acid oxidation inform our understanding of T cell metabolism. *Molecular immunology* **68**, 564–574 (2015).
149. Michael Loschi, R. Regis Peffault de Latour Porcher *et al.* High Numbers Of Memory T Cells Are Associated With Higher Risk Of Grade II-IV Acute Gvhd After Human Allogeneic Transplantation. *Blood* **122**, 2061–2061 (2013).
150. Kühn, J. *et al.* Label-Free Cytotoxicity Screening Assay by Digital Holographic Microscopy. *ASSAY and Drug Development Technologies* **11**, 101–107 (2013).
151. Kemper, B. *et al.* Investigation of living pancreas tumor cells by digital holographic microscopy. *Journal of biomedical optics* **11**, 34005 (2006).
152. Green, D. R. & Llambi, F. Cell Death Signaling. *Cold Spring Harbor perspectives in biology* **7**, (2015).
153. Vanden Berghe, T., Linkermann, A., Jouan-Lanhouet, S., Walczak, H. & Vandenabeele, P. Regulated necrosis: the expanding network of non-apoptotic cell death pathways. *Nature reviews. Molecular cell biology* **15**, 135–147 (2014).
154. Kim, K. H. & Lee, M.-S. Autophagy—a key player in cellular and body metabolism. *Nature reviews. Endocrinology* **10**, 322–337 (2014).
155. Elmore, S. Apoptosis: a review of programmed cell death. *Toxicologic pathology* **35**, 495–516 (2007).
156. Taylor, R. C., Cullen, S. P. & Martin, S. J. Apoptosis: controlled demolition at the cellular level. *Nature reviews. Molecular cell biology* **9**, 231–241 (2008).
157. Krysko, D. V., Vanden Berghe, T., D’Herde, K. & Vandenabeele, P. Apoptosis and necrosis: detection, discrimination and phagocytosis. *Methods (San Diego, Calif.)* **44**, 205–221 (2008).
158. GLYNN, J. M., COTTER, T. G. & GREEN, D. R. Apoptosis induced by Actinomycin D, Camptothecin or Aphidicolin can occur in all phases of the cell cycle. *Biochemical Society Transactions* **20**, 84S–84S (1992).
159. Fujisawa, S. *et al.* Evaluation of YO-PRO-1 as an early marker of apoptosis following radiofrequency ablation of colon cancer liver metastases. *Cytotechnology* **66**, 259–273 (2014).

160. Riccardi, C. & Nicoletti, I. Analysis of apoptosis by propidium iodide staining and flow cytometry. *Nature protocols* **1**, 1458–1461 (2006).
161. Gilfillan, A. M., Austin, S. J. & Metcalfe, D. D. Mast cell biology: introduction and overview. *Advances in experimental medicine and biology* **716**, 2–12 (2011).
162. Taylor, M. L. & Metcalfe, D. D. Mast cells in allergy and host defense. *Allergy and asthma proceedings* **22**, 115–119 (2001).
163. Dahlin, J. S. & Hallgren, J. Mast cell progenitors: origin, development and migration to tissues. *Molecular immunology* **63**, 9–17 (2015).
164. Wernersson, S. & Pejler, G. Mast cell secretory granules: armed for battle. *Nature reviews. Immunology* **14**, 478–494 (2014).
165. Lundequist, A. & Pejler, G. Biological implications of preformed mast cell mediators. *Cellular and molecular life sciences : CMLS* **68**, 965–975 (2011).
166. Atiakshin, D., Buchwalow, I., Samoilova, V. & Tiemann, M. Tryptase as a polyfunctional component of mast cells. *Histochemistry and cell biology* **149**, 461–477 (2018).
167. Halova, I. *et al.* Changing the threshold-Signals and mechanisms of mast cell priming. *Immunological reviews* **282**, 73–86 (2018).
168. Żelechowska, P., Agier, J., Kozłowska, E. & Brzezińska-Błaszczak, E. Mast cells participate in chronic low-grade inflammation within adipose tissue. *Obesity reviews : an official journal of the International Association for the Study of Obesity* **19**, 686–697 (2018).
169. Silva, E. Z. M. da, Jamur, M. C. & Oliver, C. Mast cell function: a new vision of an old cell. *The journal of histochemistry and cytochemistry : official journal of the Histochemistry Society* **62**, 698–738 (2014).
170. Nechushtan, H. The complexity of the complicity of mast cells in cancer. *The international journal of biochemistry & cell biology* **42**, 551–554 (2010).
171. Frossi, B. *et al.* Mast cells are associated with the onset and progression of celiac disease. *The Journal of allergy and clinical immunology* **139**, 1266–1274.e1 (2017).
172. Kempuraj, D. *et al.* Mast Cell Activation in Brain Injury, Stress, and Post-traumatic Stress Disorder and Alzheimer's Disease Pathogenesis. *Frontiers in neuroscience* **11**, 703 (2017).
173. Yu, Y., Blokhuis, B. R., Garssen, J. & Redegeld, F. A. Non-IgE mediated mast cell activation. *European journal of pharmacology* **778**, 33–43 (2016).
174. Sibilano, R., Frossi, B. & Pucillo, C. E. Mast cell activation: a complex interplay of positive and negative signaling pathways. *European journal of immunology* **44**, 2558–2566 (2014).
175. Albrecht, M., Müller, K., Köhn, F. M., Meineke, V. & Mayerhofer, A. Ionizing radiation induces degranulation of human mast cells and release of tryptase. *International journal of radiation biology* **83**, 535–541 (2007).
176. Rivera, J. & Olivera, A. A current understanding of Fc epsilon RI-dependent mast cell activation. *Current allergy and asthma reports* **8**, 14–20 (2008).
177. Nakamura, R. & Nakanishi, M. Atomic force microscopy to study the degranulation in rat peritoneal mast cells after activation. *Immunology letters* **69**, 307–310 (1999).
178. Deng, Z. *et al.* Impact of Actin Rearrangement and Degranulation on the Membrane Structure of Primary Mast Cells: A Combined Atomic Force and Laser Scanning Confocal Microscopy Investigation. *Biophysical Journal* **96**, 1629–1639 (2009).

179. Xiang, Z., Block, M., Löfman, C. & Nilsson, G. IgE-mediated mast cell degranulation and recovery monitored by time-lapse photography. *The Journal of allergy and clinical immunology* **108**, 116–121 (2001).
180. Huang, L. *et al.* A rapid and sensitive assay based on particle analysis for cell degranulation detection in basophils and mast cells. *Pharmacological Research* **111**, 374–383 (2016).
181. Okayama, Y. & Kawakami, T. Development, migration, and survival of mast cells. *Immunologic research* **34**, 97–115 (2006).
182. Kuriu, A. *et al.* Proliferative potential of degranulated murine peritoneal mast cells. *Blood* **74**, 925–929 (1989).
183. Dvorak, A. M., Schleimer, R. P. & Lichtenstein, L. M. Human mast cells synthesize new granules during recovery from degranulation. In vitro studies with mast cells purified from human lungs. *Blood* **71**, 76–85 (1988).
184. Rådinger, M., Jensen, B. M., Swindle, E. & Gilfillan, A. M. Assay of mast cell mediators. *Methods in molecular biology (Clifton, N.J.)* **1220**, 307–323 (2015).
185. Lee, J., Veatch, S. L., Baird, B. & Holowka, D. Molecular mechanisms of spontaneous and directed mast cell motility. *Journal of leukocyte biology* **92**, 1029–1041 (2012).
186. Mesri, E. A., Cesarman, E. & Boshoff, C. Kaposi's sarcoma and its associated herpesvirus. *Nature reviews. Cancer* **10**, 707–719 (2010).
187. Bhutani, M., Polizzotto, M. N., Uldrick, T. S. & Yarchoan, R. Kaposi Sarcoma-Associated Herpesvirus-Associated Malignancies: Epidemiology, Pathogenesis, and Advances in Treatment. *Seminars in Oncology* **42**, 223–246 (2015).
188. Avey, D., Brewers, B. & Zhu, F. Recent advances in the study of Kaposi's sarcoma-associated herpesvirus replication and pathogenesis. *Virologica Sinica* **30**, 130–145 (2015).
189. Giffin, L. & Damania, B. KSHV: Pathways to Tumorigenesis and Persistent Infection. *Advances in Virus Research* 111–159 (2014).doi:10.1016/b978-0-12-800098-4.00002-7
190. Uppal, T., Jha, H., Verma, S. & Robertson, E. Chromatinization of the KSHV Genome During the KSHV Life Cycle. *Cancers* **7**, 112–142 (2015).
191. Guito, J. & Lukac, D. KSHV Reactivation and Novel Implications of Protein Isomerization on Lytic Switch Control. *Viruses* **7**, 72–109 (2015).
192. Purushothaman, P., Uppal, T. & Verma, S. Molecular Biology of KSHV Lytic Reactivation. *Viruses* **7**, 116–153 (2015).
193. Cai, Q., Verma, S. C., Lu, J. & Robertson, E. S. Molecular biology of Kaposi's sarcoma-associated herpesvirus and related oncogenesis. *Advances in virus research* **78**, 87–142 (2010).
194. Hosseinipour, M. C. *et al.* Viral Profiling Identifies Multiple Subtypes of Kaposi's Sarcoma. *mBio* **5**, e01633–14–e01633–14 (2014).
195. Myoung, J. & Ganem, D. Generation of a doxycycline-inducible KSHV producer cell line of endothelial origin: maintenance of tight latency with efficient reactivation upon induction. *Journal of virological methods* **174**, 12–21 (2011).
196. Muñoz-Espín, D. & Serrano, M. Cellular senescence: from physiology to pathology. *Nature reviews. Molecular cell biology* **15**, 482–496 (2014).
197. Salama, R., Sadaie, M., Hoare, M. & Narita, M. Cellular senescence and its effector programs. *Genes & development* **28**, 99–114 (2014).

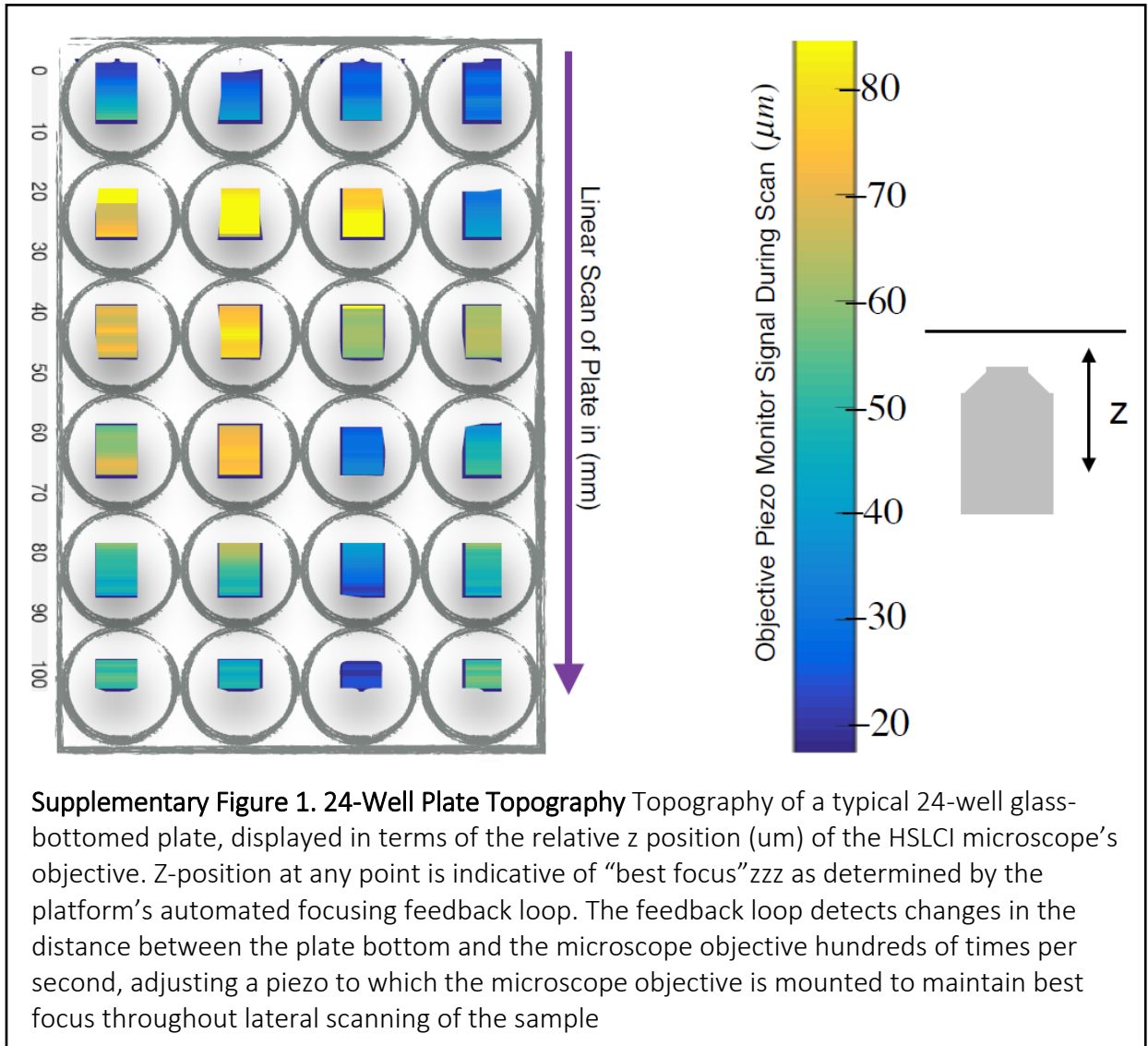
198. Lecot, P., Alimirah, F., Desprez, P.-Y., Campisi, J. & Wiley, C. Context-dependent effects of cellular senescence in cancer development. *British journal of cancer* **114**, 1180–1184 (2016).
199. Achuthan, S., Santhoshkumar, T. R., Prabhakar, J., Nair, S. A. & Pillai, M. R. Drug-induced senescence generates chemoresistant stemlike cells with low reactive oxygen species. *The Journal of biological chemistry* **286**, 37813–37829 (2011).
200. Cahu, J. & Sola, B. A sensitive method to quantify senescent cancer cells. *Journal of visualized experiments : JoVE* (2013).doi:10.3791/50494
201. Lee, M. & Lee, J.-S. Exploiting tumor cell senescence in anticancer therapy. *BMB reports* **47**, 51–59 (2014).
202. Jemal, A., Center, M. M., DeSantis, C. & Ward, E. M. Global Patterns of Cancer Incidence and Mortality Rates and Trends. *Cancer Epidemiology Biomarkers & Prevention* **19**, 1893–1907 (2010).
203. Eton, D. T., Lepore, S. J. & Helgeson, V. S. Early quality of life in patients with localized prostate carcinoma: an examination of treatment-related, demographic, and psychosocial factors. *Cancer* **92**, 1451–1459 (2001).
204. Rebbeck, T. R. Prostate Cancer Genetics: Variation by Race, Ethnicity, and Geography. *Seminars in Radiation Oncology* **27**, 3–10 (2017).
205. Bock, C. H. *et al.* Results from a prostate cancer admixture mapping study in African-American men. *Human Genetics* **126**, 637–642 (2009).
206. Kerns, S. L. *et al.* Genome-wide association study to identify single nucleotide polymorphisms (SNPs) associated with the development of erectile dysfunction in African-American men after radiotherapy for prostate cancer. *International journal of radiation oncology, biology, physics* **78**, 1292–1300 (2010).
207. Klein, D. *et al.* Endothelial Caveolin-1 regulates the radiation response of epithelial prostate tumors. *Oncogenesis* **4**, e148 (2015).
208. Mobley, D. F., Khera, M. & Baum, N. Recent advances in the treatment of erectile dysfunction. *Postgraduate Medical Journal* **93**, 679–685 (2017).
209. Ahn, K., Pan, S., Beningo, K. & Hupe, D. A permanent human cell line (EA.hy926) preserves the characteristics of endothelin converting enzyme from primary human umbilical vein endothelial cells. *Life sciences* **56**, 2331–2341 (1995).
210. Drews-Elger, K. *et al.* Primary breast tumor-derived cellular models: characterization of tumorigenic, metastatic, and cancer-associated fibroblasts in dissociated tumor (DT) cultures. *Breast cancer research and treatment* **144**, 503–517 (2014).
211. Zhang, X. *et al.* A renewable tissue resource of phenotypically stable, biologically and ethnically diverse, patient-derived human breast cancer xenograft models. *Cancer research* **73**, 4885–4897 (2013).
212. Li, S. *et al.* Endocrine-therapy-resistant ESR1 variants revealed by genomic characterization of breast-cancer-derived xenografts. *Cell reports* **4**, 1116–1130 (2013).
213. Liu, X. *et al.* Short-Form Ron Promotes Spontaneous Breast Cancer Metastasis through Interaction with Phosphoinositide 3-Kinase. *Genes & cancer* **2**, 753–762 (2011).
214. Wagenblast, E. *et al.* A model of breast cancer heterogeneity reveals vascular mimicry as a driver of metastasis. *Nature* **520**, 358–362 (2015).

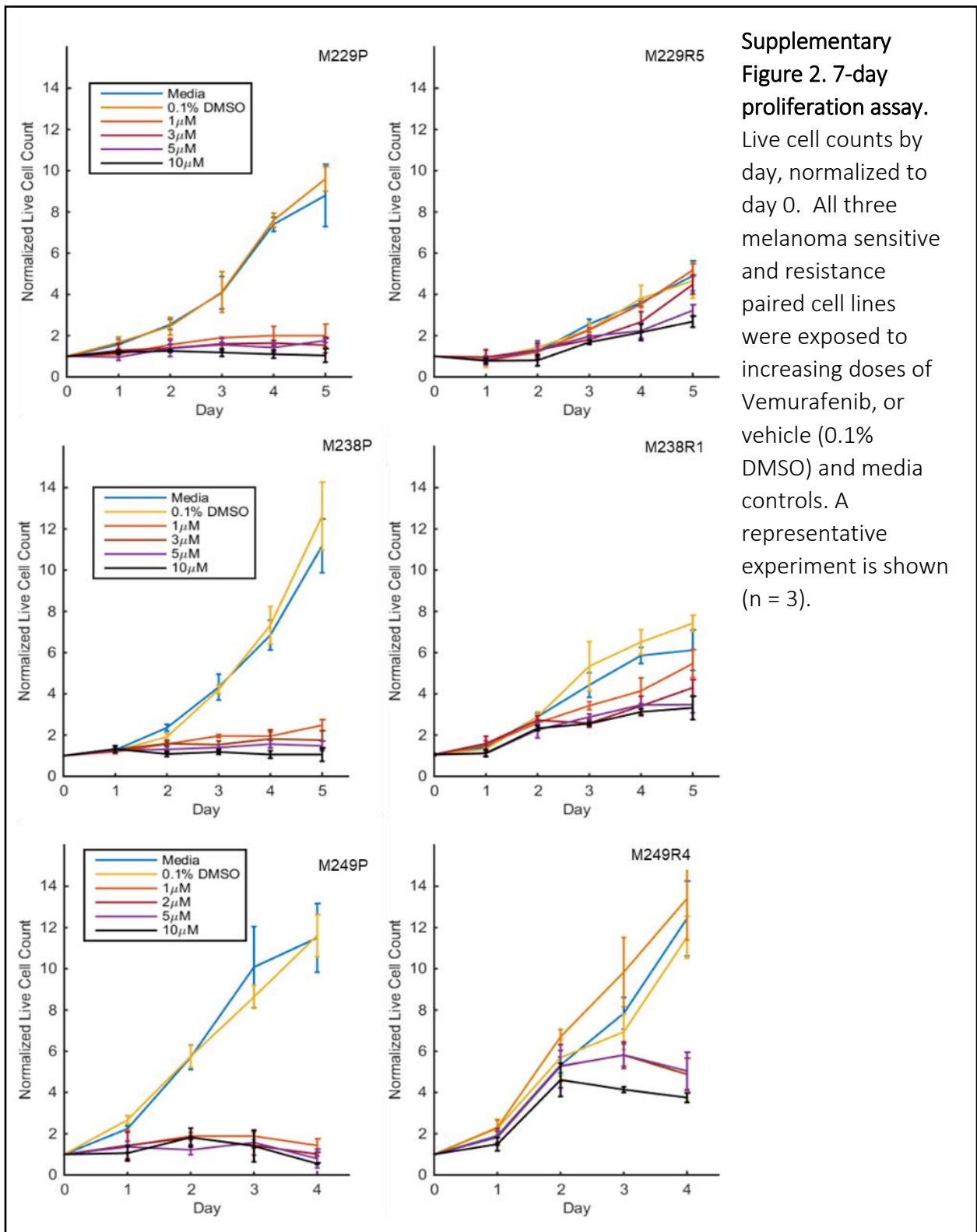
215. Prat, A. *et al.* Characterization of cell lines derived from breast cancers and normal mammary tissues for the study of the intrinsic molecular subtypes. *Breast cancer research and treatment* **142**, 237–255 (2013).
216. Duncan, J. S. *et al.* Dynamic reprogramming of the kinome in response to targeted MEK inhibition in triple-negative breast cancer. *Cell* **149**, 307–321 (2012).
217. Jung, J., Seol, H. S. & Chang, S. The Generation and Application of Patient-Derived Xenograft Model for Cancer Research. *Cancer research and treatment : official journal of Korean Cancer Association* **50**, 1–10 (2018).
218. Lai, Y. *et al.* Current status and perspectives of patient-derived xenograft models in cancer research. *Journal of hematology & oncology* **10**, 106 (2017).
219. Whittle, J. R., Lewis, M. T., Lindeman, G. J. & Visvader, J. E. Patient-derived xenograft models of breast cancer and their predictive power. *Breast cancer research : BCR* **17**, 17 (2015).
220. Hidalgo, M. *et al.* Patient-derived xenograft models: an emerging platform for translational cancer research. *Cancer discovery* **4**, 998–1013 (2014).
221. Network, C. G. A. Comprehensive molecular portraits of human breast tumours. *Nature* **490**, 61–70 (2012).
222. Harrell, J. C. *et al.* Genomic analysis identifies unique signatures predictive of brain, lung, and liver relapse. *Breast cancer research and treatment* **132**, 523–535 (2012).
223. Ignatiadis, M., Desmedt, C., Sotiriou, C., Azambuja, E. de & Piccart, M. HER-2 as a target for breast cancer therapy. *Clinical cancer research : an official journal of the American Association for Cancer Research* **15**, 1848–1852 (2009).
224. Ignatiadis, M. & Sotiriou, C. Breast cancer: Should we assess HER2 status by Oncotype DX? *Nature reviews. Clinical oncology* **9**, 12–14 (2011).
225. Sharma, P. Biology and Management of Patients With Triple-Negative Breast Cancer. *The oncologist* **21**, 1050–1062 (2016).
226. Anders, C. K., Abramson, V., Tan, T. & Dent, R. The Evolution of Triple-Negative Breast Cancer: From Biology to Novel Therapeutics. *American Society of Clinical Oncology educational book. American Society of Clinical Oncology. Meeting* **35**, 34–42 (2016).
227. Dent, R. *et al.* Pattern of metastatic spread in triple-negative breast cancer. *Breast cancer research and treatment* **115**, 423–428 (2009).
228. Lin, N. U. *et al.* Sites of distant recurrence and clinical outcomes in patients with metastatic triple-negative breast cancer: high incidence of central nervous system metastases. *Cancer* **113**, 2638–2645 (2008).
229. Prat, A. *et al.* Molecular characterization of basal-like and non-basal-like triple-negative breast cancer. *The oncologist* **18**, 123–133 (2013).
230. Jitariu, A.-A., Cîmpean, A. M., Ribatti, D. & Raica, M. Triple negative breast cancer: the kiss of death. *Oncotarget* **8**, 46652–46662 (2017).
231. Dent, R. *et al.* Triple-negative breast cancer: clinical features and patterns of recurrence. *Clinical cancer research : an official journal of the American Association for Cancer Research* **13**, 4429–4434 (2007).
232. Lee, A. & Djamgoz, M. B. A. Triple negative breast cancer: Emerging therapeutic modalities and novel combination therapies. *Cancer treatment reviews* **62**, 110–122 (2018).

233. Nielsen, D. L., Kümler, I., Palshof, J. A. E. & Andersson, M. Efficacy of HER2-targeted therapy in metastatic breast cancer. Monoclonal antibodies and tyrosine kinase inhibitors. *Breast (Edinburgh, Scotland)* **22**, 1–12 (2013).
234. Quail, D. F. & Joyce, J. A. Microenvironmental regulation of tumor progression and metastasis. *Nature medicine* **19**, 1423–1437 (2013).
235. Shamir, E. R. & Ewald, A. J. Three-dimensional organotypic culture: experimental models of mammalian biology and disease. *Nature reviews. Molecular cell biology* **15**, 647–664 (2014).
236. Modena, M. M., Chawla, K., Misun, P. M. & Hierlemann, A. Smart Cell Culture Systems: Integration of Sensors and Actuators into Microphysiological Systems. *ACS chemical biology* (2018).doi:10.1021/acscchembio.7b01029
237. Zhang, W., Zhuang, A., Gu, P., Zhou, H. & Fan, X. A review of the three-dimensional cell culture technique: Approaches, advantages and applications. *Current stem cell research & therapy* **11**, 370–380 (2016).
238. Ravi, M., Paramesh, V., Kaviya, S. R., Anuradha, E. & Solomon, F. D. P. 3D cell culture systems: advantages and applications. *Journal of cellular physiology* **230**, 16–26 (2015).
239. *Tumor Organoids*. (Springer International Publishing: 2018).doi:10.1007/978-3-319-60511-1
240. Szade, K. *et al.* Spheroid-plug model as a tool to study tumor development, angiogenesis, and heterogeneity in vivo. *Tumour biology : the journal of the International Society for Oncodevelopmental Biology and Medicine* **37**, 2481–2496 (2016).
241. Drost, J. & Clevers, H. Organoids in cancer research. *Nature reviews. Cancer* **18**, 407–418 (2018).
242. Kota, S. *et al.* A novel three-dimensional high-throughput screening approach identifies inducers of a mutant KRAS selective lethal phenotype. *Oncogene* (2018).doi:10.1038/s41388-018-0257-5
243. Wang, Z. *et al.* Spatial light interference microscopy (SLIM). *Optics express* **19**, 1016–1026 (2011).
244. Cohen, M. Z. *et al.* Symptoms and quality of life in diverse patients undergoing hematopoietic stem cell transplantation. *Journal of pain and symptom management* **44**, 168–180 (2012).

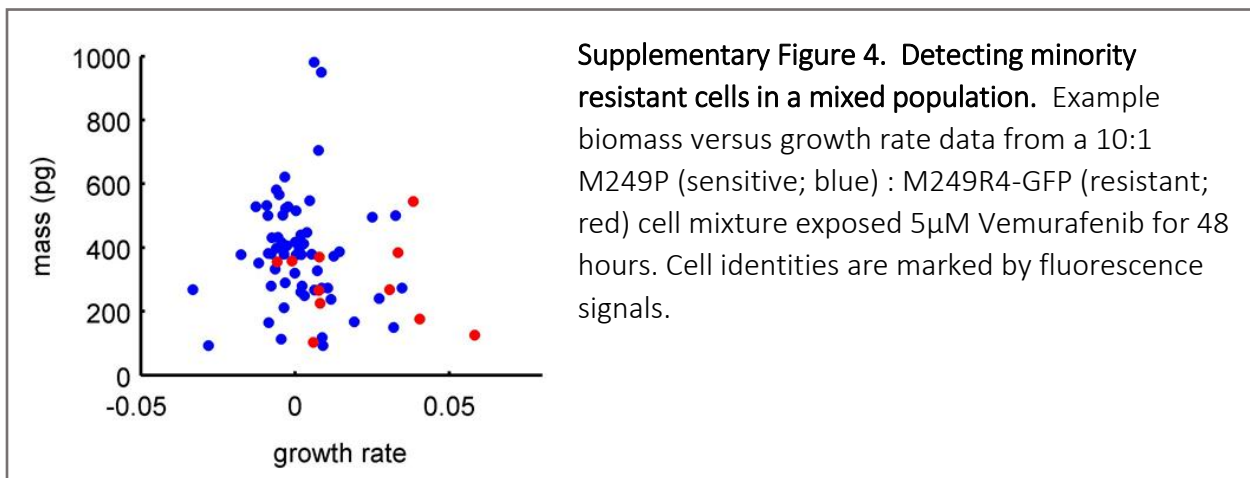
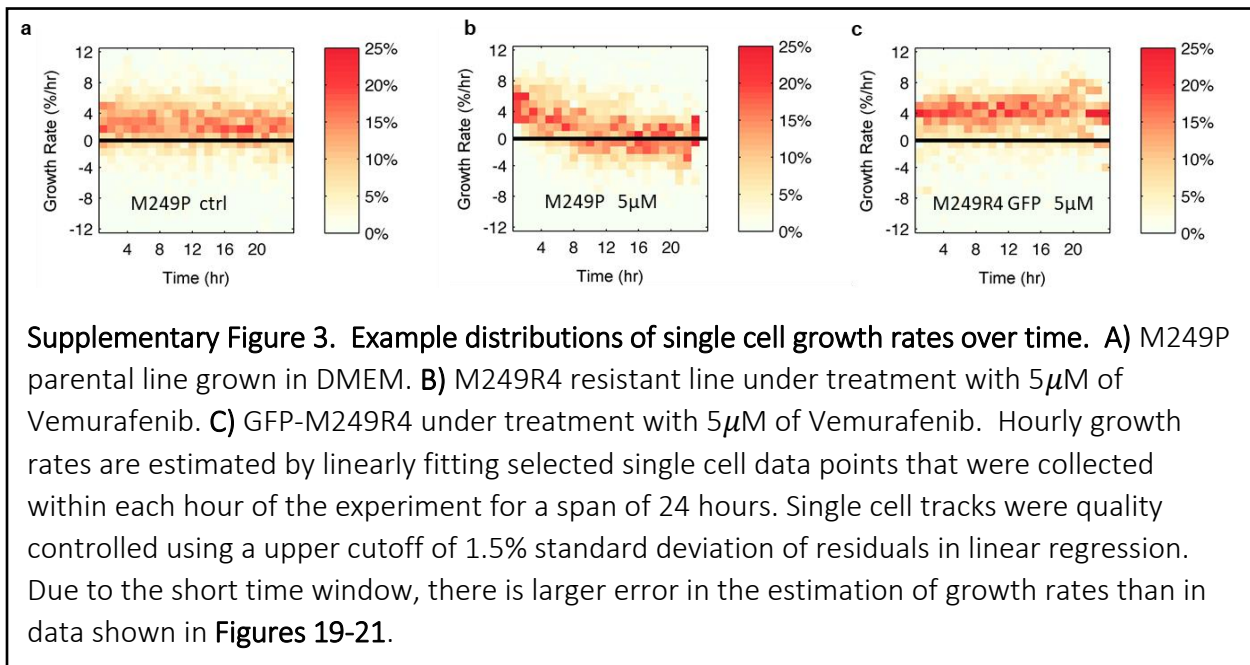
Appendix

Supplementary Figures





Supplementary Figure 2. 7-day proliferation assay. Live cell counts by day, normalized to day 0. All three melanoma sensitive and resistance paired cell lines were exposed to increasing doses of Vemurafenib, or vehicle (0.1% DMSO) and media controls. A representative experiment is shown (n = 3).



Supplementary Tables

Supplementary Table 1. Patient-Derived Melanoma Lines

| <u>Cell Line Designation</u> | <u>Molecular Lesions</u> |
|------------------------------|---|
| M229P | BRAF V600E |
| M229R5 | BRAF V600E, PDGFR β up-regulation |
| M238P | BRAF V600E |
| M238R1 | BRAF V600E, PDGFR β up-regulation |
| M249P | BRAF V600E |
| M249R4 | BRAF V600E, N-RAS Q(61)K |

Supplementary Table 2. Kinase Inhibitor Dosing Chart

| <u>Trade</u> | <u>Drug</u> | <u>Chemical</u> | <u>Clinical Dose</u> | <u>Target</u> | <u>Serum Conc.</u> | |
|--------------|-------------|-----------------------|----------------------|---------------|--------------------|-------------------------------|
| | | | | | <u>(ng/mL)</u> | <u>μM (1x)</u> |
| Tafinlar | Dabrafenib | GSK2118436 | 150 mg twice daily | BRAF | 1050 | 2.02 |
| Cotellic | Cobimetinib | GDC-0973 / RG7420 | 60 mg once daily | MEK1 | 273 | 0.51 |
| N/A | Selumetinib | AZD6244 / ARRY-142886 | 75 mg twice daily | MEK1 | 1165 | 2.55 |
| Mekinist | Trametinib | GSK1120212 | 2 mg once daily | MEK1/2 | 22.2 | 0.04 |
| N/A | Binimetinib | MEK162 / ARRY-162 | 45 mg twice daily | MEK1/2 | 257.0 | 0.58 |

Supplementary Table 3. Mast Cell Fluorescence Experiments

| <u>Date</u> | <u>Duration (hrs)</u> | <u>Medium</u> | <u>Dye</u> | <u>Treatment</u> |
|-------------|-----------------------|--|---------------------|------------------|
| 19-May | 18 | Media + Methyl cellulose | None | None |
| 21-May | 17 | Media + Methyl cellulose vs. Media + Fibronectin | None | None |
| 27-May | 1 | Media + Methyl cellulose | YoPro + PI | DNP-HSA |
| 28-May | 15 | Media + Methyl cellulose | YoPro + PI | DNP-HSA |
| 3-Jun | 9 | Media + Methyl cellulose | YoPro + PI | Ionomycin |
| 5-Jun | 24 | Media + Methyl cellulose | YoPro + PI | None |
| 10-Jun | 20 | Media + Methyl cellulose | None vs. YoPro + PI | None |
| 11-Jun | 24 | Media + Methyl cellulose | YoPro + PI | Ionomycin |
| 12-Jun | 24 | Media + Methyl cellulose | YoPro + PI | Ionomycin |
| 18-Jun | 21 | PBS (w/out Ca or Mg) | YoPro + PI | None |
| 21-Jun | 21 | PBS (w/out Ca or Mg) | YoPro + PI | Ionomycin |

Supplementary Methods

M249R4-GFP cell generation. Third generation lentiviral construct pMD.G (VSV-G envelope) was used in combination with pMDLg/pRRE (gag/pol elements) and pRSV-REV. Lentivirus was produced by transient plasmid co-transfection into HEK293T cells. Infections used protamine sulphate, with mGFP subcloned into the FUGW vector. M249R4 GFP-positive cells were obtained using a BD FACSAria sorter. GFP expression was determined 4 days after sorting by a BD LSRII flow cytometer. FACS Diva analysis showed 98.4% of M249R4-GFP cells express mGFP.

Drug Sourcing and Preparation. Imatinib (Cat.# S1026), Dabrafenib (Cat.# S2807), Selumetinib (Cat.# S1008), Trametinib (Cat.# S2673), Cobimetinib (5mg, Cat.# S8041) and Binimetinib (10mg, Cat.# S7007) were purchased from Selleck Chemicals (Houston, TX). Imatinib, Vemurafenib, Dabrafenib, Selumetinib, and Trametinib were supplied at 10mM in DMSO. Cobimetinib and Binimetinib were supplied as dry powders but suspended in DMSO to a final stock concentration of 10mM upon receipt.

Kinase Inhibitor 1X Dose Determination: For each inhibitor, a “1X” dose was calculated. Briefly, clinical doses were obtained from publically-available package inserts or, if none were available, the median dose administered in clinical trials. Doses were matched to peak serum concentration values (C_{max} (ng/mL)) for each inhibitor as measured in clinical trials in which the doses were utilized. If multiple C_{max} values were available, those values were averaged to yield a single peak serum concentration value. Using each drugs’ molecular weight, peak serum concentration values were converted to micromolar (μ M) units and designated as “1X”. Unless otherwise noted, clinical

doses were sourced from package inserts and used to identify C_{max} values in studies. References for C_{max} determinations: imatinib ⁴⁻⁶, dabrafenib ⁷⁻⁸, Cobimetinib ⁹, Selumetinib ¹⁰⁻¹³ (*dose determined from median of clinical trial doses*), Trametinib ¹⁴, and Binimetinib ¹⁵⁻¹⁶ (*dose determined from median of clinical trial doses*).

Cell proliferation assay. Cells in multiple six-well tissue culture plates were incubated overnight at 37°C, 5% CO₂. Each six-well plate contained one well with a media control, one well with 0.1% DMSO vehicle control, and four wells of Vemurafenib at 1 μM, 3 μM, 5 μM, or 10 μM concentrations. Cells were counted each day for five days following seeding.

Supplementary References

1. Bon, P., et al. Quadriwave lateral shearing interferometry for quantitative phase microscopy of living cells. *Optics Express* **2009**, *17* (15), 13080-13094.
2. Reed, J., et al. Rapid, massively parallel single-cell drug response measurements via live cell interferometry. *Biophysical journal* **2011**, *101* (5), 1025-31.
3. Zhang, T., et al. The genomic landscape of cutaneous melanoma. *Pigment cell & melanoma research* **2016**, *29* (3), 266-83.
4. Peng, B., et al. Pharmacokinetics and pharmacodynamics of imatinib in a phase I trial with chronic myeloid leukemia patients. *Journal of clinical oncology : official journal of the American Society of Clinical Oncology* **2004**, *22*(6), 935-942.
5. von Mehren, M.; Widmer, N., Correlations between imatinib pharmacokinetics, pharmacodynamics, adherence, and clinical response in advanced metastatic gastrointestinal stromal tumor (GIST): an emerging role for drug blood level testing? *Cancer treatment reviews* **2011**, *37*(6), 291-299.
6. Larson, R. A., et al. Imatinib pharmacokinetics and its correlation with response and safety in chronic-phase chronic myeloid leukemia: a subanalysis of the IRIS study. *Blood* **2008**, *111*(6), 4022-4028.
7. Falchook, G. S., et al. Dose selection, pharmacokinetics, and pharmacodynamics of BRAF inhibitor dabrafenib (GSK2118436). *Clinical cancer research : an official journal of the American Association for Cancer Research* **2014**, *20*(6), 4449-4458.
8. Park, J., et al. Pharmacokinetics of dabrafenib in a patient with metastatic melanoma undergoing haemodialysis. *Pigment cell & melanoma research* **2017**, *30*(6), 68-71.
9. Han, K., et al. Population pharmacokinetics and dosing implications for cobimetinib in patients with solid tumors. *Cancer chemotherapy and pharmacology* **2015**, *76*(6), 917-924.
10. LoRusso, P. M., et al. A phase I dose-escalation study of selumetinib in combination with docetaxel or dacarbazine in patients with advanced solid tumors. *BMC cancer* **2017**, *17*(6), 173.
11. Leijen, S., et al. A phase I, open-label, randomized crossover study to assess the effect of dosing of the MEK 1/2 inhibitor Selumetinib (AZD6244; ARRY-142866) in the presence and absence of food in patients with advanced solid tumors. *Cancer chemotherapy and pharmacology* **2011**, *68*(6), 1619-1628.

12. Adjei, A. A., et al. Phase I pharmacokinetic and pharmacodynamic study of the oral, small-molecule mitogen-activated protein kinase kinase 1/2 inhibitor AZD6244 (ARRY-142886) in patients with advanced cancers. *Journal of clinical oncology : official journal of the American Society of Clinical Oncology* **2008**, *26(6)*, 2139-2146.
13. Coleman, R. L., et al. A phase II evaluation of selumetinib (AZD6244, ARRY-142886), a selective MEK-1/2 inhibitor in the treatment of recurrent or persistent endometrial cancer: an NRG Oncology/Gynecologic Oncology Group study. *Gynecologic oncology* **2015**, *138(6)*, 30-35.
14. Infante, J. R., et al. Safety, pharmacokinetic, pharmacodynamic, and efficacy data for the oral MEK inhibitor trametinib: a phase 1 dose-escalation trial. *The Lancet. Oncology* **2012**, *13(6)*, 773-781.
15. Dummer, R., et al. Results of NEMO: A phase III trial of binimetinib (BINI) vs dacarbazine (DTIC) in NRAS-mutant cutaneous melanoma. *Journal of Clinical Oncology* **2016**, *34(6)*, 9500-9500.
16. Bendell, J. C., et al. A phase 1 dose-escalation and expansion study of binimetinib (MEK162), a potent and selective oral MEK1/2 inhibitor. *British journal of cancer* **2017**, *116(6)*, 575-583.

Vita

Kevin Alexander Leslie was born on January 28, 1986, in San Mateo, California. He graduated from Langley High School in McLean, Virginia in 2004. He received his Bachelor of Science in Biology from The College of William & Mary in Williamsburg, Virginia in 2009 and his Master of Science in Biology from The College of William & Mary in 2012. He managed Dr. Jason Reed's laboratory in the Physics Department at Virginia Commonwealth University for two years (2012-2014) prior to beginning coursework for the Integrative Life Sciences program.